Journal of Volcanology and Geothermal Research

Explosive Glaciovolcanism at Cracked Mountain Volcano, Garibaldi Volcanic Belt, Canada

--Manuscript Draft--

Manuscript Number:	VOLGEO-D-21-00262R1
Article Type:	Research Paper
Keywords:	Glaciovolcanism; Subglacial; Phreatomagmatic; Basalt; Englacial Lake; Ice-Sheet
Corresponding Author:	Martin Harris University of British Columbia CANADA
First Author:	Martin Harris
Order of Authors:	Martin Harris
	James K. Russell, PhD
	Rene Barendregt, PhD
	Lucy A. Porritt, PhD
	Alexander Wilson, PhD
Abstract:	Cracked Mountain (CM) is a basaltic volcano within the northern extension of the Cascade volcanic arc into southwest, British Columbia, Canada (i.e. Garibaldi Volcanic Belt) and is dated at 401 ± 38 ka (40 Ar/ 39 Ar). The edifice covers an area of ~1.5 km 2 and has a volume of 0.18 km 3 . The volcano features steep margins with local relief of ~250 m (1,650 m a.s.l), is dissected by abundant 0.5 to ~20 m wide extensional cracks with depths up to 30 m, and has a highly eroded top. The edifice is dominated by massive to poorly stratified, moderately to pervasively palagonitized lapilli tuffs, comprising vitric fine ash to lapilli. Juvenile pyroclasts have blocky to highly vesiculated shapes consistent with a phreatomagmatic (i.e. explosive) origin. The lapilli tuffs are intruded by and mingled with coherent to disaggregated lobes of peperitic pillowed lavas. Contacts between lapilli tuff and peperitic pillowed lava show soft-sediment deformation and in-situ quench-fragmentation indicating that the tephra was both unconsolidated and water-saturated at the time of intrusion. Local stacks of pillow lava are found on the margins of the edifice. More than fifty, 0.5 to 3 m wide dykes intrude CM stratigraphy and display, either, peperitic pillowed margins or sharp, chilled margins and columnar-jointing. Measurements of paleomagnetic directions (9 sites) were made for all CM lithofacies and record a single-pole direction indicating a single monogenetic eruption. A glaciovolcanic origin is strongly suggested by the abundant subaqueous lithofacies (i.e. palagonitized tephra, pillows, peperites) and the physiographic setting of the edifice which is well above any drainage that could sustain a standing body of water. The elevation of CM and depth of surrounding valleys indicate syn-eruptive confinement by a paleo-ice sheet that was ≥ 850 m thick. The edifice shape, size, and surrounding topography suggest a 'leaky' paleolake system capable of supporting ~0.36 km 3 of water. The glaciovolcanic origin and the absolute (40 Ar/ 39 Ar) age of CM represent an important record of the Cordilleran Ice sheet (CIS) in southwestern BC during the mid-Pleistocene.
Suggested Reviewers:	Ben Edwards, PhD Professor, Dickinson College edwardsb@dickinson.edu This researcher has expertise in the field of glaciovolcanism.
	Ian Skilling, PhD Senior Lecturer, University of South Wales ian.skilling@southwales.ac.uk This researcher has expertise in the field of glaciovolcanism.
	Brittany Brand, PhD Professor, Boise State University brittanybrand@boisestate.edu

	This researcher has expertise in the field of physical volcanology, particularly phreatomagmatic styled eruptions and the resulting volcaniclastic deposits.
	Pierre-Simon Ross, PhD Professor, Institut national de la recherche scientifique pierre-simon.ross@ete.inrs.ca This researcher has expertise in phreatomagmatic fragmentation processes that occur during subaqueous style eruptions.
	Catherine Hickson, PhD Adjunct Professor, The University of British Columbia chickson@eoas.ubc.ca This researcher has expertise in the field of volcanology, with extensive work done in the Cascade and Garibaldi Volcanic Arc.
	Melanie Kelman, PhD Geological Survey of Canada: Natural Resources Canada Earth Sciences Melanie.Kelman@nrcan-rncan.gc.ca This researcher has expertise in the field of glaciovolcanism and has worked extensively in the Garibaldi Volcanic Belt.
Opposed Reviewers:	
Response to Reviewers:	

January 11, 2022

JVGR Editorial Board
Journal of Volcanology and Geothermal Research
Elsevier Editorial System

To the Editorial Board,

This letter is to accompany our revised manuscript: "Explosive Glaciovolcanism at Cracked Mountain Volcano, Garibaldi Volcanic Belt, Canada" submitted to the Journal of Volcanology and Geothermal Research for publication as a Research Paper. The manuscript is authored by me (Martin Harris), Kelly Russell, Rene Barendregt, Lucy A. Porritt, and Alexander Wilson and is an original unpublished research article and is not under review, elsewhere.

The original submission was reviewed by Dr. Rosie Cole, who provided feedback in the form of minor comments. The manuscript was also reviewed by the JVGR editor Jim Gardner, who provided constructive feedback on ways to improve the flow and presentation of information. We have essentially accepted and incorporated all comments from both reviewers. Additionally, we have gone through the entire document, including text, figures, and tables, and moderately revised portions for clarity and to reduce redundancies. The details of these revisions can be found in our response to the editor document. Our submission includes our manuscript (with changes tracked and a clean version provided), 14 figures, and 3 tables, accompanied by 3 supplements (containing 2 figures and 3 tables). The word count is ~6400 words (from introduction to summary).

Our work contributes to the field of glaciovolcanism. Few studies have identified explosive onsets to glaciovolcanic eruptions making the deposits found at Cracked Mountain unique within the existing literature. We think these results will be of interest to, both, volcanologists and paleoclimatologists. We believe publication in JVGR offers us an appropriately broad and international readership.

Below is a list of potential referees for this manuscript who we feel would be interested and willing to provide a timely and impartial evaluation of the merits of our work:

Ben Edwards –Earth Sciences, Dickinson College, Carlisle, PA, USA; edwardsb@dickinson.edu
Ian Skilling –Geology, University of South Wales, Pontypridd, United Kingdom; ian.skilling@southwales.ac.uk
Brittany Brand –Geosciences, Boise State University, Boise, ID, USA; brittanybrand@boisestate.edu.
Pierre-Simon Ross – Institut national de la recherche scientifique, Quebec City; pierre-simon.ross@ete.inrs.ca
Catherine Hickson – Tuya Terra Geo Corp, Vancouver, Canada, ttgeo@telus.net
Melanie Kelman –Geological Survey of Canada, Vancouver, Melanie.Kelman@nrcan-rncan.gc.ca.

Thank you in advance for your consideration.
Sincerely,

Martin Harris
Corresponding Author Contact Details:
Martin Harris
Department of Earth, Ocean, and Atmospheric Sciences
University of British Columbia
2020-2207 Main Mall,Vancouver, BC V6T 1Z4, Canada
+1 603 727 2944
mharris@eoas.ubc.ca

Manuscript Number: VOLGEO-D-21-00262 Response to Reviewers

Reviewer #1: Review of Harris et al: "Explosive volcanism at Cracked Mountain Volcano, GVB, Canada"
JVGR
Rosie Cole

This manuscript provides a glaciovolcanic eruption and emplacement model for the Cracked Mountain edifice, based dominantly on detailed field evidence. It is a great contribution of an explosively formed edifice with intrusive and peperitic bodies. Paleomagnetic field directions derived from all units are used to support a continuous eruptive history. The study provides a constraint on the thickness of the continental ice sheet at the time of eruption. It is a good example of how glaciovolcanic sequences can be used as paleoenvironmental indicators.

The manuscript gives fantastic detailed field descriptions of each lithofacies. The lithofacies associations make the relations between different rock types clear. Interpretations are justified and supported by relevant evidence. It is great to see additional paleomagnetic evidence which supports the eruption model. The text is also well structured and written, and the figures are clear and informative. My comments are minor:

Line 49: Can you briefly explain what the Mosaic Assemblage is?
Author response: We have elaborated in the text what the Mosaic Assemblage is defined as (line 47 in revised text).

Line 161: What is a blooming dyke?
Author response: We have expanded this sentence to include a description of what I mean by 'blooming' dyke (line 155 in revised text)

Line 164: Unfinished sentence, but peperite is defined with White and Houghton reference above, so it isn´t necessary here.

Author response: We agree with this comment and this sentence has been removed.

Line 182: "Commonly glaciated" suggests a glacier still sometimes accumulates here. Do you mean that at one time a glacier has over-ridden this lava to make striations and deposit erratics?

Author response: We have removed 'commonly glaciated' as I agree it can be misconstrued. I have revised the sentence to clarify that the tops of the lavas are scoured by past cycles of glaciation and that erratics now sit on top (line 171 in revised text).

Line 199: You mention that the source of the deposits is higher up - can you say where the vent(s) was? What was the relationship between the vent and the ice? Have these deposits travelled under ice from the vent or have they met ice further away from the eruption site?

Author response: We have added a couple of clarifying sentences at the start of subsection 5 (line 184 in revised text), which add more information on our understanding of vent location and any evidence of magma-ice contacts.

Line 282: Which rocks were these samples taken from for chemical analysis? Can you explain the spread in chemistry shown by the TAS diagram? Is there a relationship between the chemistry and the inferred phase of eruption, for example?

Author response: We have added a clarifying sentence (line 267 in revised text) to address which volcanic units were used for whole-rock chemistry. I have expanded the end of the second paragraph (line 276 in revised text) in this section to explain possible reasons for the spread of TAS and how it relates to stages of the eruption.

Line 553-560: Is there any other evidence from the region that you can use to support this estimate for ice thickness at this slightly older date or during MIS 12?

Author response: We have revised parts of the text (lines 479-501 in revised text), to provide more regional evidence of volcanism during MIS 12. Although no other dates exist that can support our ice thickness models, there are a few older studies that indicate the presence of, or absence, of glacial ice in SW British Columbia at this period in the Pleistocene. I have cited an additional study to support these additions.

Line 578: intrusive and effusive styles?

Author response: We have changed this sentence to say 'intrusive and effusive activity (line 518 in revised text).

Figure 1: label all features mentioned in geological background text.
Author response: We have revised this figure to include additional features mentioned in the geological background, including the explorer plate, Salal Glacier, Elaho valley, Mosaic Ridge, Lillooet Ridge.
Figure 2: - Log 5 is shown in the granodiorite
- Lithologies legend, second down - check spelling of coherent.
- Third down - what is lava tuff?

Author response: We have moved the Log 5 location to be at the edge of the edifice, and corrected the spelling of coherent, and added the work breccia that was previously missing. Additional reformatting was also done on this figure to increase font sizes and improve readability.

Figure 3: not easy to see the cracks here - can they be emphasised or can some be annotated?

Author response: We have added another google earth image, now 3B, that better shows the cracks that run through the whole volcano.

Figure 11: Can you show the Maximum Angular Deviation (MAD3) on these plots? Is the ambient regional paleomagnetic field direction for this area and time known? If so, it should be stated and shown for comparison on the stereoplot. Is it consistent with the direction shown for these deposits? This would give confidence to both the age estimate and the assumption that there has been no rotation.

Author response: MAD values have been added as suggested by the reviewer. GAD (Geocentric Axial Dipole field directions) and PEF (present earth's field directions) for sampling locality have now been added to TableC1 and Fig. 11, as suggested by the reviewer. The mean direction for sites is within expected secular variation (see mean of sites 2-9 and GAD inclination for sampling latitude, Fig. 11 and Table C1. Additionally, reported values have been adjusted to the tenth decimal place (rather than the hundredth) to better represent the precision of the paleomagnetic results. Lastly, in Fig 11B, we replaced sample CMV60 with CMV15, which is of the same lithofacies (Lt1) but better reflects the differences observed between AF demagnetization and thermal demagnetization.

Figure 12D: typo in edifice?

Author response: This figure has been revised so that the text has been removed to limit the presentation of redundant information. We feel there is an adequate explanation of the stages of the eruption in the text and figure caption and is not needed in the figure itself.

Other Modifications:

We have revised the text moderately for clarity and brevity. Subheadings of lithofacies and lithofacies associations have been removed to make the manuscript less choppy, as suggested by the editor Jim Gardner.

The discussion section has been reorganized and revised into two sections (rather than four in the previous version). This decision was made to reduce the repetition of information and focus on our major findings and implications. Section 8.1 is now 'Explosive Onset to Glaciovolcanic Eruption'. This section contains our detailed evidence for the explosive eruption at Cracked Mountain which makes it a unique glaciovolcanic eruption worthy of documentation. The end of section 8.1 contains the abbreviated eruptive succession (depicted in figure 12) after the explosive onset. Section 8.2 is now 'Paleoenvironmental implications'. This section presents our evidence-based modelling for a reconstructed cordilleran ice-sheet extent and timing within the mid-Pleistocene. Here we drive home the importance of our investigation of Cracked Mountain volcano as a land-based proxy that can be used to inform on the paleoclimate of SW British Columbia.

Figures 10A and B have been modified so that their x-axis (SiO_2 wt %) are in the same range. Fig 10C has been modified, and now data are normalized to a Chondrite, as we feel this is more conventional with other literature.

Figure 13 has been revised for readability with larger text and less white space.

Figure 14 has been revised with an indication of our 'preferred' age of 425 ka as a dashed line.

Tables 3, A1, and A2 have been revised to include 2s analytical precision values, and all values are now reported to their significant digits.

Appendix Fig A1 has been removed as we no longer feel it is necessary, as the data can be presented in table format.

Explosive Glaciovolcanism at Cracked Mountain Volcano, Garibaldi Volcanic Belt, Canada

Martin A. Harris[1]

James K. Russell[1]

Rene Barendregt[2]

Lucy A. Porritt[1]

&

Alex Wilson[3]

[1]Volcanology and Petrology Laboratory, EOAS, University of British Columbia

[2]Department of Geography, University of Lethbridge

[3]Minerva Intelligence

Journal of Volcanology and Geothermal Research

Submitted September 8, 2021

Revised, January 10, 2022

Corresponding Author: Martin Harris: mharris@eoas.ubc.ca

Abstract

Cracked Mountain (CM) is a basaltic volcano within the northern extension of the Cascade volcanic arc into southwest, British Columbia, Canada (i.e. Garibaldi Volcanic Belt) and is dated at 401 ± 38 ka ($^{40}Ar/^{39}Ar$). The edifice covers an area of ~1.5 km^2 and has a volume of 0.18 km^3. The volcano features steep margins with local relief of ~250 m (1,650 m a.s.l), is dissected by abundant 0.5 to ~20 m wide extensional cracks with depths up to 30 m, and has a highly eroded top. The edifice is dominated by massive to poorly stratified, moderately to pervasively palagonitized lapilli tuffs, comprising vitric fine ash to lapilli. Juvenile pyroclasts have blocky to highly vesiculated shapes consistent with a phreatomagmatic (i.e. explosive) origin. The lapilli tuffs are intruded by and mingled with coherent to disaggregated lobes of peperitic pillowed lavas. Contacts between lapilli tuff and peperitic pillowed lava show soft-sediment deformation and in-situ quench-fragmentation indicating that the tephra was both unconsolidated and water-saturated at the time of ~~magma~~ intrusion. Local stacks of pillow lava are found on the margins of the edifice. More than fifty, 0.5 to 3 m ~~thick~~wide dykes intrude CM stratigraphy and display, either, peperitic pillowed margins or sharp, chilled margins and columnar-jointing. Measurements of paleomagnetic directions (9 sites) were made for all CM lithofacies and record a single-pole direction ~~(i.e. within uncertainty)~~ indicating ~~that the edifice likely represents~~ a single monogenetic eruption. A glaciovolcanic origin is strongly suggested by the abundant subaqueous lithofacies (i.e. palagonitized tephra, pillows, peperites) and the physiographic setting of the edifice which is well above any drainage that could sustain a standing body of water. The elevation of CM and depth of surrounding valleys indicate syn-eruptive confinement by a paleo-ice sheet that was ≥ 850 m thick. The edifice shape, size, and surrounding topography suggest a 'leaky' paleolake system ~~was~~ capable of supporting ~0.36 km^3 of water. The glaciovolcanic origin and the absolute ($^{40}Ar/^{39}Ar$) age of CM ~~represents~~represent an important record of the Cordilleran Ice sheet (CIS) in southwestern BC during the mid-Pleistocene.

Key Words: Glaciovolcanism, Subglacial, Phreatomagmatic, Basalt, Englacial Lake, Ice-Sheet

1. Introduction

The Garibaldi Volcanic Belt (GVB) is the northern segment of the Cascade Volcanic Arc (Roddick and Souther, 1987; Green et al., 1988; Hildreth, 2007). GVB volcanic deposits range from Pleistocene to Holocene in age and result from subduction of the Juan de Fuca plate beneath the North American Plate (Roddick and Souther, 1987; Green et al., 1988; Hildreth, 2007). Southwest British Columbia has a protracted history of multiple glaciations, with cycles of advancing and retreating ~~continental~~cordilleran ice sheets throughout the Pleistocene (Clague, 2009; Clague and Ward, 2011). As a result, the GVB hosts numerous glaciovolcanic landforms. Prior studies concerning glaciovolcanism have focused on the Mount Garibaldi volcanic field (e.g., Mathews, 1952; Wilson et al., 2019), the Mount Cayley volcanic field (e.g., Kelman et al., 2002; Kelman, 2005), the Mount Meager volcanic complex (MMVC) (e.g., Wilson and Russell, 2017, 2018), the Salal Glacier volcanic complex (e.g., Lawrence et al., 1984; Wilson and Russell, 2018), and the Bridge River volcanic field (e.g., Roddick and Souther, 1987; Wilson and Russell, 2018).

Cracked Mountain is a ~~~0.18 km^3~~ basaltic volcano situated on the southern flank of the MMVC and originally identified by Read (1979) as part of the Mosaic Assemblage~~.~~ (i.e., undivided, Pleistocene aged, basalts within the MMVC). Here, we present a new dataset including a map of volcanic lithofacies, petrographic and geochemical characteristics of the deposits, geochronometric (^{40}Ar /^{39}Ar) age estimates, and paleomagnetic directions of all lithofacies. Collectively, these data inform on the physical volcanological evolution of the Cracked Mountain (CM) volcano. Our analysis shows CM to have a glaciovolcanic origin (Kelman et al., 2002; Smellie, 2007; Edwards et al., 2009) involving sustained eruption within an englacial lake. The lithofacies and their stratigraphic relationships indicate an explosive onset to the eruption ~~onset~~ dominated by phreatomagmatic activity that transitioned to effusive ~~eruption~~activity expressed by intrusions and lavas. We use the geometry of the CM edifice (i.e. shape and size) and the distribution of lithofacies to reconstruct the eruptive history of the glaciovolcanic edifice and to constrain the ~~minimum~~ thickness and distribution of the enclosing ~~paleo~~ ice sheet. Our findings contribute to a larger story of glaciovolcanism within the GVB and ~~understanding the~~ paleoclimate ~~of~~reconstructions for SW British Columbia.

2. Geological Background

The Mount Meager volcanic complex is situated 160 km north of Vancouver in SW British Columbia (Fig. 1) and is one of eight major centres and volcanic fields comprising the GVB (Fig. 1A). Recent GVB geochemical and petrological studies show increases in melt alkalinity and a decrease in slab-derived signatures moving northward in the GVB (Green and Sinha, 2004; Mullen and Weis, 2013). In particular, the MMVC, Salal Glacier volcanic complex, and Bridge River volcanic field show a heightened primitive signature compared to the southward GVB and the High Cascade volcanoes. These findings suggest that the Nootka Fault, located Northwest of the Bridge River cones (Fig.1A), may mark the terminus of the Juan de Fuca subduction where a window between the Juan de Fuca and Northward Explorer plate allows upwelling of asthenospheric melts under the northernmost GVB centres (Mullen and Weis, 2013).

The MMVC (Fig. 1B) contains Pleistocene to Holocene basalt to rhyolite overlying basement igneous and metamorphic rocks of the Coastal Plutonic complex (Fig 1B) (Woodsworth, 1977; Read, 1979; Green et al., 1988). The MMVC is also host to the youngest GVB eruptive deposits, namely the 2350 B.P. Pebble Creek formation (Hickson et al., 1999; Stewart et al., 2008). Intermediate to felsic lavas are dominant within the Mount Meager Massif, however, localized mafic centres are present in the north (Lillooet Ridge and River), west (Mosaic Ridge), and southwest (Cracked Mountain and Elaho Valley) regions of the volcanic complex (Fig. 1B) (Read, 1979, 1990; Harris and Russell, 2021). The ages of the Mosaic Ridge basalts and Elaho Valley basaltic andesites are ~90 and 140 ka respectively (Woodsworth, 1977; Green et al., 1988).

3. Cracked Mountain Physiography and Morphology

The Cracked Mountain volcano unconformably overlies basement granodiorite (Bg) and schist (Bs) of the Gambier and Cadwallader Groups respectively (Fig. 2A) (Read, 1979). The volcanic deposits form a slightly asymmetric, NE-SW trending ~250 m thick ridge that is ~1,300 m long and ~1,000 m wide~~.~~ covering an area of ~1.5 km^2 and having a present-day volume of ~0.18 km^3. The summit of CM rises to 1,650 m above sea level (a.s.l.) and the margins reach elevations as low as 1,250 m (Fig. 2A). CM is surrounded by steep valleys of the Meager Creek

and Elaho River tributaries to the north and west respectively (Fig. 3). Extensional cracks dissect the entirety of CM (Figs. 2A; ~~3A~~3B), ranging from 0.5 to > 20 m in width and up to 30 m in depth. The fractures form parallel clusters that commonly trend perpendicular to the downslope direction. All CM lithofacies are offset and displaced by cracks. No glacial deposits (i.e. till, erratics) are found within cracks, suggesting a post-eruptive and post-glacial origin.

The shape and surface features of CM show evidence of glacial enveloping and scouring. The present-day surface is littered with cobble to boulder-sized granitic erratics and some locations have been smoothed and striated in a SW direction. These findings show that post-eruption Cordilleran Ice Sheets have reached elevations greater than the summit of CM. The margins of CM are cliffs up to 40 m high, which is unusually thick for basaltic lava (e.g., Edwards et al., 2015). We interpret this morphology to be a result of syn-eruptive glacial confinement and subsequent erosion. There is no evidence of ice-abutment in the form of laterally facing, hackly, or irregular jointed lavas (e.g., Lescinsky and Fink, 2000; Kelman et al., 2002) suggesting that the outermost CM margins result from post-eruptive glacial erosion rather than reflecting primary lava-ice contact surfaces.

4. Volcanic Lithofacies

We recognize ten CM lithofacies (Table 1) that include, both, volcaniclastic and coherent lithofacies. All volcanic deposits are olivine and plagioclase porphyritic and differ only in their groundmass textures ranging from holocrystalline, hypocrystalline, and quenched. The terminology used to describe grain size and componentry of volcaniclastic rocks is after White and Houghton (2006).

4.1 Volcaniclastic

~~4.12 Lapilli Tuff (Lt_{1-3})~~

CM lapilli tuffs (Lt_{1-2}) (Table 1) form the stratigraphically lowest (Fig. 2B) lithofacies. Observed thicknesses range from 0.5 m to < 6 m. Lt_1 is massive, moderately- to poorly sorted, and is observed throughout the CM edifice from its base to its summit (Fig. ~~2A~~2; 4A). Lt_1 is ~~comprised~~composed of dense and blocky to highly vesiculated and cuspate vitric juveniles and contains 5-35% lapilli-sized clasts supported in a vitric ash matrix. Lt_1 is commonly intruded by dykes (Ld_{1-2}) and mingled with peperitic lobes (Lpi; Table 1) (Fig. 5). In some locations, soft-

sediment deformation of Lt_1, in the form of squeeze-up pipes, is observed. Lt_2 outcrops in the SE and N sections of CM and, by comparison, are thinly bedded, well-sorted (Fig. 4B). Beds of ultra-fine ash are up to 5 cm thick and dip shallowly in the downslope direction. In some outcrops, microfractures offset laminated beds, and truncated and shallow cross-beds are also observed. Lt_2 is commonly observed as 1-2 m layers within thicker, massive Lt_1 exposures (Fig. 2B; 4B) and displays fining upward grain sizes. Lt_3 are locally stratified as defined by accumulations of lapilli and bomb-sized, fluidal to blocky, vesiculated (<60%) spatter clasts (Fig. 4C). The clasts are supported by a well-sorted, vitric ash matrix. Two small outcrops of Lt_3 are located at upper elevations (i.e. high in stratigraphy) in the central and NE sections of the CM.

~~4.13 Peperite (Pi)~~

Peperite (Pi) deposits, as defined by White et al., (2000) and Skilling et al., (2002), are volcaniclastic deposits resulting from the mingling of magma with wet, unconsolidated sediments. At CM, peperites occur as fragmented, globular to blocky components of vitric basalt supported by ash and lapilli tuff matrix (Figs. 2B; 6). Peperite deposits are distributed along the margins of the peperitic intrusive bodies (Lpi). We distinguish lithofacies Pi from Lpi (Table 1) as volcaniclastic and coherent, respectively. The thickness of peperites varies from a few cm to 2-3 m away from the margins of Lpi. Peperites rarely outcrop at the present-day CM surface but are commonly exposed in cracks at all locations of the volcano.

~~4.14 Tuff Breccia (Tb)~~

Tuff breccias (Tb) blanket much of the topography in the central and north regions, are the dominant map unit (Fig. 2), and obscure stratigraphically older volcanic lithofacies. At higher elevations, tuff breccias form thin 1-2 m-thick deposits that progressively thicken (<10 m) downslope (Fig. 7). Tuff breccias are massive and clast-supported, featuring monolithic lapilli-to block-sized lithic components. These lithics are olivine-and-plagioclase porphyritic lava fragments of Lpi, Ls, and Lp, where ~30-40% show rounded chilled margins. Minor yellow ash-sized interstitial sediment is present between breccia clasts. Rarely, block and lapilli-sized, rounded Lt_1 lithics are present (Fig. 7B).

4.2 Coherent

~~4.21 Peperitic Pillowed Lava (Lpi)~~

The peperitic pillowed lava unit (Lpi) (Table 1) comprises coherent, mingled lavas that intrude volcaniclastic deposits (Lt) across all elevations and locations of the edifice (Fig. 2). Lpi is a mappable unit ~~and is distinguished~~distinct from coherent pillow lavas (Lp; Table 1) ~~where Lpi intruded saturated sediments and Lp~~ formed through subaqueous effusion. ~~Lpi is commonly exposed in cracks as~~The Lpi unit occurs where magma has been injected into water-saturated sediments and forms massive globular bodies up to 15-20 m across and 10-15 m high, ~~comprised of~~comprising chilled, subrounded lobes (Fig. 5A and B). Additionally, Lpi is often associated with 'blooming' dykes (Ld_1) (Fig. ~~5C).~~5C) that transition from ~0.5-1 m wide intrusions into <5 m wide, "pillowed" masses. Since Lpi intrudes and pillows into lapilli tuff (Lt) (i.e. host sediments) we interpret these lithofacies to be 'peperitic' intrusions~~. Here we use the adjective "peperitic",~~ after White and Houghton (2006) ~~which has a genetic connotation describing deposits resulting from intrusion and mingling of magma and unconsolidated~~.

~~.~~

~~4.22 Pillow Lava (Lp)~~

Pillow lava deposits (Lp) (Table 1~~) comprise individually stacked radial and quenched lobes,~~), makeup ~20% of the edifice, and are the dominant lithofacies exposed at the edges of CM (Fig. 2). Pillow lava ~~outcrop~~outcrops at the present-day, high elevations of CM (Figs. 2A) as 1-3 m thick piles and increases to ~ 10-40 m thick along the cliffs at the outer edges of the volcano (Figs. 2B; 8A and B). Individual pillows are bulbous, with diameters up to 50 cm (Fig. 8C). Interstitial quench-fragmented vitric sediment fills void spaces between intact pillows in some outcrops (Fig. 9A). Large radial columnar jointed pods up to 3 m in diameter make up a lesser amount of the lithofacies. Stratigraphically, Lp is overlain by tuff breccia (Tb), is cut by dykes (Ld_2), and is observed to overlie outcroppings of lapilli tuff (Lt_1) at the base of the edifice (Fig. 2B).

~~4.23 Sheet Lava (Ls)~~

Blocky and columnar jointed remnants of sheet lava (Ls) (Table 1) are preserved at the highest elevations of CM near the central and eastern regions (Fig. 2A). Sheet lava outcrops are small, ranging from ~10-30 m across, and 1-2.5 m thick. The sheet lavas have coarse columnar

joints up to 0.4 m in diameter and occur at the present-day surface of CM. The tops of the sheet lavas are ~~commonly glaciated as indicated~~scoured by SW trending glacial striae and covered with erratics (Fig 8D).

~~4.24 Dykes (Ld_{1-2})~~

Over 50 dykes (Ld_{1-2}) intrude the CM volcano (Fig 2A). The dykes are predominantly subvertical and have widths ranging from 0.5 to 3 m in width and up to 100 m in length. The dominant trends of the dykes strike E-NE and W-NW. Dykes were divided into two groups based on their margins: 1) Ld_1 (Table 1) have poorly defined, glassy, pillowed, or peperitic margins where they contact bodies of Lpi (Fig. 5C), and 2) Ld_2 (Table 1) have sharp, chilled, and columnar jointed margins where they intrude all other lithofacies. Ld_1 is prevalent in the central and high elevations of the edifice and is best exposed through extensional cracks. Ld_2 outcrop sporadically ~~outcrop~~ in the central high elevations of CM ~~and are high in density~~, as well as, along the eastern ~~margins~~margin of the edifice where they intrude subvertically ~~through the~~ stacked ~~walls~~piles of Lp.

5. Lithofacies associations

The ~~transitional eruptive history~~topmost portion of CM ~~involving explosive, effusive,~~edifice and ~~intrusive activity produced non-uniform deposition of all volcanic lithofacies. The deposits~~ uppermost stratigraphic units are ~~not stratigraphically ordered in a planar fashion (i.e. a layer-cake model). Instead,~~heavily eroded which precludes us from identifying the ~~build~~upprecise location and nature (e.g., fissure, cone, etc.) of the ~~volcano~~ vent. However, we expect that the vent was ~~both lateral,~~near the present-day summit (elev. ~1580 m) where ~~eruptive deposits spread out~~, within a 100 m radius, we find a multitude (~10) of cross-cutting dykes intersecting the upper surface of the edifice. The volcano is volumetrically dominated by subaqueous style lithofacies that result from and record an explosive onset to the eruption followed by effusion (e.g., pillow lava) and intrusion (e.g., dykes). Furthermore, rather than a simple layer-cake stratigraphy, the CM volcano grew: i) laterally where deposits source from higher elevations ~~down~~and extend to the margins of the edifice, and ~~endogenous, through peperitic~~ii) endogenously by abundant intrusions ~~and dykes. The~~within the volcaniclastic pile. Based on the detailed stratigraphic ~~relations are observed through the excellent crack exposures~~

~~and allow us to determine~~relationships described above, we define four ~~dominant~~main lithofacies associations (A-D) (Table 2).

~~5.1 Lithofacies Association A~~

Lithofacies association A comprises Lt_1, Lpi, and Ld_1 (Table 2). Lt_1 is intruded by Lpi and Ld_1 at all elevations of the edifice, including exposures at the base of CM (Figs. 2B; 5). Ld_1 is observed to be in genetic relation to Lpi (Fig. 5C). Lt_1 outcrops at all elevations of CM, and the deposits are pervasively palagonitized and lithified (Stroncik and Schmincke, 2002). The mingling of Lpi within Lt_1 and examples of soft-sediment deformation indicate that Lt_1 was saturated and unconsolidated at the time of intrusion. Additionally, the margins of Ld_1 are often poorly defined and pillowed, further suggesting a saturated slurry-like host rather than a cooled and lithified host at the time of intrusion. Lastly, Ld_1 is often seen tangential to 'blooming' Lpi, suggesting that these two intrusive bodies are temporally related. Further petrographic similarities (i.e. olivine and plagioclase phenocrysts) substantiate a co-genetic relationship between Lpi and Ld_1. This lithofacies association reveals that unconsolidated ash and lapilli were intruded by peperitic bodies, processes that require a water-saturated eruptive environment. These stratigraphic relations imply an age succession of $Lt_1 > Lpi \geq Ld_1$.

~~5.2 Lithofacies Association B~~

Lithofacies association B comprises Lpi and Pi (Table 2); at CM peperite deposits (Pi) are always spatially associated with masses of intrusive pillow lava (i.e. Lpi; Fig. 6). We interpret these occurrences as fuel-coolant interactions (FCI) where the sudden contact of hot magma (e.g.~~,~~., fuel) with cold, saturated sediment (e.g.~~,~~., coolant) generates a vapour film around the intruding body (i.e. Lpi) (Doyle, 2000; Hooten and Ort, 2002; Martin and Németh, 2007). Within the vapour films, instabilities may arise, causing local phreatomagmatic fragmentation along the borders of the intrusion. Regions that experienced more stable vapour films result in globular peperite texture (Fig. 6C) while areas with less film stability produce blocky peperite textures (Figs. 6D) (Martin and Németh, 2007). ~~Most peperite deposits form along the margins of syn-volcanic intrusions and we take their widespread occurrence at or near the present-day surface of CM as an indicator of substantial post-eruptive erosion (e.g., Rosa et al., 2016).~~Most peperite deposits form along the margins of syn-volcanic intrusions. The field relations for Lpi

and Pi show a contemporaneous origin, with both lithofacies forming as a result of intrusion into wet, unconsolidated lapilli tuffs.

~~5.3~~ Lithofacies ~~Association C~~

~~This~~ association C comprises Tb, Ls, Lp, Lpi, and Lt (Table 2). The tuff breccia (Tb) blankets the upper surface of CM and contains a large proportion (<50%) of sheet lava (Ls) lithics, as well as moderate (30-40%) subrounded lithics of pillowed lava (Lp and Lpi), and minor (>5%) subrounded blocks of Lt (Fig 7). The high volume of Ls lithics entrained within the widespread tuff breccias is our best line of evidence that the sheet lavas preserved at higher elevations were originally more extensive and volumetrically abundant. Post-eruptive erosion (i.e. glacier erratics and scour marks; Fig. ~~The Tb matrix is comprised of~~8D) and collapse (i.e. extensive network of extensional fissures) provide a reasonable explanation for the relatively small remnant outcroppings of the Ls unit. The Tb matrix comprises moderately palagonitized, explosively derived fine ash, quench fragmented ash and lapilli, and coherent lapilli lithics. These findings suggest that Tb are syn-eruptive debris flows ~~comprised~~composed of previously erupted volcanic lithics. The degree of palagonitization alteration throughout the unit ~~indicates~~suggests subaqueous deposition ~~and may also have played a role in destabilizing the edifice slopes~~ (Schiffman et al., 2006). ~~The high volume of Ls lithics entrained within the widespread tuff breccias is our best line of evidence that sheet lavas made up a larger degree of edifice volume than what is preserved at the highly eroded present-day surface. Evidence of post~~The tuff breccias incorporate clasts derived from all other earlier stratigraphic units which, combined with other stratigraphic relationships, suggests the succession ~~eruptive erosion (i.e. glacier erratics and scour marks; Fig. 8D) may explain why presently, Ls are only found as small remnant outcroppings. Given that the tuff breccias are comprised of earlier eruptive lithics (and not juveniles) this association suggests a temporal succession of~~ Lt>Lpi≥Lp>Ls>Tb.

~~5.4~~ Lithofacies ~~Association~~association D

comprises Ld_2 ~~is associated~~ with all other CM lithofacies (Table 2). At CM, Ld_2 intrudes through all other lithofacies with sharp, columnar jointed margins, including cross-cutting Ld_1 in select locations. These contact relations indicate that Ld_2 is the latest preserved lithofacies from

the CM eruption. This last association suggests a temporal succession of Lt>Lpi=Pi≥Ld_1≥Lp>Ls≥Tb>Ld_2.

6. Chemistry and Petrography

6.1 Petrography

Detailed mineral abundances and componentry based on standard polarizing light and scanning electron microscopy (Philips XL30) for all CM volcanic lithofacies are listed in Table 1. All coherent CM samples are olivine and plagioclase porphyritic, with glomeroporphyritic clots visible in hand samples. A smaller population of samples also contains phenocrystic augite. Petrographically, the pillowed dykes (Ld_1) have similar mineralogy as found in pillowed (Lpi) and most sheet lavas (Ls). Jointed-dykes (Ld_2) commonly contain phenocrystic augite as do a small proportion of pillow lava samples (Lp). Olivine phenocrysts are subhedral and unzoned. Plagioclase phenocrysts are tabular and moderately zoned, with a very minor percentage (>5%) showing sieve textures. When present, augite crystals are subhedral to anhedral.

Volcaniclastic samples are distinguished by sorting, grain size, structures, and componentry. Lapilli tuffs (Lt_{1-3}) are ~~comprised~~composed of monolithic vitric juvenile fine ash and coarse lapilli (Figs. 9B-H) and microlitic tachylyte juvenile pyroclasts (5-30%). Intact to fragmented crystals of olivine and plagioclase are observed within the matrix of Lt_{1-3}. Juvenile shapes range from blocky to highly vesicular (~60-70%) (Figs. 9B-H). Interstitial sediments are observed between coherent Lp clasts but are notably different (i.e. coarse, jig-saw fit clasts compared with Lt_{1-3} ~~()~~(e.g. Fig 9A).

Tuff breccia (Tb) componentry is highly variable. Tb is dominated by clasts of basalt (Lpi, Ls, Lp) and contains minor blocks of Lt_1 within a matrix of vitric ash and lapilli. Tb matrix is overall coarser than Lt_{1-3} although still contains abundant blocky and highly vesiculated juveniles.

6.2 Geochemistry

Whole-rock major and trace element geochemical compositions were measured for 26 samples by X-ray fluorescence (XRF) analyses of fused discs and by inductively coupled plasma-mass spectroscopy (ICP-MS), respectively. Samples span all CM volcanic lithofacies (i.e. dykes, sheet and pillow lavas, and juvenile vitric-lapilli). Representative compositions of

whole rocks and glasses are reported in Table 3; analytical uncertainties are based on replicate analyses done by Acme Analytical Labs Ltd., Vancouver, BC, Canada. A subset of samples was analysed for FeO volumetrically by ALS Canada Ltd., North Vancouver, BC, Canada. Appendix A contains the full data set and additional analytical details.

Figure 10A illustrates the chemical diversity of CM samples after Le Bas et. al, 1986 classification of volcanic rocks. All CM samples are subalkaline (Irvine and Baragar, 1971) but display moderate spread in SiO_2 (~47-51 wt.%) and Na_2O-K_2O (~3-4 wt. %). The spread in chemistry observed in Fig. 10A correlates with groups of samples having different phenocryst contents. Samples that contain minor modal abundances of augite (in addition to olivine and plagioclase) are typically higher in SiO_2 and Na_2O-K_2O wt. %. However, we find no significant differences in mineralogy or chemical compositions that correlate with the stratigraphic position.

Fig 10B shows Mg#s (molar MgO/ (MgO +FeO*)∗100) of CM samples with relation to SiO_2 wt.%. Within the Cascade arc, volcanic rocks having Mg# > 60 are considered "primitive" indicating limited crustal influence (Green and Harry, 1999; Mullen and Weis, 2013). Our results show CM samples range from Mg# ~55-67 with the majority of samples (~80%) between 60-66.

~~CM rare earth elements (REE) are normalized to a primitive mantle (Sun and McDonough, 1989) and shown in Fig. 10C. All CM samples show similar anomalies (i.e. positive Eu^{2+}, negative Y^{3+}). Little variations in trace element concentrations are observed between samples, suggesting a similar mantle source for all CM eruptive deposits.~~

Cracked Mountain rare earth elements (REE) shown in Fig. 10C normalized to chondrite composition after Sun and McDonough (1989). There is little variation in trace element concentrations between samples, including similar anomalies (i.e. positive Eu^{2+}), suggesting a similar mantle source for all CM deposits.

7. Geochronometry

7.1 Radiogenic $^{40}Ar/^{39}Ar$ Results

Two CM samples (MH-19-055, 031) were selected for $^{40}Ar/^{39}Ar$ radiometric dating at the WiscAr Geochronology Labs, University of Wisconsin-Madison, USA. The holocrystalline dyke sample (MH-19-031) proved to be non-measurable because of excess argon trapped in the plagioclase minerals. This is a common issue with basaltic dykes (of young ages) (Brian Jicha, pers. comm. 2021) and with subglacially erupted deposits of all compositions (Clay et al., 2015).

The second CM sample (MH-19-055) was collected from the radially jointed interior of a pillow lava outcrop. This sample contained low radiogenic argon but the analysis was still possible through twenty-four heating steps with moderate uncertainty. The results yielded a plateau age of 401.6 ± 38.1 ka for crystallization of the groundmass (Fig. B1). Errors are quoted at a 2σ (95% confidence) level and are propagated from all sources except for mass spectrometer sensitivity and the age of the flux monitor. Appendix B contains analytical procedures used and table B1 contains complete measured data for heating steps.

7.2 Paleomagnetic Methods and Results

A total of nine sites across the CM edifice were selected for ~~sampling at CM, with the objectives of gaining representative data from approximately~~ the paleomagnetic study. The sites were chosen to span the entire stratigraphic sequence (i.e. oldest to youngest ~~CM lithofacies. One sample~~) and one site (Site 2) was replicated ~~to test~~ for field and lab reproducibility~~. All samples were drilled into volcanic lithofacies~~ (Table C1). We preferentially sampled units that cooled quickly, thus locking in the geomagnetic field orientation at the time of emplacement (e.g., Johnson et al., 2008). Efforts were made to sample ~~in situ~~only intact outcrops ~~and avoid~~thereby avoiding areas suspected of ~~obvious~~ post-emplacement ~~rotation. Standard~~movement. Approximately eight standard 2.5-cm-diameter paleomagnetic cores were ~~drilled in the field. Approximately eight cores were taken from most sites~~collected from each site and a minimum of three cores from each outcrop. Each sample was oriented using a magnetic compass, and where possible a sun compass was used in conjunction with magnetic orientations.

CM samples were analyzed at the paleomagnetic laboratory at the University of Lethbridge, Alberta. Magnetic susceptibility was determined with a Sapphire Instruments (SI-2B) susceptibility meter. The magnetization of each sample was measured with an AGICO JR-6A spinner magnetometer before demagnetization and again after each level of stepwise demagnetization. CM samples were held in magnetic shields following field collection and between laboratory measurements. All samples were subjected to alternating field (AF) demagnetization, performed using an ASC Scientific D-2000 demagnetizer with a three-axis manual tumbler, and carried out at 10 milli-tesla (mT) steps (up to 200 mT). Thermal demagnetization was carried out at 100, 200, 300, 400, 500, 525, 550, and 580 °C, using an ASC Model TD48 dual-chamber thermal demagnetizer to confirm that alternating field

demagnetization was sufficient to resolve the primary remanence. Directions of characteristic magnetization were determined for each sample by principal component analysis (Kirschvink, 1980) using Remasoft version 3.0 (Chadima and Hrouda, 2006). Mean directions of characteristic magnetization were calculated for each site and an overall mean was also calculated (Appendix C; Table C1). All samples were subject to stepwise AF demagnetization and principal component analysis and mean directions were calculated from the AF data only.

All paleomagnetic samples are normally magnetized (Fig. 11A; Table C1). The ~~site~~ mean directions of sites are consistent for eight of nine sites, where all eight sites plot within the uncertainty circle (α_{95}) about the overall mean (N=8) with a declination of ~~346.54~~347.3˚ and inclination of 76.~~54~~6˚, and Fisher precision factor of k = 351, α_{95} = ~~2.99~~3.0° (Fig. ~~12A~~11A). Typical, well-behaved demagnetization characteristics are shown for samples from Lt_1 and Ld_1 respectively in Figs 11B and C.

All paleomagnetic samples produced stable directions of magnetization following stepwise demagnetization. Alternating field demagnetization, applied to all specimens, exhibited linear decay to the origin on orthogonal projections (Fig. ~~11A~~11B and ~~B~~C). The median destructive fields range from 20–80 mT and final directions are often stable up to 200 mT alternating field demagnetization (see ~~CMV060A~~CMV015A, Fig. 11B) indicative of single-domain magnetite. Thermal demagnetization showed complete demagnetization at 550 to 580 °C, typical of fine-grained (single domain) magnetite as the magnetic carrier (see CMV029, Fig. 11C). Note that single-domain magnetite is the optimal magnetic mineral and grain size for producing reliable paleomagnetic directions. The magnetic susceptibility values of CM volcanics range from 0.4-1.0 x 10-3 SI (median value of 0.5 x 10-3 SI) for the flows composed of pyroclastic density currents and 2.4-16.4 x 10-3 SI (median value of 4.5 x10-3 SI) for dykes. Mean natural remanent magnetization for CM volcanics is 9.4 A/m (range 0.4–22.0 A/m). ~~These findings indicate that the bulk of the sampled lithofacies at CM have the same emplacement age (i.e. monogenetic).~~

~~One site (Site 1; Table C1) provided seven samples that were outliers compared to the results obtained from the eight other sites (2-9). The sampling location for Site 1 was from basal lava (Lp) exposed below the SE cliff margin of the edifice. Of the seven cores analyzed from Site 1, we accept three as likely due to edifice rotation not evident in the field at the time of sampling. These three samples gave coherent results with a mean declination and inclination of~~

~~34.37˚ and 72.88˚ respectively. From our observed crack orientations (e.g. Fig. C1) we believe the edifice is collapsing in the downslope directions. This suggests that Site 1 may have experienced east (southeast) trending rotation. Based on a comparison of the stereographic orientation of Site 1 mean data (from three coherent samples) with the whole CM mean data, we find that a rotation of ~12˚E is observed (Fig. C1), which is consistent with our interpretation of extensional collapse. Additionally, we calculated the approximate crack width from the ~12˚ of interpreted rotation and thickness of block (e.g. deposit thickness above basement) to be ~20 m. Again, this calculated crack width is consistent with observed crack widths seen along the outer margins of CM, and further supports our interpretation of Site 1 paleomagnetic data. The remaining four samples collected from Site 1 returned highly dispersed results that were inconsistent with both the mean CM magnetic data of Sites 2-9 and the three Site 1 samples that plot within our plausible edifice collapse direction. We interpret the remaining four samples to be a result of the reorientation of blocks (i.e. not in-situ to edifice lava wall) not obvious at the outcrop at the time of sampling.~~

The common pole direction obtained for all volcanic units, including the latest dykes, implies a common eruption age indicating a monogenetic origin for the volcano. Furthermore, the data from each site showed no indication of rotation or tilt as the mean direction is within the expected paleosecular variation (see mean of sites 2-9 and GAD inclination for sampling latitude, Fig. 11A, and Table C1). The sole exception was Site 1 (Table C1) where the seven cores record a different mean pole direction compared to the other eight sites (2-9). Site 1 is a lower elevation cliff-side exposure of pillow lava (Lp) on the SE margin of the edifice. Of the seven cores, three can be ascribed to post-emplacement rotation and yield coherent results with a mean declination and inclination of 34.4˚ and 72.9 respectively. The rotation is likely due to partial extensional collapse and, relative to the mean pole direction for the CM edifice, we calculate a downslope rotation of ~12˚E (Fig. C1). This rotation has a calculated maximum crack width of ~20 m which accords well with the observed fissures found on the outer margins of CM (e.g., Fig. 3B).

8. Discussion

~~8.1 A glaciovolcanic eruption within an englacial lake~~

Our mapping and analysis suggest CM is a monogenetic edifice with no evidence of time lapses during the eruption. The results of paleomagnetic analyses concur with our field observations that the varying lithofacies were emplaced in one paleomagnetic moment (< 1,000 years; Turner, 1987; Barletta et al., 2010; Lisé-Pronovost et al., 2013) at 401 ±38 ka based on our best $^{40}Ar/^{39}Ar$ age determination. CM lithofacies (i.e. pillow lavas, palagonitized tuffs, and peperites) indicate a subaqueous eruptive paleoenvironment, however, the edifice is situated in an alpine setting with extremely steep-sided valleys on all sides (Fig. 3). There are no reasonable physical barriers (i.e. mountains or ridges) to provide a paleo-closed catchment to form an alpine lake, thus, we ascribe a glaciovolcanic origin. CM lacks the lithofacies succession in a "Classic" mafic tuya model (e.g., pillow effusion, hyaloclastites, lava-fed deltas, and capping lava) (Smellie, 2007; Jakobsson and Gudmundsson, 2008; Edwards et al., 2015). The Russell et al., (2014) descriptive classification would describe CM as a transitional, tephra-dominated, tuya.

The CM volcanic succession is ~250 m thick and subaqueous lithofacies outcrop at elevations as high as ~1,650 m a.s.l where they have relief of ~800 m above the major drainages. At the highest elevations of CM (~1,600-1650m a.s.l), we find small remnant subaerial sheet lavas (Ls) but no evidence of preserved 'passage zones' (i.e. surfaces that mark transitions between subaqueous and subaerial depositional environments during volcanic eruptions) (Jones, 1970; Smellie, 2006; Russell et al., 2013; Edwards et al., 2015). This provides strong evidence that the englacial meltwater lake was sustained throughout the majority of the eruption and the lake surface elevation continued to rise with the growth of the edifice. The absence of lava-fed delta sequences containing pillow breccias at Cracked Mountain (i.e. aggradation of volcaniclastic material from lava flowing into the water; Edwards et al., 2015) suggests Ls formed as overlapping effusions of subaerial lava (e.g., Skilling, 2009; Russell et al., 2013) where the englacial lake had partially drained at a later time in the edifice buildup.

The present-day Ls outcrops are small; however, we find substantial Ls lithics entrained in the thick, massive Tb that cover much of the CM surface. These findings suggest a significant volume of subaerial lava erupted during the late-stage edifice formation. Two scenarios would give rise to the subaerial capping lavas: 1) The edifice grew above the paleolake level, becoming emergent, where a passage zone would denote the maximum lake level, or 2) the water level dropped (via drainage) giving rise to dry, subaerial eruptive environment. In the latter case, the subaerial lavas would mark the minimum height that lake level reached (i.e., overlap) (Russell et

~~al., 2013). We favour the second scenario of overlap lavas because we find no definitive passage zones that would suggest subaerial lavas aggraded into water (i.e. lava-fed-deltas) and our models of meltwater produced versus paleolake capacity suggest a moderately 'leaky' lake system must have been present in the later stages of the eruption (see section 8.4). Thus, the elevation of Ls (~1,650 m) marks the minimum level for the paleo-englacial lake.~~

~~8.2~~8.1 Explosive Onset to Glaciovolcanic Eruption

The lapilli tuff deposits (e.g. Fig 9B-H) ~~are comprised of~~comprise coarse to fine ash (>100 μm) particles that are commonly highly vesiculated (<60%). The abundance of fine ash in CM Lt deposits suggests explosive magmatic and/or phreatomagmatic fragmentation (Zimanowski et al., 1991; White and Valentine, 2016; Latutrie and Ross, 2020). ~~CM~~The Lt deposits comprise both blocky ash (e.g. Fig 9B) and micro-vesiculated cuspate ash (e.g. Fig 9D and F) suggesting that both phreatomagmatic (external water) and magmatic (internal volatiles) drove the explosive fragmentation processes. We note that blocky juveniles are dominant in Lt_{1-3} suggesting that phreatomagmatic reactions involving glacial meltwater played the largest role in the explosive eruptive style.

Based on the overall bedform and textures found in Lt deposits, we assert that the depositional environment was wet and probably (shallow) subaqueous. The massive~~,~~ character and moderate to poor sorting of Lt_1 suggest ~~an influx of fragmental material erupted through~~continuous deposition from a sustained column, rather than periodic explosive pulses which would generate moderately sorted and bedded deposits via elutriation (e.g., White, 1996, 2000) ~~and the~~. The lack of welding ~~between matrix and juvenile material suggests~~, compaction, or clast imbrication is also consistent with a water-rich intergranular phase (rather than gas) ~~was present through~~for these ~~eruption-fed aqueous~~pyroclastic density currents (White, 2000; Brand and Clarke, 2009).

The thinly bedded, moderate to well sorted, and weakly normally graded Lt_2 is indicative of deposition from dilute pyroclastic density currents (i.e. pyroclastic surge; Fisher and Waters, 1970; Brand and Clarke, 2009). These deposits reflect phreatomagmatic explosive pulses that dispersed highly fragmented ash laterally and elutriated through the water column. The shallow dipping cross-bedding preserved in some Lt_2 outcrops (Fig. 4B) is consistent with subaqueous pyroclastic deposits (Moorhouse and White, 2016). The overall lack of well-sorted beds of fine

ash, characteristic of thick water column elutriation, makes a shallow subaqueous setting most plausible.

~~Lt_3 is composed~~Lt_3 contains moderate volumes (20-40 %) of non-welded spatter within moderately to well-sorted ash and lapilli matrix (Fig. 4C). We propose that the Lt_3 deposits record periods of increased magma flux, volatility, and/or a decreased water supply (at the vent), where a strombolian style burst ejected largely vesiculated and fluidal clasts (Latutrie and Ross, 2020). We find that the overall characteristics of the Lt_3 deposits indicate a shallow aqueous to emergent depositional environment. This assertion is based on a lack of bomb sags within these deposits and chilled but not quenched (or pillowed) spatter clasts. The two outcrops of Lt_3 are located at upper elevations of CM, and not observed within lower to middle stratigraphy. Our interpretation is Lt_3 represents localized magmatic generated fallout mixed with phreatomagmatically generated pyroclastic density currents in shallow aqueous to locally drained regions of CM.

Explosively derived Lt deposits are present at all elevations of CM (Fig. 2) and ~~we estimate that it comprises~~comprise ~30% of the entire edifice ~~by volume~~ (Table 1~~).~~), and excluding intrusions, are closer to 60% of the volcano volume. Our findings indicate that not only was the onset of the CM eruptions explosive but that explosivity was sustained ~~through the middle to late stages~~throughout most of the eruption. This explosive-styled eruption makes CM unique within the GVB, being only one of five other identified tephra-dominated glaciovolcanic landforms (Wilson and Russell, 2018). We ~~hypothesise~~speculate that ~~these~~ explosive ~~styled~~ onsets to glaciovolcanic eruptions may ~~not~~ be ~~uncommon in any glaciovolcanic setting but rather~~significantly more common than recognized and underestimated because tephra-dominated landforms are ~~less likely to be preserved, compared~~highly susceptible to ~~lava-dominated tuyas, if multiple cycles of glaciation occur after edifice formation~~erosion. We suggest CM's transitional eruptive history, which produced intrusive and effusive coherent lavas, helped create a stronger structure more resistant to glacial erosion.

~~8.3 Model for CM eruption~~

~~The glaciovolcanic deposits record a complex sequence of events indicative of a primarily subaqueous setting. We find that the interior of the edifice is dominated by tephra and peperitic intrusions, while the margins are comprised of coherent lavas and lava-dominated~~

~~breccias. These variable lithofacies speak to transitions in eruptive style from explosive to effusive. Lastly, the shape and present-day partial collapse of CM (in the form of cracks) provide a post-eruptive context for the paleoenvironmental setting of the eruption. Our model for the CM sequence of events (Fig. 12) is described below.~~

The investigation of Cracked Mountain deposits records a complex sequence of events beyond the initially explosive onset. Our analysis suggests the following conceptual model for the evolution of the CM eruption (Fig. 12):

1. An explosive, Surtseyan phase dominated the initial CM eruption, producing a subaqueous tephra cone ~~comprised of~~comprising Lt_1 (Fig. 12A). ~~This~~ Our interpretation of this initial phase is ~~evidenced by the predominant bedform structure and componentry of Lt_1 (i.e. massive, moderately sorted vitric ash and lapilli) which we interpret to be derived from a sustained phreatomagmatic column and proximal high-density pyroclastic flows. Our temporal assessment for this phase is based on stratigraphic relations~~ detailed above.

~~1. (i.e. Association A; Fig. 5) between Lt_1 and Lpi. This association is seen from the base of the edifice (e.g. Fig 2B) through to the summit and is supported by the fact that we find no exposure where CM volcanics post-date Lt_1, making it the oldest mapped unit.~~

2. ~~The second CM eruptive phase is characterized by the~~ transition from explosive to effusive (and intrusive) activity (Fig. 12B~~). Peperitic~~) is expressed by peperitic dykes (Ld_1) and bodies (Lpi~~)~~). These intrusions inflate the edifice ~~from within,~~endogenously and dykes that ~~reach~~pierce the margins of the tephra pile form stacks of pillow lavas (Lp) ~~that pile up on~~ at the margins of the volcano. ~~The presence of peperites (Pi) along the margins of Lpi (Fig. 6) indicates that these large lava bodies were intrusive rather than extrusive. This relationship shows that phase 2 occurred rapidly after phase 1, where the previously erupted tephra was still unlithified.~~

3. ~~The third CM eruptive phase involved continued intrusions and effusions through the earlier erupted lithofacies, forming effusive lavas (Ls), breccias (Tb), and dykes (Ld_2) (Fig. 12C). The columnar jointing of the remnant Ls outcrops suggests the lake level was draining periodically at this point, likely through well-established drainage channels that prevented lake volumes from reaching amounts capable of floating the encapsulating glacier (see section 8.4 below). The massive tuff breccias contain lithics from all other volcanic lithofacies, including rounded, block-sized Lt_1. This relationship suggests explosivity~~

~~persisted throughout the later stages of the CM eruption, where underlying Lt_1 was ripped up, subrounded, entrained, and deposited in Tb. The later stage explosivity is further substantiated by our findings of high stratigraphy fire-fountaining deposits (Lt_3) that show signs of 'dryer' deposition in locally drained regions of the edifice.~~Late-stage intrusions and effusions produce effusive lavas (Ls) and dykes (Ld_2) and associated breccias (Tb), (Fig. 12C). The culmination of the CM eruption is marked by late-stage dyke activity (Ld_2) that cut through all other lithofacies. ~~Despite changes in eruptive styles (i.e. explosive and effusive) and environments (i.e. wet and dry), the~~The paleomagnetic signatures of all CM deposits overlap within one paleomagnetic moment. Thus, the CM eruption taking place from stages 1-3 can be thought of as more or less continuous.

The final stage (4) in the CM formation was non-eruptive and characterized by glacial erosion and edifice collapse (Fig. 12D). The timing of glacial retreat ~~after the CM eruption~~ is unclear, but ~~we do find evidence of glaciation (i.e.~~ the present-day surface features bedrock erratics and scour marks~~) on the present-day surface. These findings show that at some point post-eruption, CM was once again enveloped in an ice sheet. We propose that this~~ indicating post-eruptive glaciation ~~removed portions of the upper CM eruptive stratigraphy~~. The widespread distribution of large extensional fissures and ~~carved the over-steepened edifice margins that we presently see today. The final process we model at CM is the formation of the~~ cracks ~~after the glacial unconfinement. We attribute this partial edifice collapse to the removal of confining pressure after the ice sheet retreated. The lack of glacial deposits~~results from the retreat of the enclosing ice sheet which originally buttressed the steep-walled edifice. Glacial erratics are not found within ~~the cracks indicates that they formed after the localized last glacial maximum and are probably continuing to collapse to the present day.~~these fissures which may suggest that the edifice was mainly enclosed (and buttressed) by regional and local ice until the Last Glacial Period (i.e. <115 -120 ka).

8.42 Paleoenvironmental ~~reconstruction~~ implications

~~We find englacial erupted~~ Our mapping and analysis suggest CM is a monogenetic edifice with no evidence for significant time gaps during the eruption. The results of paleomagnetic

analyses concur with our field observations that the varying lithofacies ~~at elevations up to~~were emplaced in one paleomagnetic moment (≲ 1,000 years; Turner, 1987; Barletta et al., 2010; Lisé-Pronovost et al., 2013) at 401 ± 38 ka (Fig. B1).

The CM lithofacies (i.e. pillow lavas, palagonitized tuffs, and peperites) indicate a subaqueous eruptive paleoenvironment, however, the edifice is situated at a high elevation in a high relief environment and surrounded by steep-sided deep (~800 m) valleys (Fig. 3). ~~650 m a.s.l, with the volcanic succession built ~250 m atop the basement rocks. These findings require~~We suggest a glaciovolcanic eruption into a sustained englacial lake of meltwater enclosed by a substantial ice sheet on the basis that there are no obvious physical barriers (i.e. mountains or ridges) to allow for a conventional paleo-lake. The volcanic lithofacies suggest that the englacial lake was sustained throughout the eruption and that the lake surface elevation continued to rise with the growth of the edifice. The CM volcano is best described as a transitional, tephra-dominated, tuya after the descriptive classification of Russell et al., (2014) and its lithofacies associations make it distinct from the classical mafic tuya model (e.g., pillow effusion, hyaloclastites, lava-fed deltas, and capping lava) (Smellie, 2007; Jakobsson and Gudmundsson, 2008; Edwards et al., 2015).~~which CM erupted into~~

The CM volcanic succession is ~250 m thick and rests on basement rocks at ~1,250 m a.s.l (Fig. 2A). Subaqueous lithofacies outcrop at elevations as high as ~1,650 m a.s.l where they have relief of ~800 m above the major drainages. At the highest elevations of CM (~1,600-1650 m a.s.l), we find small remnant subaerial sheet lavas (Ls) although the abundance of Ls lithics within the thick succession of Tb deposits may suggest that there was much more subaerial lava originally. There are, at least, two scenarios that would ~~have been ~250 m deep along the edifice margins~~explain subaerial capping lavas within the englacial lake environment. The most likely scenarios are that, either, i) the edifice grew and became emergent above the paleolake level to form a classic passage zone defining a maximum lake level (Jones, 1970; Smellie, 2006; Russell et al., 2013; Edwards et al., 2015) or ii) the level of the englacial lake decreased due to subglacial drainage creating a "dry" subaerial environment. In the latter case, post-draining subaerial lavas overlapping the subaqueous lithofacies establish a minimum level of the englacial lake (Smellie, 2006; Skilling, 2009; Russell et al., 2013).

There is no direct evidence for a passage zone relationship (i.e. beds of pillow lava breccias or lava fed deltas) so we favour the second scenario involving overlap lavas wherein the elevation of Ls at ~1,650 m defines a minimum level and, thus, a minimum depth of ~250 m for the paleo-englacial lake (Fig 13B). We ~~use these findings to investigate the minimum~~have used the shape and size of the CM edifice and the surrounding topography to constrain the maximum dimensions and volume of the paleo-englacial lake. The paleo-topography beneath the CM edifice (Figs. 3, 13A) limits the size of the syn-eruptive englacial lake. Relative to the present-day edifice we estimate the lake may have extended <100 m to the south and <300 m to the east but been limited to < 50 m to the north and west by very steep drainages. Assuming an asymmetric shape of 1,800 m long and 1,300 m wide and a maximum depth of 250 m (Fig. 13B) yields a maximum lake volume at ~0.36 km^3. The present-day (i.e. minimum) volume of the CM volcano is ~0.18 km^3 such that the lake could only store < 0.18 km^3 of water (i.e. maximum lake volume – edifice volume). This strongly suggests that throughout the eruption the englacial lake was never fully sealed but was a leaky system where meltwater production and sub-ice drainage were nearly matched (cf. Russell et al. 2014). As the eruption waned, melting of the enclosing ice became less efficient and drainage became dominant, leading to a lowering of the lake level to allow for subaerial eruption of lavas (Fig. 12C).

To sustain a lake level of 250 m requires a rate of leakage less than the rate of meltwater accumulation and also requires an ice thickness ~~at the time of the CM eruption. In glacial lakes, when the water level exceeds ~90% of ice thickness,~~above ~280-300 m to counterbalance the hydrostatic ~~pressures exceed glaciostatic pressures, causing the ice to float~~lake pressure (e.g., Tweed and Russell, 1999; Smellie, 2006; Edwards et al., 2015). The surrounding topography features steep drainages with valley floors at ~ 800 m a.s.l. (i.e. ~~In the case of CM, we find that to sustain a lake level of 250 m without resulting in hydrostatic drainage, the ice must have been at least ~280 m above the basement rocks. We find no field-based evidence of rapid subaerial edifice growth that would indicate a deluge of meltwater occurred (i.e. jökulhlaups; Tweed and Russell, 1999; Gudmundsson et al., 2004; Russell et al., 2013). Therefore, the minimum ice cover must have reached 1,680 m a.s.l. Given that CM is not located beneath peaks that could have sourced an alpine glacier, the encompassing ice must have been a continental ice sheet (CIS). We use the models of CIS growth and decay (e.g.,~~Meager Creek and Elaho valley; Figs. 3 and 13). This suggests that the enclosing ice sheet, an earlier (paleo-) incarnation of the

Cordilleran Ice Sheet (CIS) at 401 ± 38 ka, was at least 880 m thick. This minimum ice thickness has implications for the distribution of the paleo-CIS and suggests that most of the surrounding landscape was under ice except at the highest elevations (Fig. 13A and C; Clague, 2009; Wilson et al., 2020) ~~to show that the surrounding Meager Creek and Elaho Valley's would have been filled with ice, and only the upper elevation peaks of the Mount Meager massif would be emergent (Fig. 13A). We use the constraints of the surrounding topography to calculate the minimum thickness of the CIS. The lowest point in the northward Meager Creek valley is ~800 m a.s.l, thus the CIS was > 880 m thick (given the elevation of ice above CM at 1,680 m a.s.l) (Fig. 13C). .~~

~~We use the shape and size of CM and the surrounding topography to approximate the maximum dimensions and volume of a paleo-englacial lake. Based on the gradient of underlying basement rocks (Fig. 3), we estimate that the englacial lake is unlikely to have extended more than 50 m past the north and west CM borders, ~100 m from the south edge, and up to 300 m at the east edifice corner (Fig. 13A). We estimate that the lake had an asymmetric shape, 1800 m long and 1300 m wide, and a maximum depth of 250 m (Fig. 13B). From our estimated dimensions, and assumed uniform lake depth, we calculate maximum lake volume at ~0.36 km^3. We estimate the volume of erupted material to be ~0.18 km^3 based on present-day edifice dimensions and thickness. Throughout the eruption, water volume (within the lake) would have been displaced by erupting material, and by stage three (i.e. edifice maximum volume), only ~0.18 km^3 (i.e. max lake volume – edifice volume) of water could have been stored in the lake. The heat capacity of a basaltic eruption the size of CM is capable of melting more than 2 km^3 of water from surrounding ice (e.g., Gudmundsson et al., 2004; Kelman, 2005; Tuffen, 2007). This volume of meltwater exceeds the capacity of our proposed maximum paleolake and negates the possibility of a fully sealed lake catchment system. Instead, we propose a leaky lake system, with established drainage channels (Fig 13).~~

The CM age of 401 ± 38 ka ~~fits within~~coincides with the waning of marine $\delta^{18}O$ isotope stage (MIS) 12 glacial period (~470-425 ka) ~~into~~and the warming period of MIS 11 (~420-375 ka) (Lisiecki and Raymo, 2005) (Fig. 14). The shift in global $\delta^{18}O$ ~~during~~ associated with the MIS 12 to 11 transition is the ~~most drastic~~largest of all the Pleistocene cycles ~~(e.g. Fig 14), signifying~~and signifies rapid global warming~~. Thus, we believe a CIS~~ (e.g. Fig 14; Lisiecki and Raymo, 2005). The ~850 m (or thicker) thickness of ~~~850 m at 400 ka (i.e. middle~~the paleo-CIS

enclosing the Cracked Mountain volcano is inconsistent with the mid-point of MIS 11~~) was unlikely. Instead, we favour~~ at 400 ka. However, if we accept a slightly older $^{40}Ar/^{39}Ar$ age of ~425 ka ~~for the Cracked Mountain eruption. This slightly older age fits~~(still within the analytical uncertainty ~~of the $^{40}Ar/^{39}Ar$ results and places~~) (Table B1) for the eruption ~~more within the waning of~~of Cracked Mountain, the age accords well with the global ice period ~~(~~MIS 12~~)~~ (Lisiecki and Raymo, 2005; Batchelor et al., 2019). Eruption ages for other volcanoes in the GVB are sparse, however, Wilson and Russell (2018) report glaciovolcanic eruptions during MIS 12 within the Mount Cayley volcanic field (Ember Ridge, unpublished age), as well as, subaerial lavas erupting in the Salal glacier field during MIS 11 (Nichols Valley at 405 ka). These additional age constraints, although limited, do support the eruption of Cracked Mountain into an early (late-Pleistocene) incarnation of the CIS within SW British Columbia at ~ 425 ka.

~~-~~We also speculate that at this time, there may have been a large-scale decompression effect on the Earth's crust driven by rapid deglaciation at the end of MIS 12. The link between volcanism and crustal unloading during periods of deglaciation has been modeled throughout the GVB (e.g., Wilson and Russell, 2020) and explored in Icelandic and Andean glaciovolcanic fields (e.g., Carrivick et al., 2009; Guillot and Ponce, 2021). We, therefore, find it entirely feasible that the CIS retreat in SW British Columbia would have triggered magmatic ascent through the unloaded crust, leading to the ~~CM eruption.~~eruption of the Cracked Mountain volcano (as well as others). Lastly, since records of older glaciation cycles tend to be obscured by younger waxing and waning of ice sheets, our findings at CM provide useful temporal and physical constraints for the CIS extent in SW British Columbia during the mid-Pleistocene.

9. Summary

The Garibaldi Volcanic Belt contains many Quaternary glaciovolcanic centres. The study of these volcanoes provides paleoclimatic evidence at the time of the eruptions and contributes to the understanding of magma, ice, and water interactions more generally. Here, we present the first physical volcanological study of Cracked Mountain, a transitional, tephra-dominated tuya. Our findings indicate an initially explosive eruption that later transitioned into ~~a mixture of~~ intrusive and ~~extrusive styles~~effusive activity. We characterize the explosivity as dominantly phreatomagmatic, manifested as Surtseyan style eruption in a shallow englacial lake. Peperitic intrusions and pillow lava effusions are the largest coherent units by volume, indicating that

subaqueous conditions persisted through the middle and later stages of the eruption. Small remnants of subaerially erupted lavas are preserved at the highest elevations, suggesting that the lake drained periodically in the later stages of the eruption. This claim is supported by our modeling of paleolake dimensions and volumetric capacities. Lastly, our temporal investigation of the eruption concludes that CM was monogenetic, erupting ~425 ka between MIS 11 and 12. We model the localized, mid-Pleistocene CIS as having a minimum thickness of ~850 m, reaching elevations of 1,680 m a.s.l or higher.

Acknowledgments

This research was supported by the ~~National Resources~~Geological Survey of Canada ~~(NRCan) Research Affiliate~~with funding through NRCan's Emerging Renewable Power Program ~~for the Geothermal Energy Project, Mount Meager~~and GeoScience BC. Special thanks to Steve Grasby of NRCan for all his help organizing field campaigns and funding analytical methods. We thank Sophie Leiter, Lindsey Abdale, Annie Borch, and Mahmud Mohammad for their assistance in the field.

References

Barletta, F., St-onge, G., Channell, J.E.T., and Rochon, A., 2010, Dating of Holocene western Canadian Arctic sediments by matching paleomagnetic secular variation to a geomagnetic field model: Quaternary Science Reviews, v. 29, p. 2315–2324, doi:10.1016/j.quascirev.2010.05.035.

Le Bas, M.J., Le Maitre, R.W., Streckeisen, A., and Zanettin, B., 1986, A chemical classification of volcanic rocks based on the total alkali-silica diagram: Journal of Petrology, v. 27, p. 745–750, doi:10.1093/petrology/27.3.745.

Batchelor, C.L., Margold, M., Krapp, M., Murton, D.K., Dalton, A.S., Gibbard, P.L., Stokes, C.R., Murton, J.B., and Manica, A., 2019, The configuration of Northern Hemisphere ice sheets through the Quaternary: Nature Communications, v. 10, doi:10.1038/s41467-019-11601-2.

Brand, B.D., and Clarke, A.B., 2009, The architecture, eruptive history, and evolution of the Table Rock Complex, Oregon: From a Surtseyan to an energetic maar eruption: Journal of

Volcanology and Geothermal Research, v. 180, p. 203–224, doi:10.1016/j.jvolgeores.2008.10.011.

Carrivick, J.L., Russell, A.J., Rushmer, E.L., Tweed, F.S., Marren, P.M., Deeming, H., and Lowe, O.J., 2009, Geomorphological evidence towards a de-glacial control on volcanism: Earth Surface Processes and Landforms, v. 1178, p. 1164–1178, doi:10.1002/esp.

Chadima and Hrouda, 2006, Remasoft 3.0: A user-friendly paleomagnetic data browser and analyzer: Travaux Géophysiques, v. XXVII, p. 20–21.

Clague, J.J., 2009, Cordilleran Ice Sheet: Encyclopedia of Paleoclimatology and Ancient Environments, p. 206–211.

Clague, J.J., and Ward, B., 2011, Pleistocene Glaciation of British Columbia: Elsevier Inc., v. 15, 563–573 p., doi:10.1016/B978-0-444-53447-7.00044-1.

Clay, P.L., Busemann, H., Sherlock, S.C., Barry, T.L., Kelley, S.P., and McGarvie, D.W., 2015, 40Ar/39Ar ages and residual volatile contents in degassed subaerial and subglacial glassy volcanic rocks from Iceland: Chemical Geology, v. 403, p. 99–110, doi:10.1016/j.chemgeo.2015.02.041.

Doyle, M.G., 2000, Clast shape and textural associations in peperite as a guide to hydromagmatic interactions: Upper Permian basaltic and basaltic andesite examples from Kiama, Australia: Australian Journal of Earth Sciences, v. 47, p. 167–177, doi:10.1046/j.1440-0952.2000.00773.x.

Edwards, B.R., Gudmundsson, M.T., and Russell, J.K., 2015, Glaciovolcanism: The Encyclopedia of Volcanoes, p. 377–393, doi:10.1016/b978-0-12-385938-9.00020-1.

Edwards, B.R., Skilling, I.P., and Tuffen, H., 2009, Volcano-Ice Interactions on Earth and Mars: Journal of Volcanology and Geothermal Research, v. 185, p. 247–250.

Fisher, R. V, and Waters, A.C., 1970, Base surge ~~bedforms~~bed forms in Maar volcanoes: American Journal of Science, v. 268, p. 157–180.

Green, N.L., Harakal, J.E., Souther, I.J.G., and Read, P.B., 1988, Eruptive history and K-Ar geochronology of the late Cenozoic Garibaldi volcanic belt, southwestern British Columbia: Geological Society of America Bulletin, v. 100, p. 563–579, https://pubs.geoscienceworld.org/gsa/gsabulletin/article-pdf/100/4/563/3380343/i0016-7606-100-4-563.pdf.

Green, N.L., and Harry, D.L., 1999, On the relationship between subducted slab age and arc

basalt petrogenesis, Cascadia subduction system, North America: Earth and Planetary Science Letters, v. 171, p. 367–381, doi:10.1016/S0012-821X(99)00159-4.

Green, N.L., and Sinha, A.K., 2004, Consequences of varied slab age and thermal structure on enrichment processes in the sub-arc mantle of the northern Cascadia subduction system: Journal of volcanology and geothermal research, v. 140, p. 107–132.

Gudmundsson, M.T., Sigmundsson, F., Bjornsson, H., and Hognadottir, T., 2004, The 1996 eruption at Gjálp, Vatnajökull ice cap, Iceland : efficiency of heat transfer, ice deformation, and subglacial water pressure: Bulletin of Volcanology, v. 66, p. 46–65, doi:10.1007/s00445-003-0295-9.

Guillot, M.G., and Ponce, J.F., 2021, Change of eruptive style during Pliocene deglaciation : from scoria cones to lava shields in southern extra - Andean Patagonia , Argentina: Bulletin of Volcanology, p. 1–19, doi:10.1007/s00445-021-01466-z.

Harris, M., and Russell, J.K., 2021, Bedrock Mapping Results for the Mount Meager Geothermal Research Initiative: Geoscience BC, p. 7–34.

Hickson, C.J., Russell, J.K., Stasiuk, M. V, and Swanson, D.A., 1999, Volcanology of the 2350 B.P. Eruption of Mount Meager Volcanic Complex, British Columbia, Canada: implications for Hazards from Eruptions in Topographically Complex Terrain 1: Bulletin of Volcanology, v. 60, p. 489–507.

Hildreth, W., 2007, Quaternary Magmatism in the Cascades-Geologic Perspectives: U.S Geological Survey, v. 1744, p. 1–123.

Hooten, J.A., and Ort, M.H., 2002, Peperite as a record of early-stage phreatomagmatic fragmentation processes: An example from the Hopi Buttes volcanic field, Navajo Nation, Arizona, USA: Journal of Volcanology and Geothermal Research, v. 114, p. 95–106, doi:10.1016/S0377-0273(01)00282-7.

Irvine, T.N., and Baragar, W.R.A., 1971, A Guide to the Chemical Classification of the Common Volcanic Rocks: Canadian Journal of Earth Sciences, v. 8, p. 523–548, doi:10.1139/e71-055.

Jakobsson, S., and Gudmundsson, M., 2008, Subglacial and intraglacial volcanic formations in Iceland: Jökull, v. 58, p. 179–196.

Jicha, B.R., Singer, B.S., and Sobol, P., 2016, Re-evaluation of the ages of 40Ar/39Ar sanidine standards and supereruptions in the western U.S. using a Noblesse multi-collector mass

spectrometer: Chemical Geology, v. 431, p. 54–66, doi:10.1016/j.chemgeo.2016.03.024.

Johnson, C.L. et al., 2008, Recent investigations of the 0-5 Ma geomagnetic field recorded by lava flows: Geochemistry, Geophysics, Geosystems, v. 9, doi:10.1029/2007GC001696.

Jones, T.G., 1970, Intraglacial Volcanoes of the Laurgarvatn Region, Southwest Iceland, II: Journal of Geology, v. 78, p. 127–140.

Kelman, M.C., 2005, Glaciovolcanism at the Mount Cayley Volcanic Field, Garibaldi Volcanic Belt, Southwestern British Columbia: University of British Columbia, 1–258 p.

Kelman, M.C., Russell, J.K., and Hickson, C.J., 2002, Effusive intermediate glaciovolcanism in the Garibaldi Volcanic Belt, southwestern British Columbia, Canada: Geological Society, London, Special Publications, v. 202, p. 195–211, doi:10.1144/GSL.SP.2002.202.01.10.

Kirschvink, J.L., 1980, The least- squares line and plane and the analysis of palaeomagnetic data: Geophysical Journal of the Royal Astronomical Society, v. 62, p. 699–718, doi:10.1111/j.1365-246X.1980.tb02601.x.

Latutrie, B., and Ross, P.S., 2020, Phreatomagmatic vs magmatic eruptive styles in maar-diatremes: a case study at Twin Peaks, Hopi Buttes volcanic field, Navajo Nation, Arizona: Bulletin of Volcanology, v. 82, doi:10.1007/s00445-020-1365-y.

Lawrence, R.B., Armstrong, R.L., and Berman, R.G., 1984, Garibaldi Group Volcanic Rocks of the Salal Creek Area, Southwestern British Columbia: Alkaline Lavas on the Fringe of the Predominantly Calc-Alkaline Garibaldi (Cascade) Volcanic Arc: Journal of Volcanology and Geothermal Research, v. 21, p. 255–276.

Lescinsky, D.T., and Fink, J.H., 2000, Lava and ice interaction at stratovolcanoes: Use of characteristic features to determine past glacial extents and future volcanic hazards: Journal of Geophysical Research: Solid Earth, v. 105, p. 23711–23726, doi:10.1029/2000jb900214.

Lisé-Pronovost, A., St-onge, G., Gogorza, C., Haberzettl, T., Preda, M., Kliem, P., Francus, P., Zolitschka, B., Pasado, T., and Team, S., 2013, High-resolution paleomagnetic secular variations and relative paleointensity since the Late Pleistocene in southern South America: Quaternary Science Review, v. 71, p. 91–108, doi:10.1016/j.quascirev.2012.05.012.

Lisiecki, L.E., and Raymo, M.E., 2005, A Pliocene-Pleistocene stack of 57 globally distributed benthic D 18 O records: Paleoceanography, v. 20, p. 1–17, doi:10.1029/2004PA001071.

Martin, U., and Németh, K., 2007, Blocky versus fluidal peperite textures developed in volcanic conduits, vents and crater lakes of phreatomagmatic volcanoes in Mio/Pliocene volcanic

fields of Western Hungary: Journal of Volcanology and Geothermal Research, v. 159, p. 164–178, doi:10.1016/j.jvolgeores.2006.06.010.

Mathews, W.H., 1952, Mount Garibaldi, A Supraglacial Pleistocene Volcano in Southwestern British Columbia: American Journal of Science, v. 250, p. 81–103.

Min, K., Mundil, R., Renne, P.R., and Ludwig, K.R., 2000, A test for systematic errors in 40Ar/39Ar geochronology through comparison with U/Pb analysis of a 1.1-Ga rhyolite: Geochimica et Cosmochimica Acta, v. 64, p. 73–98, doi:10.1016/S0016-7037(99)00204-5.

Moorhouse, B.L., and White, J.D.L., 2016, Interpreting ambiguous bedforms to distinguish subaerial base surge from subaqueous density current deposits: The Depositional Record, v. 2, p. 173–195, doi:10.1002/dep2.20.

Mullen, E.K., and Weis, D., 2013, Sr-Nd-Hf-Pb isotope and trace element evidence for the origin of alkalic basalts in the Garibaldi Belt, northern Cascade arc: Geochemistry, Geophysics, Geosystems, v. 14, p. 3126–3155, doi:10.1002/ggge.20191.

Read, P.B., 1979, Meager Creek Geothermal Area: , p. 1 Sheet, doi:10.4095/129507.

Read, P., 1990, Mt Meager Complex, Garibaldi Belt, Southwestern BC.: Geoscience Canada, v. 17, p. 167–170.

Roddick, J.C., and Souther, J.G., 1987, Geochronology of Neogene volcanic rocks in the northern Garibaldi Belt, British Columbia: Geological Survey of Canada, v. 87–2, p. 21–24.

Rosa, C.J.P., Mcphie, J., and Relvas, J.M.R.S., 2016, Distinguishing peperite from other sediment-matrix igneous breccias : Lessons from the Iberian Pyrite Belt: Journal of Volcanology and Geothermal Research, v. 315, p. 28–39, doi:10.1016/j.jvolgeores.2016.02.007.

Russell, J.K., Edwards, B.R., and Porritt, L.A., 2013, Pyroclastic passage zones in glaciovolcanic sequences: Nature Communications, v. 4, doi:10.1038/ncomms2829.

Schiffman, P., Watters, R.J., Thompson, N., and Walton, A.W., 2006, Hyaloclastites and the slope stability of Hawaiian volcanoes: Insights from the Hawaiian Scientific Drilling Project's 3-km drill core: Journal of Volcanology and Geothermal Research, v. 151, p. 217–228, doi:10.1016/j.jvolgeores.2005.07.030.

Skilling, I.P., 2009, Subglacial to emergent basaltic volcanism at Hlöðufell, south-west Iceland: A history of ice-confinement: Journal of Volcanology and Geothermal Research, v. 185, p. 276–289, doi:10.1016/j.jvolgeores.2009.05.023.

Skilling, I.P., White, J.D.L., and Mcphie, J., 2002, Peperite : a review of magma-sediment mingling: Journal of Volcanology and Geothermal Research, v. 114, p. 1–17.

Smellie, J.L., 2007, Glacial landforms | Quaternary vulcanism, subglacial landforms: Encyclopedia of Quaternary Science, p. 784–798, doi:10.1016/B0-44-452747-8/00101-0.

Smellie, J.L., 2006, The relative importance of supraglacial versus subglacial meltwater escape in basaltic subglacial tuya eruptions: An important unresolved conundrum: Earth-Science Reviews, v. 74, p. 241–268, doi:10.1016/j.earscirev.2005.09.004.

Stewart, M.L., Russell, J.K., and Hickson, C.J., 2008, Geology, Pebble Creek formation, British Columbia: , p. 1 sheet.

Stroncik, N.A., and Schmincke, H.U., 2002, Palagonite - A review: International Journal of Earth Sciences, v. 91, p. 680–697, doi:10.1007/s00531-001-0238-7.

Sun, S.S., and McDonough, W.F., 1989, Chemical and isotopic systematics of oceanic basalts: Implications for mantle composition and processes: Geological Society Special Publication, v. 42, p. 313–345, doi:10.1144/GSL.SP.1989.042.01.19.

~~Taylor, J.R., 1982, An Introduction to Error Analysis-The Study of Uncertainties in Physical Measurements: 1–327 p.~~

~~Tuffen, H., 2007, Models of ice melting and edifice growth at the onset of subglacial basaltic eruptions: Journal of Geophysical Research, v. 112, p. 1–14, doi:10.1029/2006JB004523.~~

Turner, G.M., 1987, A 5000 year geomagnetic palaeosecular variation record from western Canada: Geophysical Journal of the Royal Astronomical Society, p. 103–121.

Tweed, F.S., and Russell, A.J., 1999, Controls on the formation and sudden drainage of glacier-impounded lakes: Implications for jökulhlaup characteristics: Progress in Physical Geography, v. 23, p. 79–110, doi:10.1191/030913399666727306.

White, J.D.L., 1996, Pre-emergent construction of a lacustrine basaltic volcano, Pahvant Butte, Utah (USA): Bulletin of Volcanology, v. 58, p. 249–262, doi:10.1007/s004450050138.

White, J.D.L., 2000, Subaqueous eruption-fed density currents and their deposits: Precambrian Research, v. 101, p. 87–109, doi:10.1016/S0301-9268(99)00096-0.

White, J.D.L., and Houghton, B.F., 2006, Primary volcaniclastic rocks: Geology, v. 34, p. 677–680, doi:10.1130/G22346.1.

White, J.D.L., Mcphie, J., and Skilling, I., 2000, Peperite: A useful genetic term: Bulletin of Volcanology, v. 62, p. 65–66, doi:10.1007/s004450050293.

White, J.D.L., and Valentine, G.A., 2016, Magmatic versus phreatomagmatic fragmentation: Absence of evidence is not evidence of absence: Geosphere, v. 12, p. 1478–1488, doi:10.1130/GES01337.1.

Wilson, A.M., and Russell, J.K., 2020, Glacial pumping of a magma-charged lithosphere : A model for glaciovolcanic causality in magmatic arcs: Earth and Planetary Science Letters, v. 548, p. 116500, doi:10.1016/j.epsl.2020.116500.

Wilson, A.M., and Russell, J.K., 2017, Lillooet Glacier basalts, southwestern British Columbia, Canada: Products of Quaternary Glaciovolcanism: Canadian Journal of Earth Sciences, v. 54, p. 639–653, doi:10.1139/cjes-2016-0201.

Wilson, A.M., and Russell, J.K., 2018, Quaternary glaciovolcanism in the Canadian Cascade volcanic arc—Paleoenvironmental implications: Field Volcanology: A Tribute to the Distinguished Career of Don Swanson. Geological Society of America, v. 538, doi:10.1130/2018.2538(06).

Wilson, A.M., Russell, J.K., and Quane, S.L., 2019, The table, a flat-topped volcano in southern British Columbia: Revisited: American Journal of Science, v. 319, p. 44–73, doi:10.2475/01.2019.02.

Wilson, A.M., Russell, J.K., and Ward, B.C., 2020, Paleo-glacier reconstruction in southwestern British Columbia, Canada : A glaciovolcanic model: Quaternary Science Reviews, v. 218, p. 178–188, doi:10.1016/j.quascirev.2019.06.024.

Woodsworth, G., 1977, Geology of Pemberton (92J) Map Area: Geological Survey of Canada, p. 1 sheet.

Zimanowski, B., Fröhlich, G., and Lorenz, V., 1991, Quantitative experiments on phreatomagmatic explosions: Journal of Volcanology and Geothermal Research, v. 48, p. 341–358, doi:10.1016/0377-0273(91)90050-A.

Figure Captions

Figure 1: Location and geologic setting of Cracked Mountain volcano. A) Map of the Cascade volcanic arc in the USA and Canada (i.e. Garibaldi volcanic belt (GVB)) (modified from Mullen and Weis, 2013; Wilson and Russell, 2017). B) Undivided geological map of MMVC distribution of Mt. Meager volcanic deposits (MV), basement (Bu) throughout the region (Woodsworth, 1977; Read, 1979; Harris and Russell, 2021). The youngest MMVC eruption, 2350 B.P. Pebble Creek Formation (PcF) (Hickson et al., 1999; Stewart et al., 2008) is differentiated from other MMVC volcanics. Cracked Mountain (CM) is situated south of the

main MMVC (Wilson and Russell, 2018; Harris and Russell, 2021). Map projection based on Universal Transverse Mercator, Zone 10U North American Datum 1983.

Figure 2: Geology of Cracked Mountain. A) Geologic map showing the distribution of CM volcanic lithofacies. Dyke location and orientations are shown in red; extensional cracks are shown in black. The volcanic edifice unconformably overlies basement granodiorites (Bg) and mica-schists (Bs). ~~Black~~White-numbered dots show locations of representative stratigraphic logs (B, C). B) Graphic logs showing volcanic stratigraphy at various locations and elevations ~~(black numbered dot)~~ within the map area (depicted in Figs. 2A). Lithologies are depicted with various patterns and symbols while corresponding map units are shown in the same colours as Fig. 2A. Red lines shown in map units represent intruding dykes observed within the lithologies of the graphic logs. Map projection based on Universal Transverse Mercator, Zone 10U North American Datum 1983.

Figure 3: Physiographic setting of Cracked Mountain volcano. A) NE-SW oriented Google Earth imagery of Cracked Mountain showing the location of volcanic deposits overlying basement rocks (white-arrows). ~~Visible~~B) N-S oriented Google Earth imagery of Cracked Mountain (outlined in white), highlighting visible cracks parallel the steep drainages. ~~B~~C) South-West facing DEM hillshade map showing CM volcanics (red shaded outline) situated above present-day Meager Creek and Elaho Valleys.

Figure 4: Field photos displaying bedform structures of CM lapilli tuffs: A) Field photo showing ~2 m thick exposure of massive, moderately sorted ash and lapilli tuff underlying poorly sorted tuff breccia (Tb). Half metre hammer (~~outlined in~~ white arrow) for scale. B) Field photo displaying a ~0.5m thick exposure of thinly bedded, well-sorted, ash, and a lapilli tuff (Lt_2) interbedded within massive lapilli tuff (Lt_1). One metre hammer for scale. C) Field photo showing ~10 m wide and ~4 m thick exposure of moderately to poorly sorted, locally spatter dominated, lapilli tuff (Lt_3). One metre hammer for scale. The white box shows the location of the inset displaying fluidal clast surrounded by a vitric ash matrix.

Figure 5: Field photos illustrating the association of pillowed lava (Lpi), peperitic dykes (Ld_1), and enclosing lapilli tuff (Lt_1): A) Photomosaic of ~30 m wide by~ 4 m thick exposure of pillowed lava (Lpi) mingled with massive lapilli tuff (Lt_1). Inset (white box) shows pillowed lobes with a lens of Lt_1. ~~Hammer (1 m~~One metre hammer (white arrow) for scale. B) Annotated version of 5A. Note preserved lenses of Lt_1 within extensive Lpi deposits. C) Field photo showing ~~~5m~~5 m wide and ~~~4m~~4 m deep exposure of "blooming" pillowed lava (Lpi) within massive lapilli tuff (Lt_1). Note a feeder dyke (Ld_1) (white arrow) is visible through the coherent Lpi body. Inset (white box) shows pillowed lava in contact with a lens of Lt_1. D) Annotated version of 5C.

Figure 6: Field photos illustrating the association of pillowed lava (Lpi) with peperites (Pi) and peperitic textures present at Cracked Mountain: A) Photomosaic of ~10 m wide and ~4 m thick exposure volcaniclastic peperite (Pi) formed along the margins of coherent bodies of pillowed lava (Lpi). ~~Human~~Tape measure (white arrow) and human for scale. Inset (white box) shows quench-fragmented peperite bounding Lpi. Marker for scale. B) Annotated version of 6A. C)

Example of globular (fluidal) peperite (Pi) texture. Pen for scale. D) Example of blocky peperite (Pi) texture. Pen for scale.

Figure 7: Field photos illustrating the structure and variable clast types found in Cracked Mountain tuff breccias (Tb). A) Massive, ~1.5 m thick, tuff breccia (Tb) dominated by subrounded to blocky lava, overlying massive lapilli tuff (Lt_1). Hammer (1 m) for scale. B) Massive, tuff breccia (Tb) dominated by subrounded to blocky lava, with minor, block-sized lapilli tuff lithics (Lt_1) (white arrows). C) Rare lithic of pahoehoe (Ls) entrained within tuff breccia (Tb). Hammer (1 m) for scale.

Figure 8: Field photos illustrating pillow and subaerial lavas from Cracked Mountain. A) Stacked sequence of pillow lavas (Lp) (view looking NW at SE base of CM), ~150 m wide and ~40 m thick. White arrows mark approximate edifice basement contact at 1500 m a.s.l. B) Wall of pillow lava (Lp), ~10 m high, exposed on the S margin of the volcano. C) Coherent bulbous pillow lobes (Lp) up to ~0.5 m in diameter. ~~Hammer (1 m~~One metre hammer (white arrow) for scale. D) Remnant flow-top of jointed sheet lava (Ls) near the summit of the volcano (~1,600 m a.s.l). Black arrows show granitic erratics and scour marks covering the surface of the lava. Hammer (1 m) for scale.

Figure 9: Photomicrographs showing textures of CM volcaniclastic lithofacies. A~~-D~~C, E, G, and ~~G~~H are plane-polarized images at 4x magnification with a ~~white~~ 2 mm scale. D and F are from Scanning Electron microscopy (SEM), shown with a 300 µm scale bar. A) Photomicrograph of interstitial pillow lava sediment (Lp) ~~comprised~~composed of coarse, jig-saw fractured, weakly vesiculated glass. B) Photomicrograph of massive, ash, and lapilli tuff (Lt_1) showing fine-grain juvenile clasts including microlitic (Mlt), blocky (Bl), and highly vesiculated (Vsc) vitric clasts. The matrix contains a small proportion of intact to fragmented olivine (Ol) and plagioclase crystals. C) Photomicrograph of massive lapilli tuff (Lt_1) showing size range of juvenile vitric clasts and shapes (i.e. blocky and cuspate). D) SEM photomicrograph of 9C showing both blocky and highly cuspate vesiculated shapes of fine ash fraction (~ 100 µm). E) Photomicrograph of massive lapilli tuff (Lt_1) showing coarse to fine juvenile clasts and fragmental crystals olivine and plagioclase. Highly vesiculated vitric clasts are abundant. F) SEM photomicrograph of 9E showing a highly vesiculated (50-60%) coarse vitric juvenile clast. G) Photomicrograph of thinly bedded lapilli tuff (Lt_2) showing layers of ultra-fine ash separating layers of coarser, blocky (Bl), and vesiculated (Vsc) vitric clasts. H) Photomicrograph of matrix material supporting spatter dominated lapilli tuff (Lt_3) showing a highly vesiculated, vitric juvenile lapilli clast within an ash and fine lapilli-sized vitric matrix.

Figure 10: Major (XRF) and trace elemental (ICP-MS) compositions for whole-rock samples (white) and glasses (black) from Cracked Mountain. A) Total alkali ($Na_2O + K_2O$) vs Silica (SiO_2) wt. % (TAS) with the classification of Le Bas et. al. (1986) and Irvine and Baragar (1971). B) Mg# (molar MgO/ (MgO +FeO*)∗100) vs Silica (SiO_2) wt. % for Cracked Mountain volcanics. CM samples not measured with ferric titration use the mean value of Fe 2+/ Σ Fe =0.7228 (N=7) for CM basalts that were determined. C) Rare Earth Trace Element (REE) compositions of Cracked Mountain volcanics, normalized to a ~~primitive mantle (P mantle)~~Chondrite after Sun and McDonough (1989).

Figure 11. Stereographic plots of ~~magnetic~~paleomagnetic remanence directions for Cracked Mountain volcano and examples of typical, well-behaved demagnetization data. A) Stereographic plot of mean data from CM Sites 2-9 and their α_{95} (p = 0.05) confidence circles (see Table C1). The mean of sites 2-9 ~~are~~ is shown in red. Geocentric Axial Dipole (GAD) field inclination for sampling latitude is shown with a filled square (see Table C1). Present Earth's Field direction (PEF) is shown with a filled star (see table C1). Site 1 is excluded as it is an outlier (see details in Appendix C) that appears to represent rotation associated with extensional collapse. B) Stereographic plots (left) show magnetization directions after stepwise AF and thermal demagnetization of the Lt_1 sample from Site 2 (~~CMV060A~~CMV015A/B), where the filled circles lie on the lower hemisphere. Precision values, given as the maximum angle of deviation (MAD) are included. Orthogonal plots (right) show horizontal projections as filled circles and vertical projections as open circles. Natural remanent magnetization is shown with a circle and cross. Units are in amperes per metre. Note that AF demagnetization for sample ~~CMV060B~~CMV015A produces more coherent results than does thermal demagnetization. C) Well-behaved stepwise demagnetization data for a dyke (Ld_1) sample collected at Site 6 (CMV029A/B), layout, symbols, and units as 12B. Note, this sample shows identical results for AF and thermal demagnetizations. Based on the results of detailed AF and thermal demagnetization of pilot specimens from each site, AF demagnetization is the preferred treatment.

Figure 12: Schematic model (2x V.E) of volcanic evolution of CM. Stage 1: Explosive phreatomagmatic eruptions, building a subaqueous tephra cone. Stage 2: The sustained intrusion of lava into unconsolidated sediments, and endogenous growth of the edifice. Dykes that breached the margins of the volcanic pile produced pillowed lavas within the englacial lake. Stage 3: Involves the buildup of CM to the level of the englacial lake (or above) and subaerial eruption of lava as well as syn-eruptive debris flows forming deposits of massive tuff breccia. Schematic drainage channels are shown forming through the ice sheet. Stage 4: Post-eruptive, glacial retreat, where the top of the edifice is scoured off. Additionally, the removal of glacially confined margins causes extensional, gravity-driven stress on of the overs steeped volcanic successions, causing cracks to form and partial edifice collapse.

Figure 13: Paleoclimate glacial reconstruction at the time of Cracked Mountain eruption, ~401 ka. A) Hillshade DEM for CM map area overlain showing the dispersal of glacial ice. We use the approximate summit of CM (~1650 m a.s.l) as the minimum height at which glacial ice is reached. All regions below 1650 m are shown in light blue (i.e. ice) and all regions above 1650 m are shown in brown. CM edifice is shown in green within a schematic englacial lake. B) Undivided N-S (A-A') and E-W (B'-B) cross-sections for CM, shown at no VE. Volcanic rocks (green) overlie basement (pink) above steep valleys to the N (Meager Creek) and W (Elaho Valley). Schematic glacier ice is shown confining CM with an englacial lake forming around the volcano. The minimum thickness of the englacial lake is ~250 m estimated from the total thickness of the edifice. C) Schematic 3D DEM is shown for the CM map area. The same colours and symbols were used in ~~14A~~13A. Glacial ice is shown reaching minimum elevations of 1650 m a.s.l. with a minimum thickness of ~850 m based on the elevation of Meager Creek. Schematic drainage channels are shown based on the physiographic setting of the edifice.

Figure 14: Mid to late Pleistocene Marine $\delta^{18}O$ (‰) isotope record (MIS), modified from Lisiecki and Raymo (2005) showing fluctuations (and numbered stages) in global ice from, where higher $\delta^{18}O$ represents periods of more global ice and lower $\delta^{18}O$ represents periods of lower global ice. The vertical axis is a record of time (ka) with magnetic pole orientations shown through the Pleistocene. Dark bars are times of normal polarity and white bars are times of pole reversal. The dashed box indicates the blow-up portion of the MIS from 250-600 ka. The Cracked Mountain plateau age of 401.6 ± 38.1 ka is plotted (grey shaded) on the blow-up MIS portion, representing times from the waning of MIS 12 through MIS 11. The preferred age of Cracked Mountain is indicated with a dashed line at ~425 ka.

Highlights:

- Cracked Mountain is Pleistocene (~425 ka) tuya in Canadian Cascades
- Lithofacies indicate explosive onset to subaqueous monogenetic eruption
- Eruption was within an englacial lake having (depth of 250 m; volume of 0.36 km^3)
- Glaciovolcanic record implies regionally > 850 m thick ice sheet at ~425 ka

Figure 1

Click here to access/download;Figure;Fig 1_revised_1_06_22.pdf

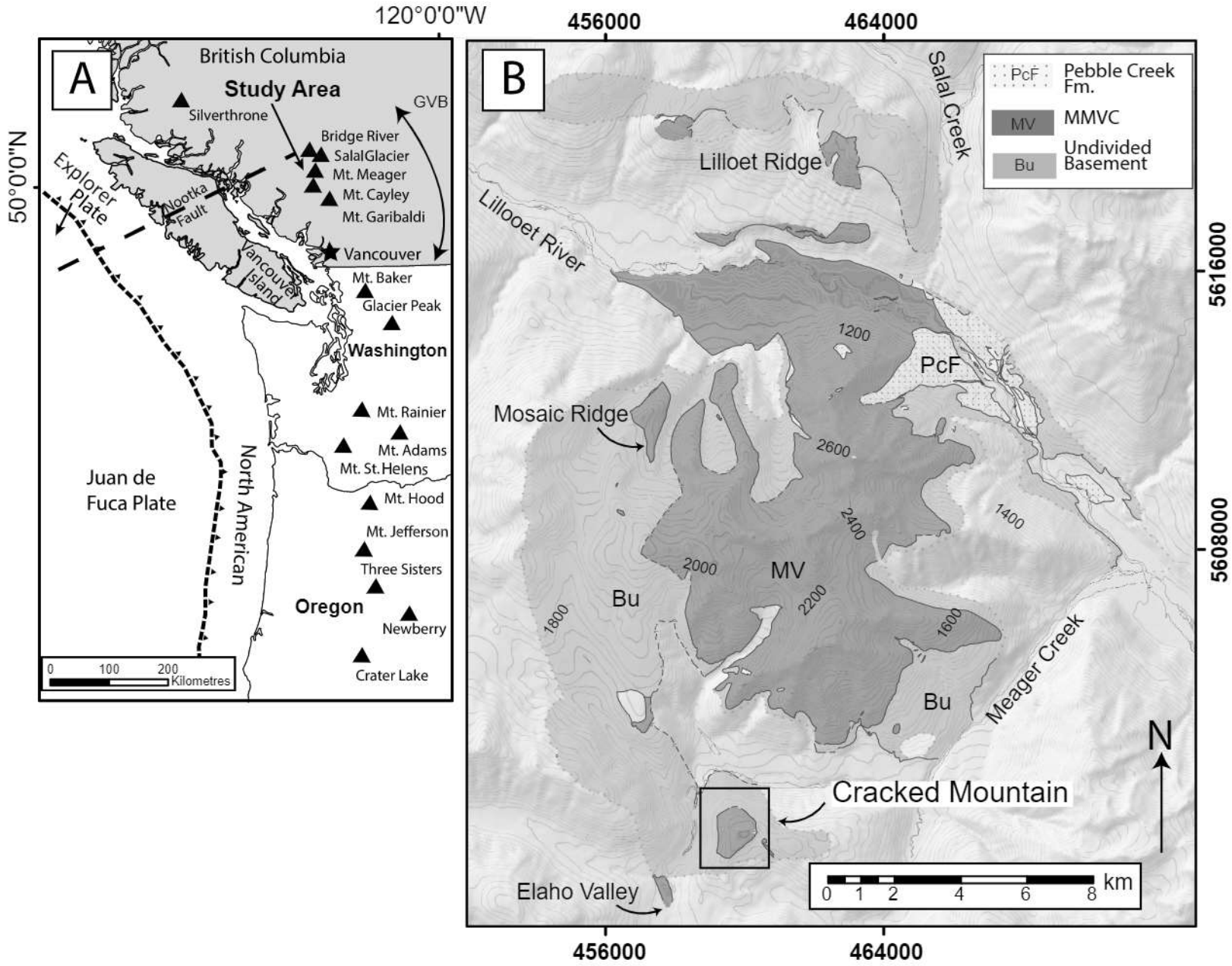

Figure 2

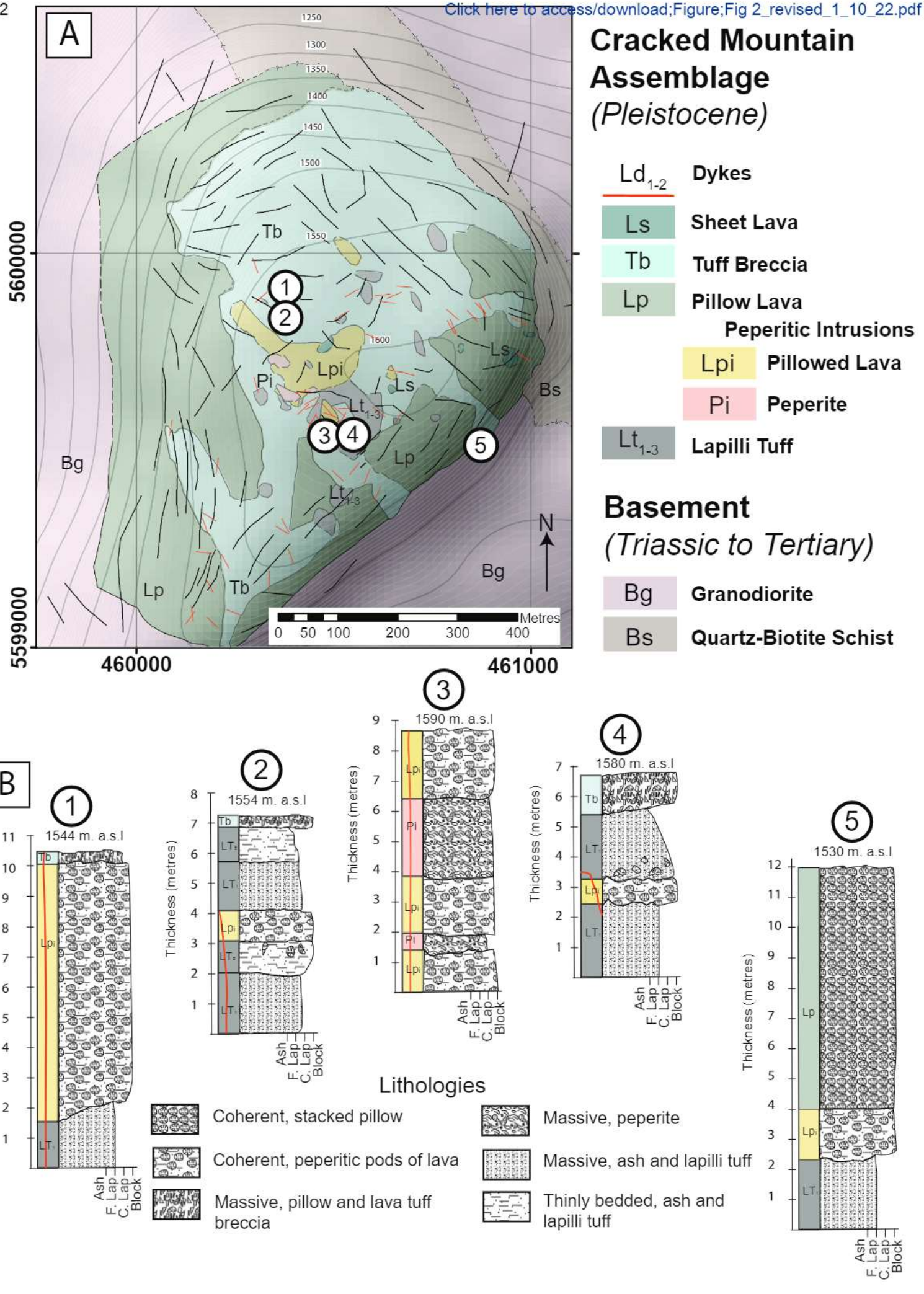

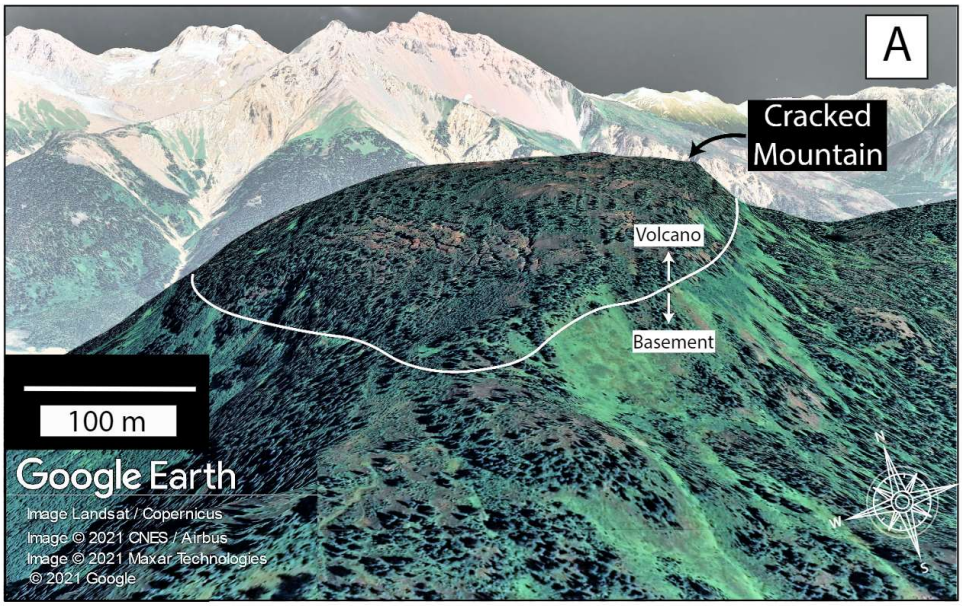

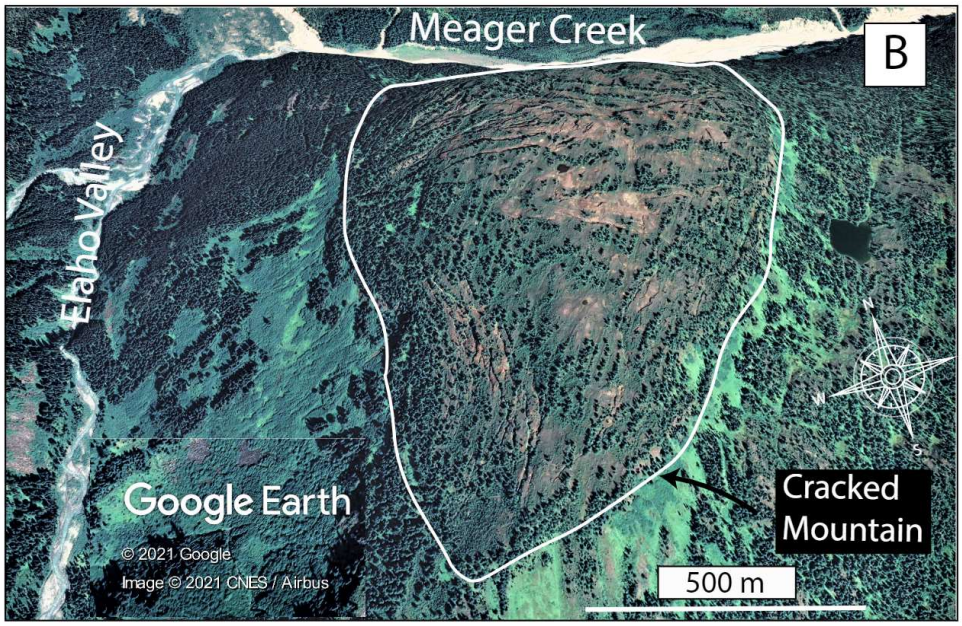

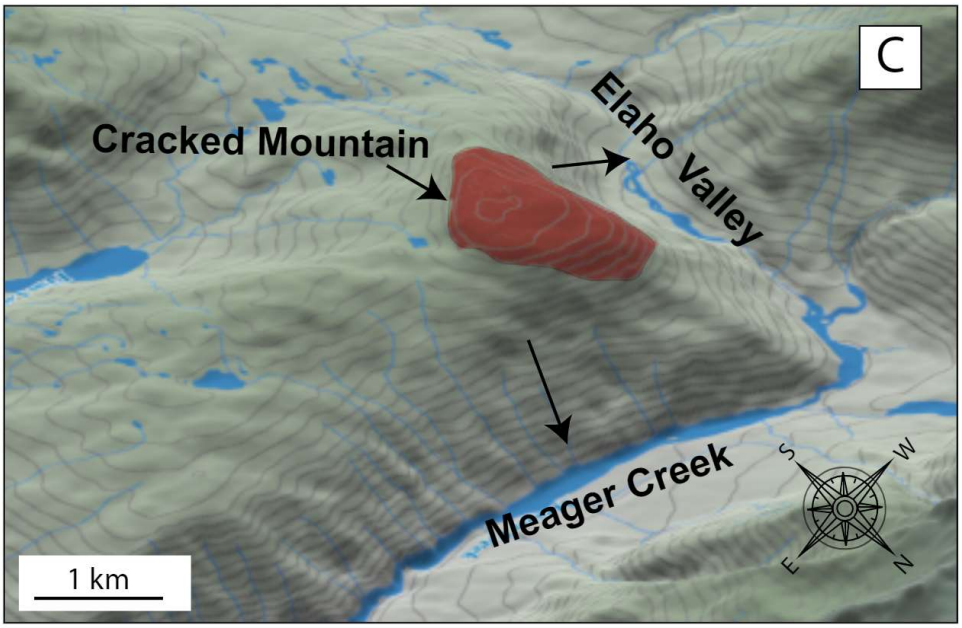

Figure 4

Click here to access/download;Figure;Fig 4.eps

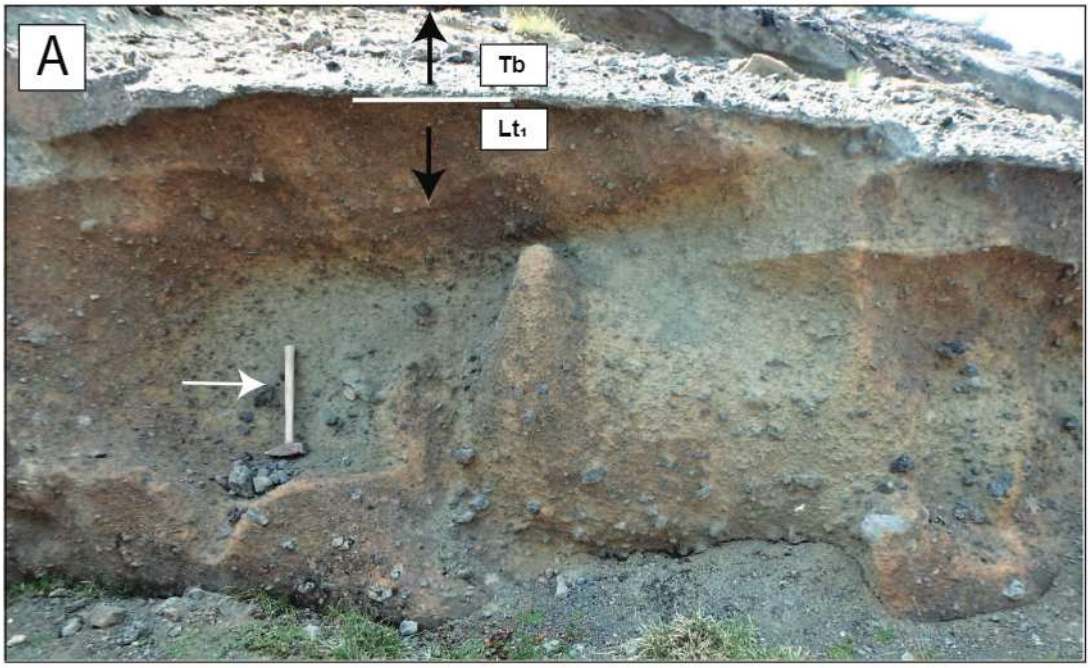

Figure 5

Click here to access/download;Figure;Fig 5.eps

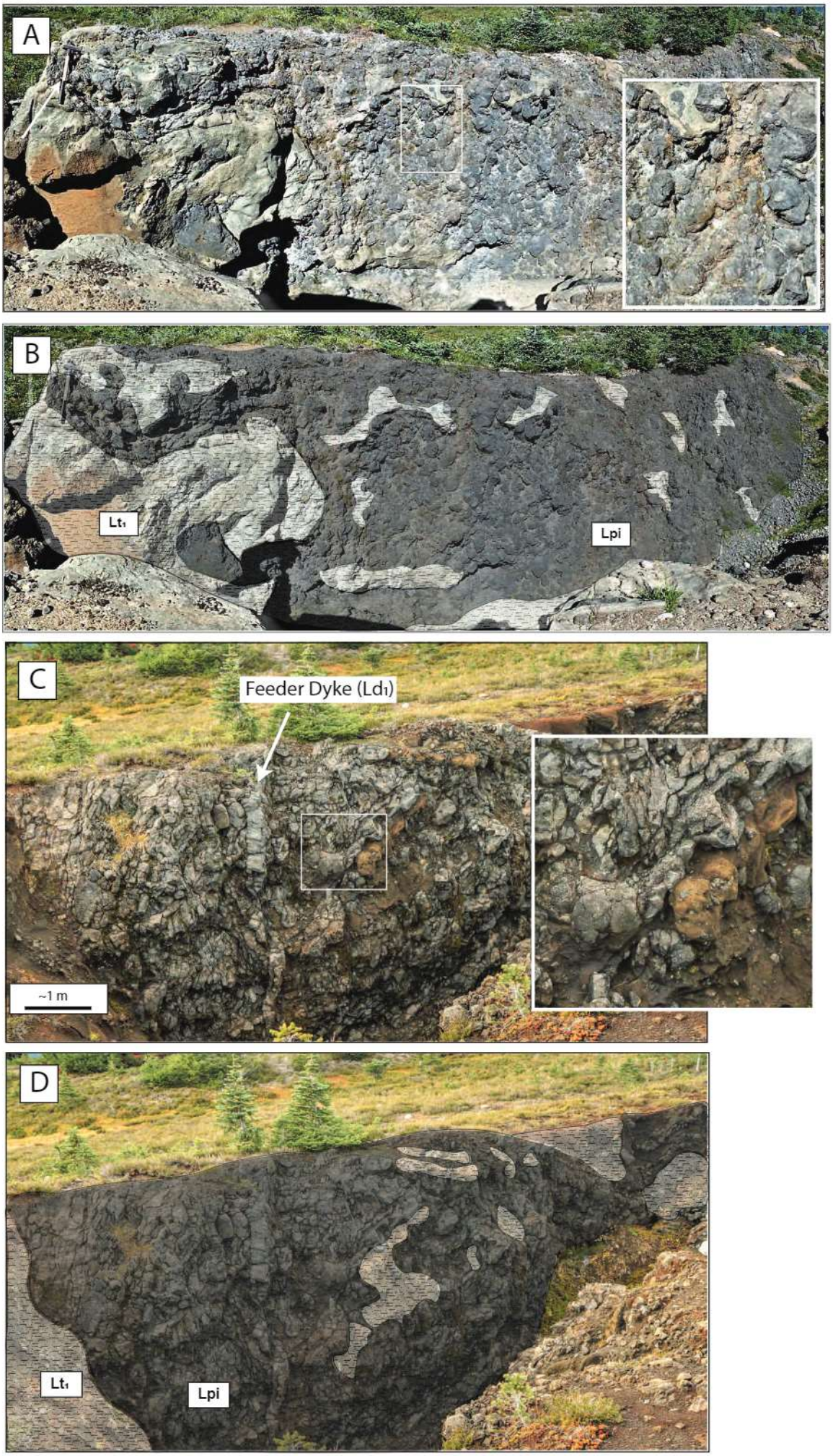

Figure 6

Click here to access/download;Figure;Fig 6.eps

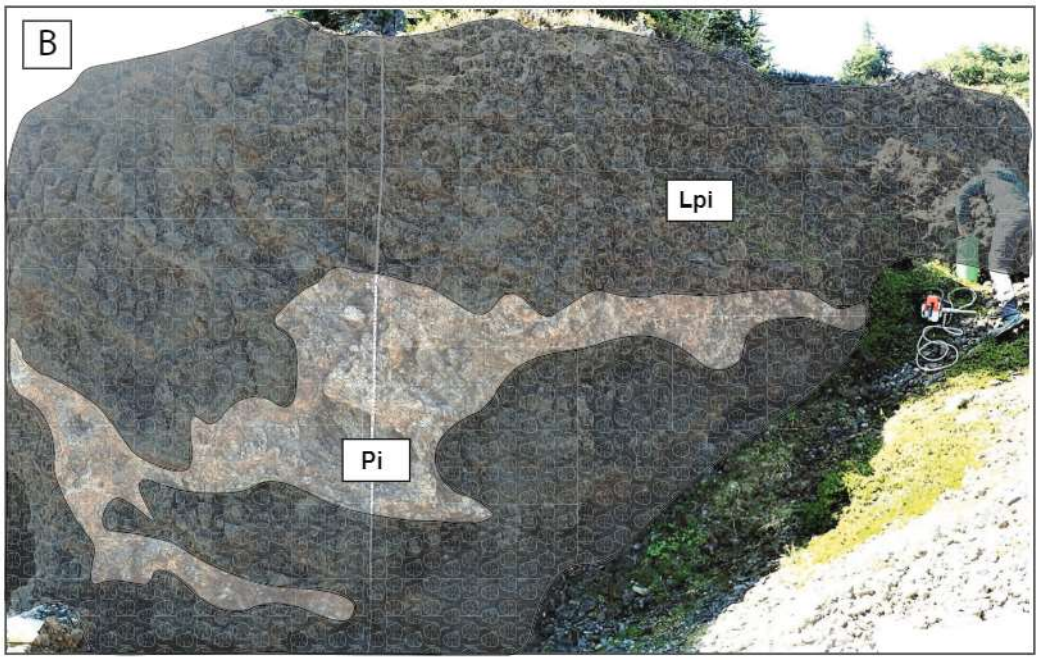

Figure 7

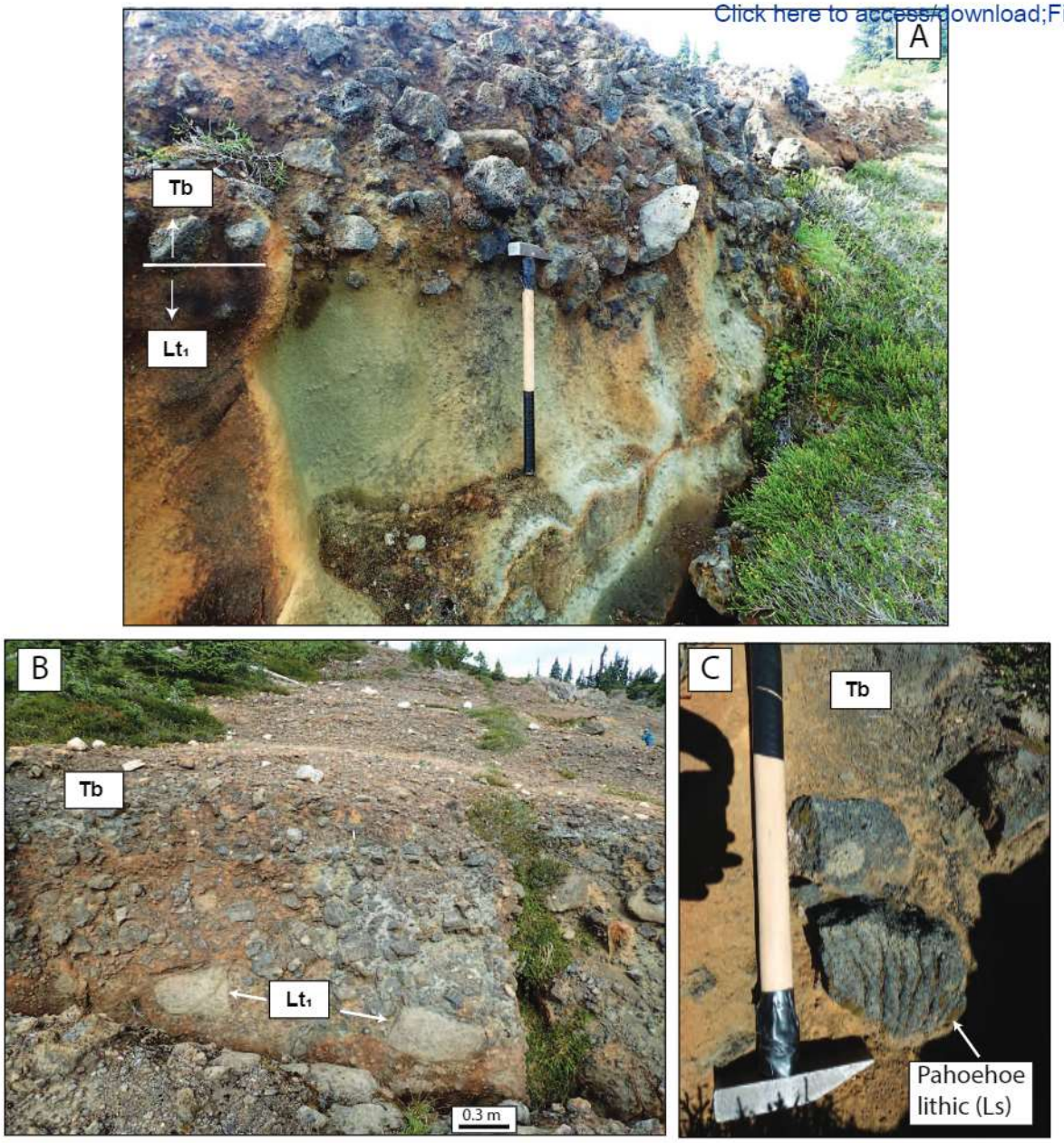

Figure 8

Click here to access/download;Figure;Fig 8.eps

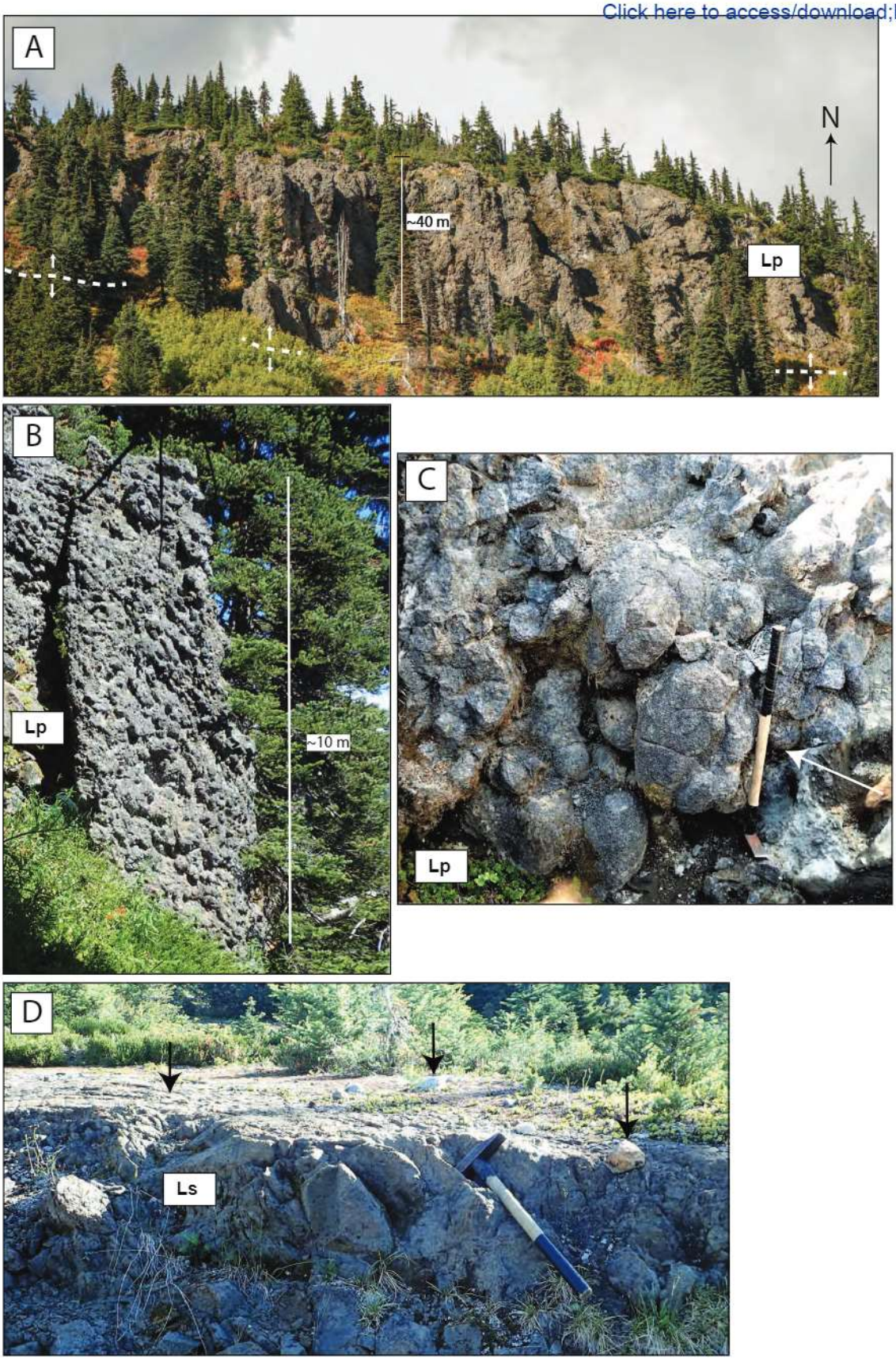

Figure 9

Click here to access/download;Figure;Fig 9.pdf

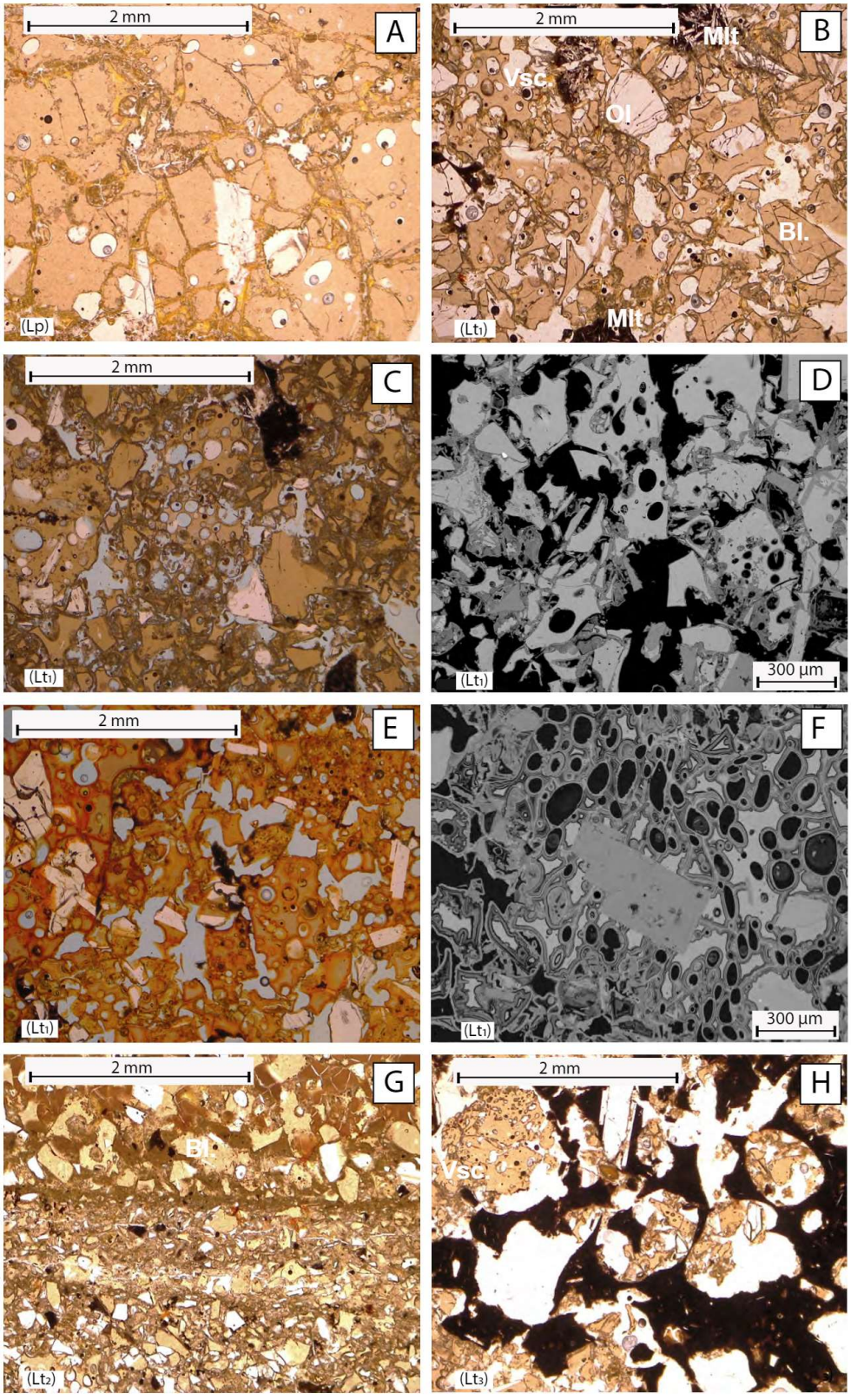

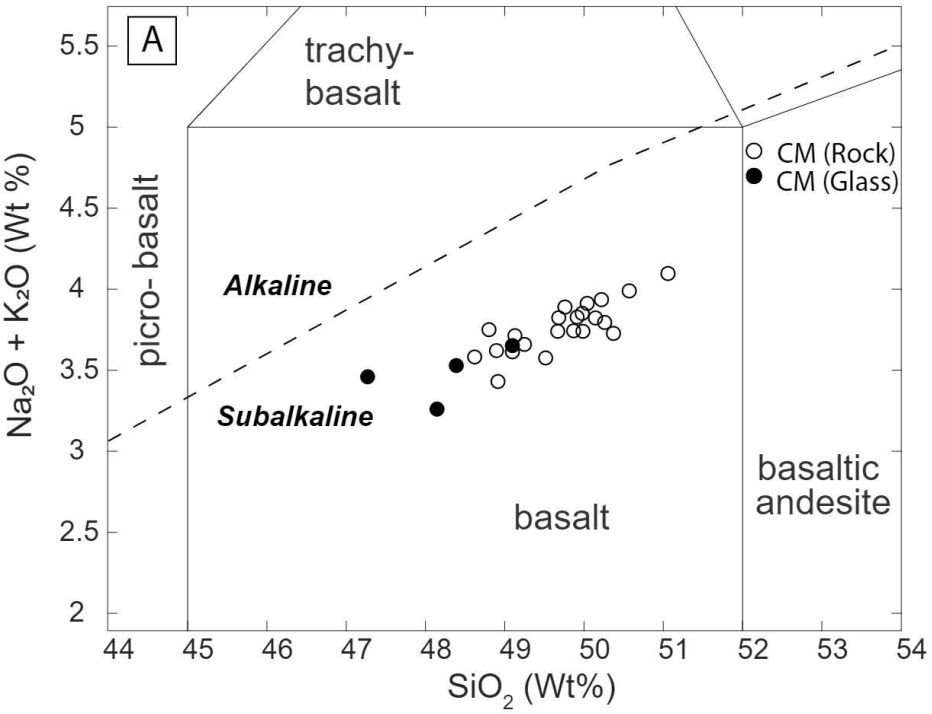

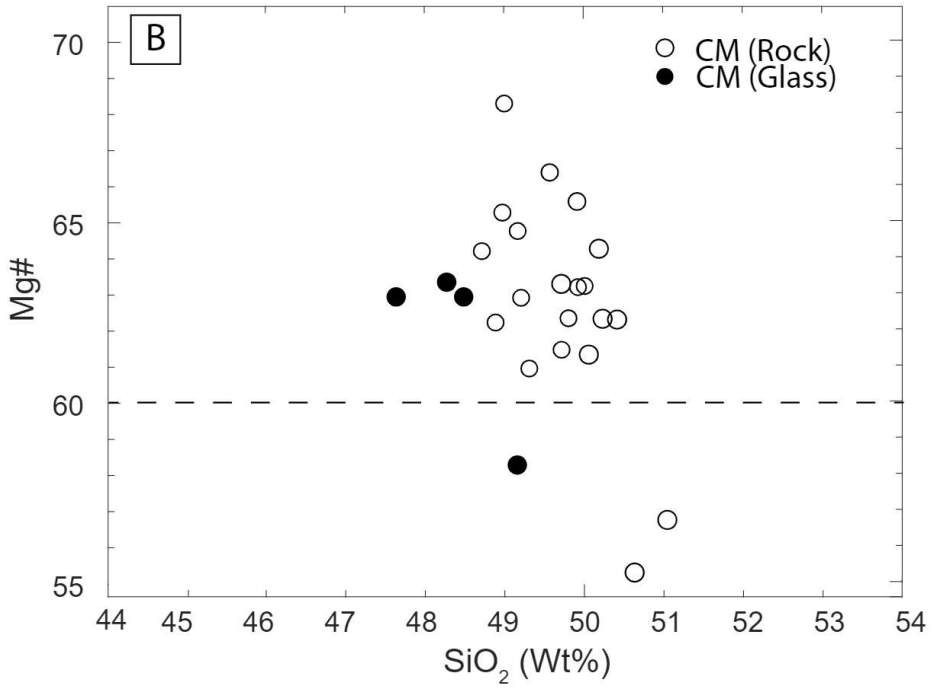

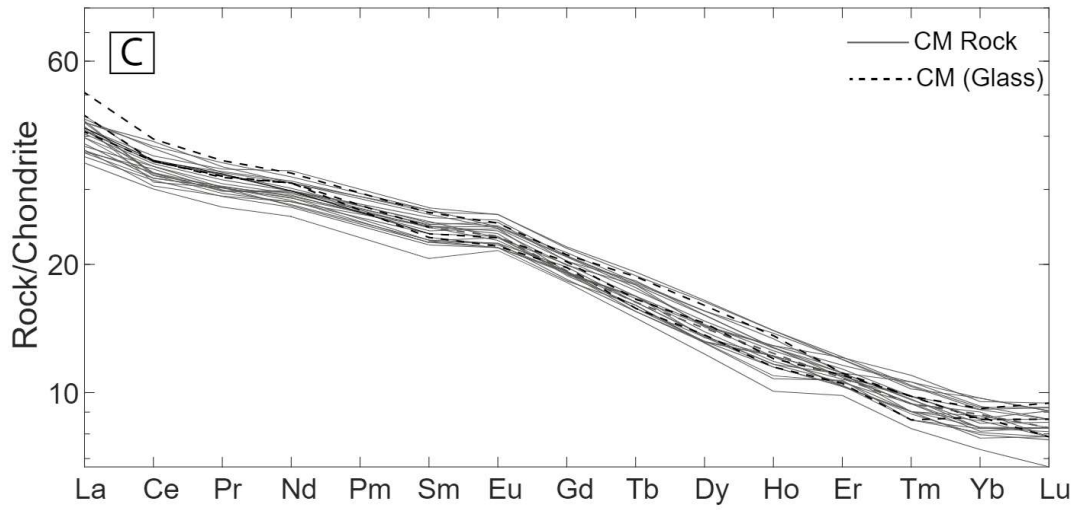

Figure 11

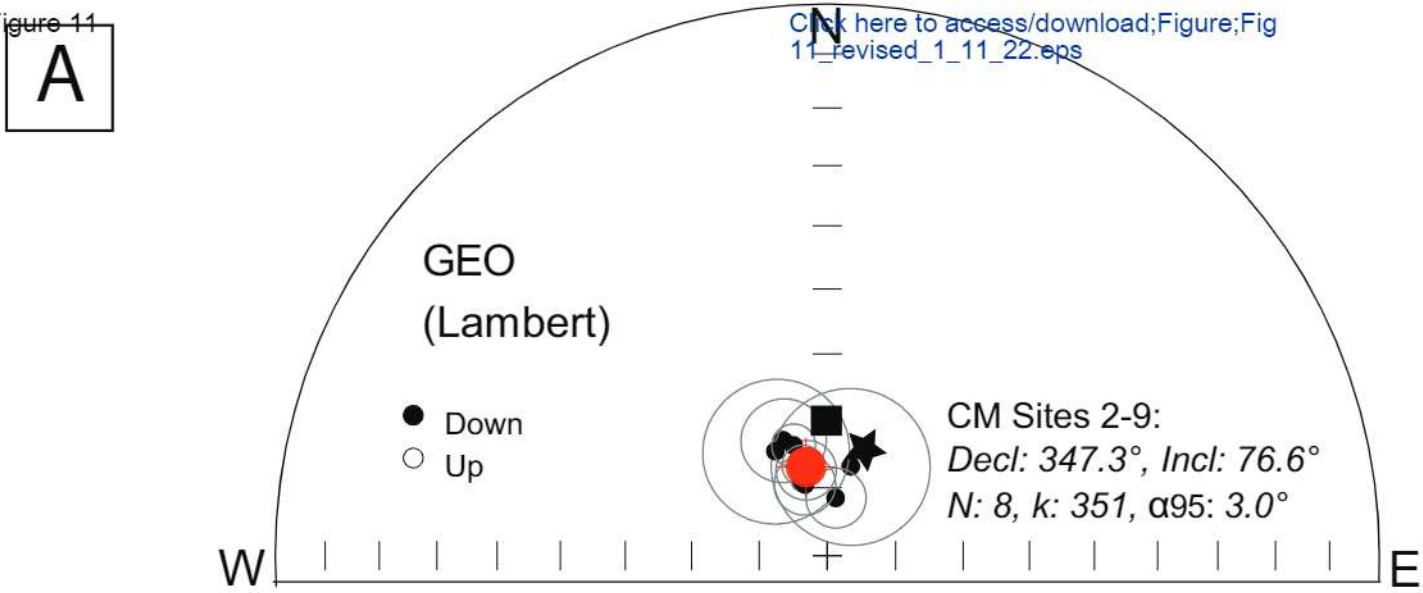

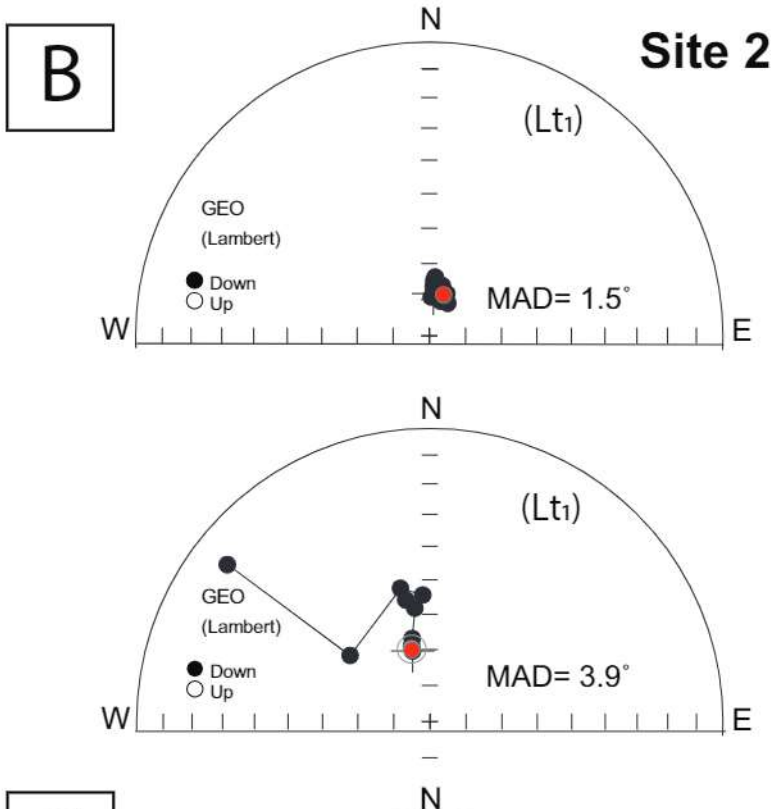

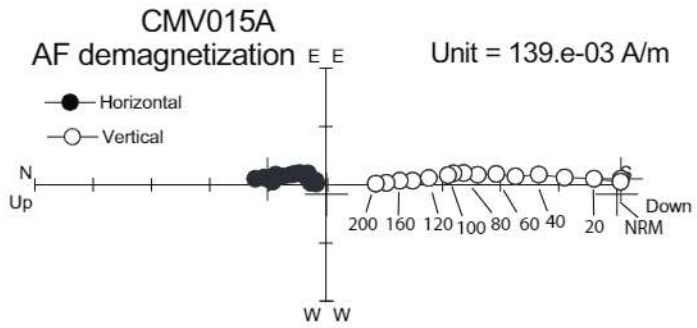

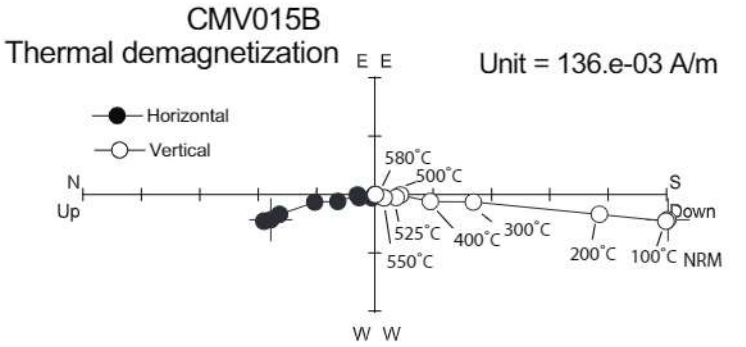

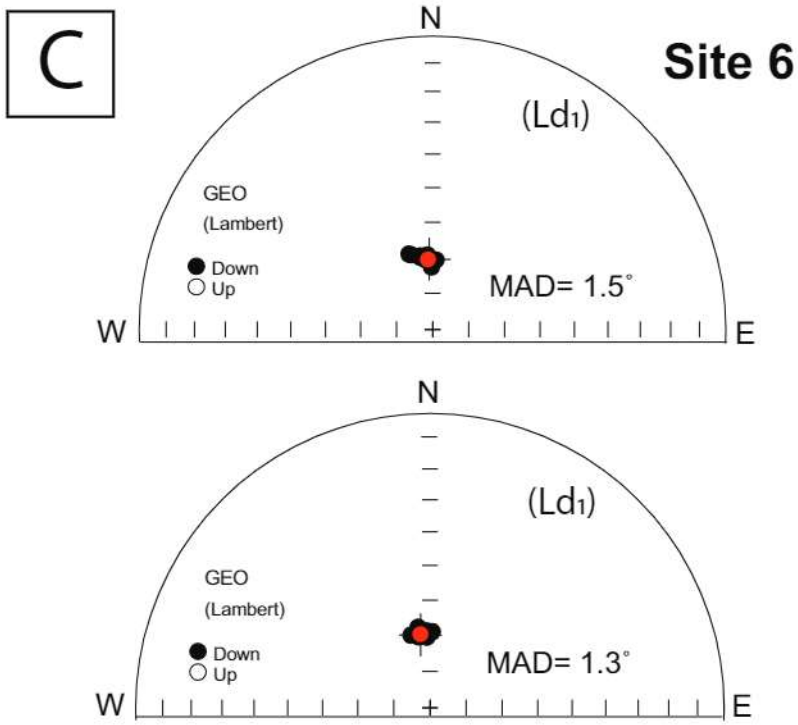

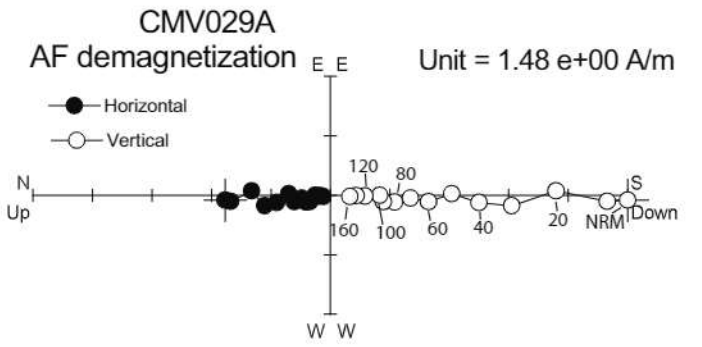

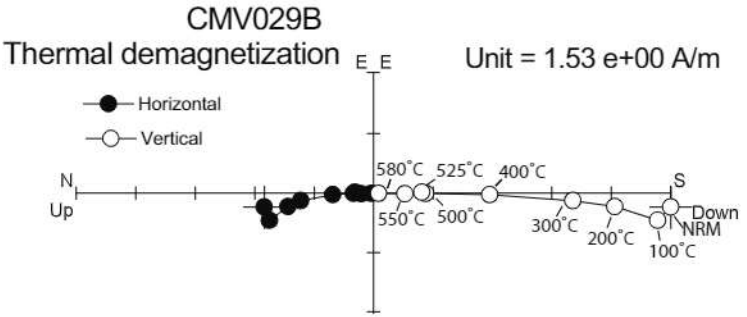

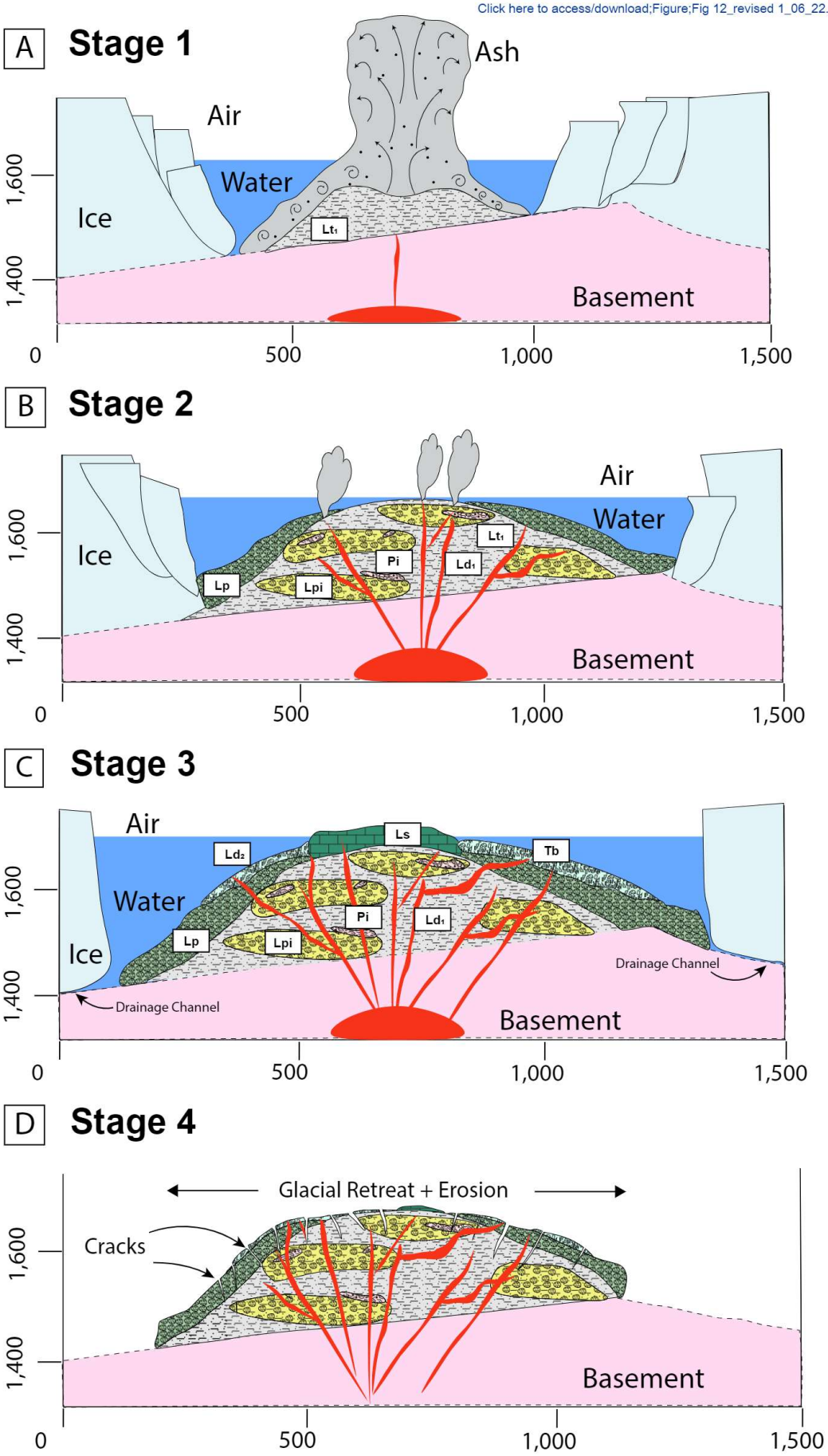

Figures 13

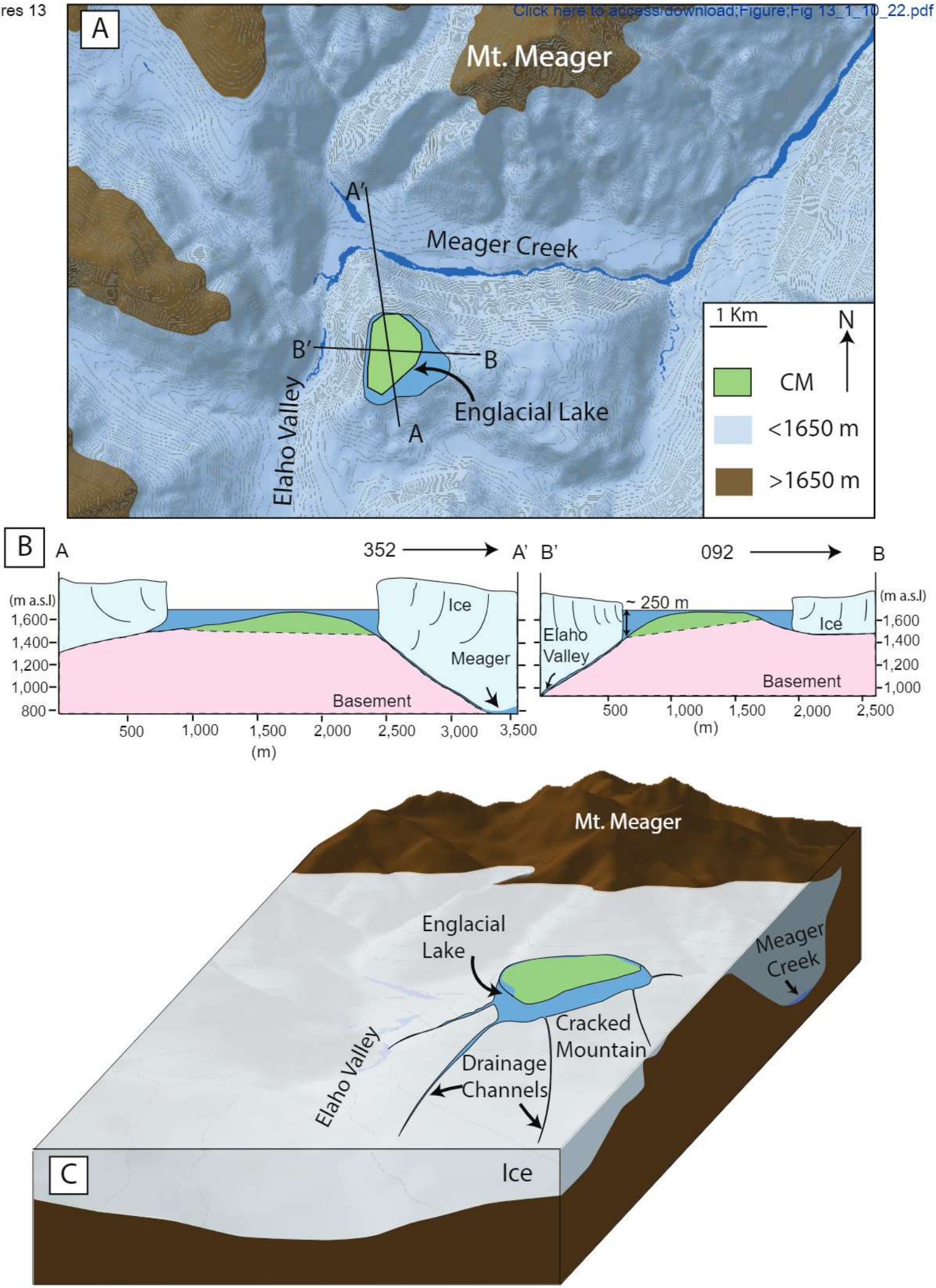

Figures 14

Click here to access/download;Figure;Fig 14 revised 12_23_21.pdf

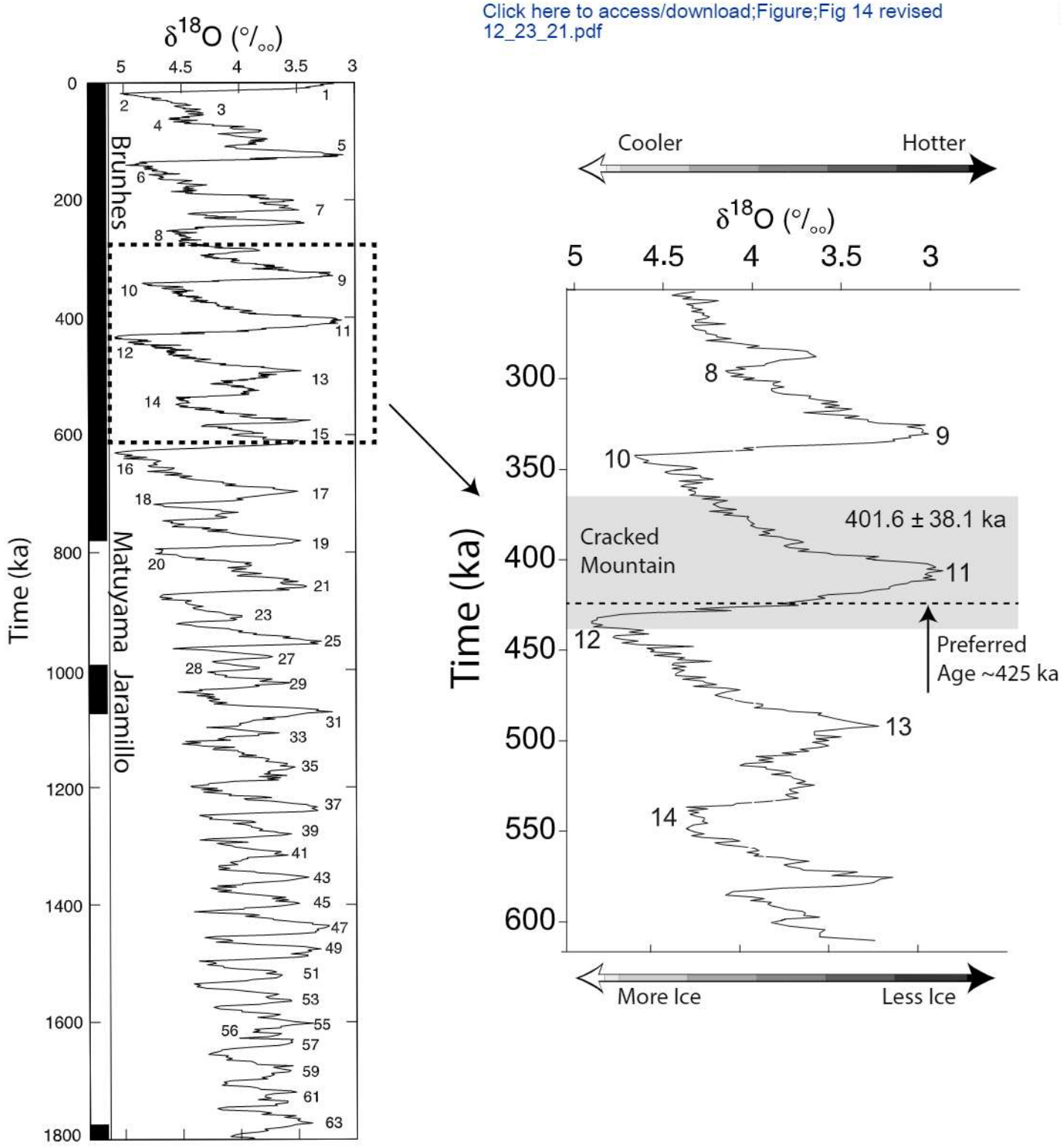

Table 1. Codes, descriptions, approximate edifice volume, and interpretations of Cracked Mountain volcanic lithofacies.

	Facies Code	Vol. %	Description	Interpretation	Figs.
Volcaniclastic	Lt_1	25	Lapilli Tuff: Yellow to grey; massive to crudely bedded, monolithic, moderately to well sorted, and matrix-supported; clasts comprise 10-30% of the unit, with ~10-25% lapilli and >5% blocks; ~20-50% of clasts are glassy, highly vesiculated juveniles, with all other clasts being dense lava lithics; dense clasts are olivine and plagioclase porphyritic, Pl (5-10%) Ol (5%) with < 50% showing chilled margins.; matrix material is yellow-orange ash and fine lapilli, comprised of ultra-fine (~5%), blocky (~60%), and cuspate (~30-35%) vitric juveniles; matrix contains intact to fragmented crystals, Pl (5-10% 0.5-2 mm) and Ol (5-10% 0.1-1 mm); lapilli tuff is stratigraphically lowest throughout the edifice.	Subaqueous pyroclastic density currents are derived from Surtseyan tephra cone buildup from the onset of the eruption.	2, 4, 5, 7
	Lt_2	3	Lapilli Tuff: Yellow to grey; thinly bedded, monolithic, moderately to well sorted, and matrix-supported; clasts comprise >10% of the deposit, with 100% being fine lapilli; ~50% of clasts are highly vesiculated vitric juveniles, and ~50% dense basalt lithics; dense lithics are olivine and plagioclase porphyritic to microlitic, Pl (5-10%) Ol (5%); matrix material is yellow ash, comprised of ultra-fine (~10-15%), blocky (~70%), and cuspate (15-20%) vitric juveniles; matrix contains intact to fragmented crystals, Pl (5-10% 0.5-2 mm) and Ol (5-10% 0.1-1 mm).	Subaqueous low density (surge) deposits during the phreatomagmatic buildup of the edifice.	2, 4
	Lt_3	1	Lapilli Tuff: Grey; massive, monolithic, poorly sorted, and matrix-supported; clasts comprise ~20-40% of the deposit, with ~10-15% lapilli and ~20% block; ~50% of clasts are highly vesiculated, fluidal to blocky, spatter juveniles, and ~50% dense basalt lithics; clasts are olivine and plagioclase porphyritic, Pl (5-10%) Ol (5%); the matrix grey, well-sorted, fine lapilli and ash, comprised of ultra-fine (~5%), blocky (~50), and cuspate (~45%) vitric juveniles; matrix contains intact to fragmented crystals, Pl (5-10% 0.5-2 mm) and Ol (5-10% 0.1-1 mm).	Shallow subaqueous to subaerial lava fountaining during the phreatomagmatic buildup of the edifice.	2, 4

	Facies Code	Vol. %	Description	Interpretation	Figs.
Volcaniclastic	Pi	3	Peperite: Yellow to grey; massive, monolithic, moderately sorted, matrix to clast supported; clast shapes range from globular to blocky, clasts comprise <50% of the deposit, with ~40% lapilli and ~10% blocks; clasts ubiquitously show chilled margins and display jig-saw fracture patterns; clasts are vitric and highly vesicular, up to 50-60%, and are olivine and plagioclase porphyritic, (Pl 5-10%, Ol 5%); matrix material is yellow-orange ash, comprised of ultra-fine (~5-10%), blocky (~60%), cuspate (~30%) vitric juveniles; Pi is stratigraphically adjoining Lpi throughout the edifice.	Quenched volcaniclastic material formed along with bodies of (Lpi) by fuel coolant reactions within water-saturated, unconsolidated lapilli tuffs (Lt1).	2, 6
	Tb	16	Tuff Breccia: Yellow to grey; massive, monolithic, moderately to poorly sorted, and clast supported; clasts are subrounded to angular, ranging from 65-70% coarse lapilli and ~5-10% blocks; 10-30% of components are subrounded pillow lithics (Lpi, Lp), ~60-70% are dense to highly vesiculated blocky lava (Ls), and ~1-2% are lapilli to block-sized rounded lapilli tuff lithic (Lt1); all coherent clasts are olivine and plagioclase porphyritic, Pl (5-10%) Ol (5%); matrix material is yellow-orange ash and lapilli, comprised of ultra-fine (~5%), dense (~60%), and cuspate (~35%) vitric juveniles; breccia blankets and fills in topography throughout the edifice.	Near and proximal vent syn- and post-depositional debris flow avalanches in subaqueous and subaerial settings.	2, 7
Coherent	Lp	20	Pillowed lava: Dark grey to black; intact to fragmented, rounded to oblong lobes, with individual diameters ranging from 0.2 to 0.5 m; vitric rims up to 1 cm are common; pillows are moderate to highly vesicular (50-65%) and commonly display concentric vesicle layers in cross-section; pillows are hypocrystalline, and olivine and plagioclase porphyritic, Pl (10-15%, 0.5-3 mm), Ol (5-10%, 0.1-1 mm); rare augite phenocrysts are observed in thin-section, Cpx (1-2%, 0.1-1 mm) pillows contain yellow-orange interstitial quench fragmented ash and lapilli between adjacent lobes.	Subaqueous extrusion of lava at moderate to low eruption rates within the ice-confined glacial lake.	2, 8

	Facies Code	Vol. %	Description	Interpretation	Figs.
Coherent	Lpi	20	Pillowed lava: Dark grey to black; domains of intact to dispersed, subrounded to oblong pillowed lobes, with individual diameters ranging from 0.2 to 0.5 m; vitric rims up to 1 cm are common; lobes are moderate to highly vesicular (50-65%) and commonly display concentric vesicle layers in cross-section; lobes are hypocrystalline, and olivine and plagioclase porphyritic, Pl (10-15%, 0.5-3 mm), Ol (5-10%, 0.1-1 mm); lobes are mingled within moderately to highly palagonitized lapilli tuffs. Corrugated vitric rinds cover lobes and tubes in some exposures.	The subaqueous intrusion of lava into unconsolidated, water-saturated volcaniclastic sediments (Lt1).	2, 5
	Ls	2	Jointed lava: Dark grey to black; columnar to blocky jointed, columns range from 0.2 to 0.5 m in diameter; lavas are dense, with moderate vesicularity (~20-30%); lavas are holocrystalline and are olivine and plagioclase porphyritic, Pl (10-15%, 0.5-3 mm), Ol (5-10%, 0.1-1 mm); rare augite phenocrysts are observed in thin-section, Cpx (1-2%, 0.1-1 mm), little to no interstitial sediments are present between jointed lavas. Outcrops are poorly preserved and show signs of glacial scouring.	Subaerial extrusion of lava at moderate to low eruption rates, at elevations above englacial lake level.	2, 8
	Ld_1	5	Dykes: Dark grey to black; subvertical to curved, thickness ranges from 0.5 to 1.5 m; dyke margins are poorly defined to pillowed margins; dykes are moderately vesicular (~20-40%); dykes are holocrystalline, and are olivine, plagioclase (glomero) porphyritic, Pl (10-15%, 0.5-3 mm) Ol (5-10%, 0.1-1mm)	Early-stage intrusions into unlithified Lt1 coinciding with emplacement of coherent lavas (Lpi, Lp).	2, 5
	Ld_2	5	Dykes: Medium to dark grey; subvertical and jointed, thickness ranges from 0.5 to 3 m; dyke margins are well defined with laterally pointing small columnar joints; dykes are moderately vesicular (~20-40%); dykes are holocrystalline and are olivine, plagioclase, and augite (glomero) porphyritic, Pl (10-15%, 0.5-3 mm) Ol (10%, 0.1-1mm) Cpx (1-2%, 0.1-1 mm); dykes contain minor crustal xenoliths.	Late-stage intrusions postdating lithification of Lt1 and growth of edifice.	2

Table 2. Summary of distribution, descriptions, and interpretations of lithofacies associations at Cracked Mountain

Association	Lithofacies present	Stratigraphic relationships	Distribution	Interpretation	Figs.
(A)	Lt1, Lpi, Ld1	Lt1 is intruded by Ld1 and mingled with Lpi; Lpi blooms away from pillowed margins of Ld1	Ubiquitous in crack exposures throughout mid and upper elevations of the edifice; small localized outcrops at the base of edifice near basement contact	Lt1 was deposited in a water-rich environment and was intruded by Ld1 while it was still unconsolidated; as the Ld1 entered the saturated unconsolidated Lt1, the injecting magma pillowed due to water-rich environments and disaggregated due to reduced pressure	5
(B)	Lpi, Pi	Pi is interbedded and adjacent to coherent Lpi, at times forming gradational contacts	Pi is exposed at the surface in small outcroppings in the central and high elevations of the edifice but is commonly observed within cracks exposures across the whole mountain	Pi formed along the margins of larger pods of Lpi where the highly saturated host sediment caused quenching and disaggregation of magma from the margins of the host intrusion.	6
(C)	Ls, Tb, Lp, Lpi, Lt1-3	Ls and Tb overly Lp, Lpi, and Lt1-3; Lithics of Ls, Lp, Lpi, and Lt1 are entrained within Tb	Ls outcrops sporadically as small remnant outcrops near the present-day summit of the edifice, Tb blankets and fills topography, extending from the central summit toward the outer margins of the edifice	Ls formed subaerially as the englacial lake level dropped below the elevation of erupting magma; Tb formed as lava piles and slopes collapsed from over steepening and/ or oversaturation, spreading out as mass flow breccias across the highest levels of volcanic stratigraphy; near the summit and central vent, explosive bursts ejected ballistics of subrounded Lt1 which are entrained in Tb	7, 8
(D)	Ld1 Ld2, Ls, Tb, Lp, Lpi, Pi, Lt1-3	Ld2 cuts through all other lithofacies.	Ld2 is present in the central vent area and high elevations of the edifice as well as seen cutting along the stacked lava at the edges of the mountain	Ld2 represent the latest stage of the Cracked Mountain eruptions; the other lithofacies were already cooled and lithified prior to these late-stage intrusions	

Table 3. Representative whole-rock major (wt. %) and rare earth (ppm) element compositions of Cracked Mountain volcanic rocks analysed by X-ray fluorescence and ICP-MS, respectively. Analytical precision (2s) on major and trace elements based on replicates is reported in brackets.

Sample	MH-19-024	MH-19-031	MH-19-055	MH-20-001	MH-20-008	MH-20-009	MH-20-014	MH-20-016	MH-20-020	MH-20-032	MH-20-039	MH-20-043	MH-20-045
UTM East	460484	460964	461014	460535	460462	460462	460539	460551	460554	460505	460653	460972	460972
UTM North	5599888	5599860	5599824	5599657	5599597	5599597	5599598	5599924	5599602	5599864	5599610	5599769	5599769
Facies Code	Ls	Ld2	Lp	Ld2	Ld1	Lpi	Lt1 (glass)	Ld1	Lt1 (glass)	Lpi	Ls	Ld2	Lp
Phenocrysts	Pl>Ol>Cpx	Pl>Ol>Cpx	Pl > Ol<Cpx	Pl > Ol<Cpx	Pl>Ol	Pl>Ol	Pl~Ol	Pl>Ol	Pl~Ol	Pl>Ol	Pl>Ol	Pl>Ol>Cpx	Pl>Ol>Cpx
SiO_2 (0.28)	49.13	50.16	49.97	49.76	49.66	48.80	48.41	48.62	48.17	49.68	49.10	50.37	49.91
TiO_2 (0.02)	1.49	1.33	1.46	1.51	1.49	1.56	1.54	1.41	1.50	1.55	1.43	1.57	1.38
Al_2O_3 (0.14)	15.19	15.23	15.34	15.33	15.40	15.06	15.05	15.54	15.25	15.24	14.93	15.63	15.83
Fe_2O_3[1]	-	2.01	2.25	2.13	2.82	-	-	2.81	-	-	2.41	-	-
FeO[2] (0.02)	12.04	9.01	9.00	9.41	9.03	13.27	13.34	9.14	13.36	12.93	9.12	11.74	11.88
MnO (0.02)	0.15	0.15	0.16	0.16	0.16	0.17	0.19	0.15	0.18	0.16	0.16	0.14	0.15
MgO (0.56)	8.31	9.11	8.72	8.78	8.77	8.91	9.21	9.23	9.40	8.41	9.42	7.91	8.31
CaO (0.08)	8.77	8.56	8.62	8.59	8.74	8.82	8.12	8.77	7.79	8.77	8.50	8.96	8.69
Na_2O (0.02)	2.98	3.18	3.05	3.22	3.14	3.11	2.96	3.27	2.85	3.20	3.11	3.23	3.10
K_2O (0.02)	0.71	0.64	0.80	0.67	0.60	0.64	0.57	0.31	0.41	0.62	0.50	0.50	0.73
Cr_2O_3 (0.02)	0.04	0.04	0.04	0.04	0.04	0.04	0.04	0.04	0.04	0.04	0.04	0.04	0.04
P_2O_5 (0.02)	0.24	0.24	0.24	0.25	0.24	0.29	0.28	0.25	0.24	0.26	0.24	0.25	0.23
Totals	99.05	99.66	99.65	99.85	100.09	100.67	99.71	99.54	99.19	100.86	98.96	100.34	100.25
LOI	-0.14	-0.31	-0.37	-0.49	-0.37	-0.41	0.82	-0.52	0.77	-0.32	-0.36	0.12	-0.25
Mg#[3]	62.99	64.32	63.33	62.45	63.39	62.35	63.00	64.29	63.44	61.47	64.80	62.43	63.30
FeO(T)*	12.04	12.02	12.25	12.59	12.86	13.27	13.34	12.97	13.36	12.93	12.55	11.74	11.88
La (0.8)	10.6	9.4	9.4	8.7	9.8	9.8	10.6	10.0	9.7	9.1	10.2	8.8	-
Ce (1.2)	21.3	20.8	19.8	20.5	20.1	21.3	21.4	19.1	21.4	19.5	20.0	18.7	-
Pr (0.08)	3.09	2.88	2.9	2.84	2.82	3.08	3.04	2.87	3.06	2.88	2.83	2.75	-
Nd (0.6)	14.1	12.8	13.5	12.9	13.8	13.9	14.5	13.4	14.5	13.2	13.9	13.1	-
Sm (0.16)	3.76	3.76	3.54	3.49	3.48	3.74	3.74	3.45	3.54	3.48	3.4	3.61	-
Zr (5)	92	91	88	96	87	95	107	89	102	94	88	95	-
Hf (0.24)	2.20	2.50	2.20	2.40	2.40	2.50	2.70	2.30	2.50	2.50	2.30	2.40	-
Eu (0.10)	1.39	1.37	1.29	1.30	1.27	1.32	1.35	1.27	1.28	1.34	1.27	1.35	-
Gd (0.08)	4.09	3.89	3.92	4.05	3.96	3.95	3.97	3.92	4.04	3.94	3.76	3.87	-
Tb (0.02)	0.67	0.63	0.63	0.61	0.59	0.61	0.61	0.58	0.59	0.59	0.60	0.60	-
Dy (0.12)	3.62	3.53	3.42	3.45	3.35	3.46	3.60	3.33	3.47	3.43	3.34	3.32	-
Y (0.9)	18.2	17.5	16.8	16.9	17.5	17.1	18.1	17.2	16.6	16.4	17.8	17.0	-
Ho (0.04)	0.73	0.67	0.69	0.66	0.69	0.66	0.70	0.62	0.65	0.65	0.69	0.61	-
Er (0.06)	2.00	1.78	1.81	1.75	1.82	1.83	1.79	1.76	1.74	1.71	1.71	1.77	-
Tm (0.02)	0.28	0.25	0.25	0.24	0.24	0.23	0.24	0.23	0.22	0.23	0.23	0.22	-
Yb (0.08)	1.62	1.47	1.48	1.53	1.38	1.50	1.51	1.46	1.49	1.41	1.33	1.37	-
Lu (0.02)	0.24	0.22	0.23	0.20	0.21	0.21	0.21	0.20	0.20	0.21	0.20	0.20	-

*FeO(T) is total iron oxide wt % reported from XRF analyses for all samples

[1]Fe_2O_3 calculated for samples with known FeO, where $Fe_2O_3 = (FeO(T) - FeO)/0.8998)$

[2]FeO determined separately through ferric titration for select samples

[3]Mg# computed as MgO/(MgO+FeO (mol. %). CM samples not measured with ferric titration use the mean value of $Fe^{2+}/\Sigma Fe = 0.7228$ (N=7) for CM basalts

Declaration of interests

☒ The authors declare that they have no known competing financial interests or personal relationships that could have appeared to influence the work reported in this paper.

☐The authors declare the following financial interests/personal relationships which may be considered as potential competing interests:

CRediT author statement

Martin Harris: Conceptualization, Investigation, Formal Analysis, Writing-Original Draft, Writing-Review and Editing, Visualization. **Kelly Russell:** Conceptualization, Writing-Review, and Editing, Supervision. **Rene Barendregt:** Formal Analysis, Resources, Writing-Review, and Editing. **Lucy A Porritt:** Resources, Writing-Review and Editing, Supervision. **Alex Wilson:** Writing-Review and Editing, Visualization.

Declaration of competing interest

The authors declare that they have no known competing financial interests or personal relationships that could have appeared to influence the work reported in this paper.

Data availability

Data will be made available upon request.

Explosive Glaciovolcanism at Cracked Mountain Volcano, Garibaldi Volcanic Belt, Canada

Martin A. Harris[1]

James K. Russell[1]

Rene Barendregt[2]

Lucy A. Porritt[1]

&

Alex Wilson[3]

[1]Volcanology and Petrology Laboratory, EOAS, University of British Columbia

[2]Department of Geography, University of Lethbridge

[3]Minerva Intelligence

Journal of Volcanology and Geothermal Research

Submitted September 8, 2021

Revised, January 10, 2022

Corresponding Author: Martin Harris: mharris@eoas.ubc.ca

Abstract

Cracked Mountain (CM) is a basaltic volcano within the northern extension of the Cascade volcanic arc into southwest, British Columbia, Canada (i.e. Garibaldi Volcanic Belt) and is dated at 401 ± 38 ka ($^{40}Ar/^{39}Ar$). The edifice covers an area of ~1.5 km^2 and has a volume of 0.18 km^3. The volcano features steep margins with local relief of ~250 m (1,650 m a.s.l), is dissected by abundant 0.5 to ~20 m wide extensional cracks with depths up to 30 m, and has a highly eroded top. The edifice is dominated by massive to poorly stratified, moderately to pervasively palagonitized lapilli tuffs, comprising vitric fine ash to lapilli. Juvenile pyroclasts have blocky to highly vesiculated shapes consistent with a phreatomagmatic (i.e. explosive) origin. The lapilli tuffs are intruded by and mingled with coherent to disaggregated lobes of peperitic pillowed lavas. Contacts between lapilli tuff and peperitic pillowed lava show soft-sediment deformation and in-situ quench-fragmentation indicating that the tephra was both unconsolidated and water-saturated at the time of intrusion. Local stacks of pillow lava are found on the margins of the edifice. More than fifty, 0.5 to 3 m wide dykes intrude CM stratigraphy and display, either, peperitic pillowed margins or sharp, chilled margins and columnar-jointing. Measurements of paleomagnetic directions (9 sites) were made for all CM lithofacies and record a single-pole direction indicating a single monogenetic eruption. A glaciovolcanic origin is strongly suggested by the abundant subaqueous lithofacies (i.e. palagonitized tephra, pillows, peperites) and the physiographic setting of the edifice which is well above any drainage that could sustain a standing body of water. The elevation of CM and depth of surrounding valleys indicate syn-eruptive confinement by a paleo-ice sheet that was ≥ 850 m thick. The edifice shape, size, and surrounding topography suggest a 'leaky' paleolake system capable of supporting ~0.36 km^3 of water. The glaciovolcanic origin and the absolute ($^{40}Ar/^{39}Ar$) age of CM represent an important record of the Cordilleran Ice sheet (CIS) in southwestern BC during the mid-Pleistocene.

Key Words: Glaciovolcanism, Subglacial, Phreatomagmatic, Basalt, Englacial Lake, Ice-Sheet

1. Introduction

The Garibaldi Volcanic Belt (GVB) is the northern segment of the Cascade Volcanic Arc (Roddick and Souther, 1987; Green et al., 1988; Hildreth, 2007). GVB volcanic deposits range from Pleistocene to Holocene in age and result from subduction of the Juan de Fuca plate beneath the North American Plate (Roddick and Souther, 1987; Green et al., 1988; Hildreth, 2007). Southwest British Columbia has a protracted history of multiple glaciations, with cycles of advancing and retreating cordilleran ice sheets throughout the Pleistocene (Clague, 2009; Clague and Ward, 2011). As a result, the GVB hosts numerous glaciovolcanic landforms. Prior studies concerning glaciovolcanism have focused on the Mount Garibaldi volcanic field (e.g., Mathews, 1952; Wilson et al., 2019), the Mount Cayley volcanic field (e.g., Kelman et al., 2002; Kelman, 2005), the Mount Meager volcanic complex (MMVC) (e.g., Wilson and Russell, 2017, 2018), the Salal Glacier volcanic complex (e.g., Lawrence et al., 1984; Wilson and Russell, 2018), and the Bridge River volcanic field (e.g., Roddick and Souther, 1987; Wilson and Russell, 2018).

Cracked Mountain is a basaltic volcano situated on the southern flank of the MMVC and originally identified by Read (1979) as part of the Mosaic Assemblage (i.e., undivided, Pleistocene aged, basalts within the MMVC). Here, we present a new dataset including a map of volcanic lithofacies, petrographic and geochemical characteristics of the deposits, geochronometric (^{40}Ar /^{39}Ar) age estimates, and paleomagnetic directions of all lithofacies. Collectively, these data inform on the physical volcanological evolution of the Cracked Mountain (CM) volcano. Our analysis shows CM to have a glaciovolcanic origin (Kelman et al., 2002; Smellie, 2007; Edwards et al., 2009) involving sustained eruption within an englacial lake. The lithofacies and their stratigraphic relationships indicate an explosive onset to the eruption dominated by phreatomagmatic activity that transitioned to effusive activity expressed by intrusions and lavas. We use the geometry of the CM edifice (i.e. shape and size) and the distribution of lithofacies to reconstruct the eruptive history of the glaciovolcanic edifice and to constrain the thickness and distribution of the enclosing ice sheet. Our findings contribute to a larger story of glaciovolcanism within the GVB and paleoclimate reconstructions for SW British Columbia.

2. Geological Background

The Mount Meager volcanic complex is situated 160 km north of Vancouver in SW British Columbia (Fig. 1) and is one of eight major centres and volcanic fields comprising the GVB (Fig. 1A). Recent GVB geochemical and petrological studies show increases in melt alkalinity and a decrease in slab-derived signatures moving northward in the GVB (Green and Sinha, 2004; Mullen and Weis, 2013). In particular, the MMVC, Salal Glacier volcanic complex, and Bridge River volcanic field show a heightened primitive signature compared to the southward GVB and the High Cascade volcanoes. These findings suggest that the Nootka Fault, located Northwest of the Bridge River cones (Fig.1A), may mark the terminus of the Juan de Fuca subduction where a window between the Juan de Fuca and Northward Explorer plate allows upwelling of asthenospheric melts under the northernmost GVB centres (Mullen and Weis, 2013).

The MMVC (Fig. 1B) contains Pleistocene to Holocene basalt to rhyolite overlying basement igneous and metamorphic rocks of the Coastal Plutonic complex (Fig 1B) (Woodsworth, 1977; Read, 1979; Green et al., 1988). The MMVC is also host to the youngest GVB eruptive deposits, namely the 2350 B.P. Pebble Creek formation (Hickson et al., 1999; Stewart et al., 2008). Intermediate to felsic lavas are dominant within the Mount Meager Massif, however, localized mafic centres are present in the north (Lillooet Ridge and River), west (Mosaic Ridge), and southwest (Cracked Mountain and Elaho Valley) regions of the volcanic complex (Fig. 1B) (Read, 1979, 1990; Harris and Russell, 2021). The ages of the Mosaic Ridge basalts and Elaho Valley basaltic andesites are ~90 and 140 ka respectively (Woodsworth, 1977; Green et al., 1988).

3. Cracked Mountain Physiography and Morphology

The Cracked Mountain volcano unconformably overlies basement granodiorite (Bg) and schist (Bs) of the Gambier and Cadwallader Groups respectively (Fig. 2A) (Read, 1979). The volcanic deposits form a slightly asymmetric, NE-SW trending ~250 m thick ridge that is ~1,300 m long and ~1,000 m wide covering an area of ~1.5 km^2 and having a present-day volume of ~0.18 km^3. The summit of CM rises to 1,650 m above sea level (a.s.l.) and the margins reach elevations as low as 1,250 m (Fig. 2A). CM is surrounded by steep valleys of the Meager Creek and Elaho River tributaries to the north and west respectively (Fig. 3). Extensional cracks dissect

the entirety of CM (Figs. 2A; 3B), ranging from 0.5 to > 20 m in width and up to 30 m in depth. The fractures form parallel clusters that commonly trend perpendicular to the downslope direction. All CM lithofacies are offset and displaced by cracks. No glacial deposits (i.e. till, erratics) are found within cracks, suggesting a post-eruptive and post-glacial origin.

The shape and surface features of CM show evidence of glacial enveloping and scouring. The present-day surface is littered with cobble to boulder-sized granitic erratics and some locations have been smoothed and striated in a SW direction. These findings show that post-eruption Cordilleran Ice Sheets have reached elevations greater than the summit of CM. The margins of CM are cliffs up to 40 m high, which is unusually thick for basaltic lava (e.g., Edwards et al., 2015). We interpret this morphology to be a result of syn-eruptive glacial confinement and subsequent erosion. There is no evidence of ice-abutment in the form of laterally facing, hackly, or irregular jointed lavas (e.g., Lescinsky and Fink, 2000; Kelman et al., 2002) suggesting that the outermost CM margins result from post-eruptive glacial erosion rather than reflecting primary lava-ice contact surfaces.

4. Volcanic Lithofacies

We recognize ten CM lithofacies (Table 1) that include, both, volcaniclastic and coherent lithofacies. All volcanic deposits are olivine and plagioclase porphyritic and differ only in their groundmass textures ranging from holocrystalline, hypocrystalline, and quenched. The terminology used to describe grain size and componentry of volcaniclastic rocks is after White and Houghton (2006).

4.1 Volcaniclastic

CM lapilli tuffs (Lt_{1-2}) (Table 1) form the stratigraphically lowest (Fig. 2B) lithofacies. Observed thicknesses range from 0.5 m to < 6 m. Lt_1 is massive, moderately- to poorly sorted, and is observed throughout the CM edifice from its base to its summit (Fig. 2; 4A). Lt_1 is composed of dense and blocky to highly vesiculated and cuspate vitric juveniles and contains 5-35% lapilli-sized clasts supported in a vitric ash matrix. Lt_1 is commonly intruded by dykes (Ld_{1-2}) and mingled with peperitic lobes (Lpi; Table 1) (Fig. 5). In some locations, soft-sediment deformation of Lt_1, in the form of squeeze-up pipes, is observed. Lt_2 outcrops in the SE and N sections of CM and, by comparison, are thinly bedded, well-sorted (Fig. 4B). Beds of ultra-fine

ash are up to 5 cm thick and dip shallowly in the downslope direction. In some outcrops, microfractures offset laminated beds, and truncated and shallow cross-beds are also observed. Lt_2 is commonly observed as 1-2 m layers within thicker, massive Lt_1 exposures (Fig. 2B; 4B) and displays fining upward grain sizes. Lt_3 are locally stratified as defined by accumulations of lapilli and bomb-sized, fluidal to blocky, vesiculated (<60%) spatter clasts (Fig. 4C). The clasts are supported by a well-sorted, vitric ash matrix. Two small outcrops of Lt_3 are located at upper elevations (i.e. high in stratigraphy) in the central and NE sections of the CM.

Peperite (Pi) deposits, as defined by White et al., (2000) and Skilling et al., (2002), are volcaniclastic deposits resulting from the mingling of magma with wet, unconsolidated sediments. At CM, peperites occur as fragmented, globular to blocky components of vitric basalt supported by ash and lapilli tuff matrix (Figs. 2B; 6). Peperite deposits are distributed along the margins of the peperitic intrusive bodies (Lpi). We distinguish lithofacies Pi from Lpi (Table 1) as volcaniclastic and coherent, respectively. The thickness of peperites varies from a few cm to 2-3 m away from the margins of Lpi. Peperites rarely outcrop at the present-day CM surface but are commonly exposed in cracks at all locations of the volcano.

Tuff breccias (Tb) blanket much of the topography in the central and north regions, are the dominant map unit (Fig. 2), and obscure stratigraphically older volcanic lithofacies. At higher elevations, tuff breccias form thin 1-2 m-thick deposits that progressively thicken (<10 m) downslope (Fig. 7). Tuff breccias are massive and clast-supported, featuring monolithic lapilli-to block-sized lithic components. These lithics are olivine-and-plagioclase porphyritic lava fragments of Lpi, Ls, and Lp, where ~30-40% show rounded chilled margins. Minor yellow ash-sized interstitial sediment is present between breccia clasts. Rarely, block and lapilli-sized, rounded Lt_1 lithics are present (Fig. 7B).

4.2 Coherent

The peperitic pillowed lava unit (Lpi) (Table 1) comprises coherent, mingled lavas that intrude volcaniclastic deposits (Lt) across all elevations and locations of the edifice (Fig. 2). Lpi is a mappable unit distinct from coherent pillow lavas (Lp; Table 1) formed through subaqueous effusion. The Lpi unit occurs where magma has been injected into water-saturated sediments and forms massive globular bodies up to 15-20 m across and 10-15 m high, comprising chilled, subrounded lobes (Fig. 5A and B). Additionally, Lpi is often associated with 'blooming' dykes

156 (Ld_1) (Fig. 5C) that transition from ~0.5-1 m wide intrusions into <5 m wide, "pillowed" masses.
157 Since Lpi intrudes and pillows into lapilli tuff (Lt) (i.e. host sediments) we interpret these
158 lithofacies to be 'peperitic' intrusions, after White and Houghton (2006).
159 Pillow lava deposits (Lp) (Table 1), makeup ~20% of the edifice, and are the dominant
160 lithofacies exposed at the edges of CM (Fig. 2). Pillow lava outcrops at the present-day, high
161 elevations of CM (Figs. 2A) as 1-3 m thick piles and increases to ~ 10-40 m thick along the cliffs
162 at the outer edges of the volcano (Figs. 2B; 8A and B). Individual pillows are bulbous, with
163 diameters up to 50 cm (Fig. 8C). Interstitial quench-fragmented vitric sediment fills void spaces
164 between intact pillows in some outcrops (Fig. 9A). Large radial columnar jointed pods up to 3 m
165 in diameter make up a lesser amount of the lithofacies. Stratigraphically, Lp is overlain by tuff
166 breccia (Tb), is cut by dykes (Ld_2), and is observed to overlie outcroppings of lapilli tuff (Lt_1) at
167 the base of the edifice (Fig. 2B).
168 Blocky and columnar jointed remnants of sheet lava (Ls) (Table 1) are preserved at the
169 highest elevations of CM near the central and eastern regions (Fig. 2A). Sheet lava outcrops are
170 small, ranging from ~10-30 m across, and 1-2.5 m thick. The sheet lavas have coarse columnar
171 joints up to 0.4 m in diameter and occur at the present-day surface of CM. The tops of the sheet
172 lavas are scoured by SW trending glacial striae and covered with erratics (Fig 8D).
173 Over 50 dykes (Ld_{1-2}) intrude the CM volcano (Fig 2A). The dykes are predominantly
174 subvertical and have widths ranging from 0.5 to 3 m in width and up to 100 m in length. The
175 dominant trends of the dykes strike E-NE and W-NW. Dykes were divided into two groups
176 based on their margins: 1) Ld_1 (Table 1) have poorly defined, glassy, pillowed, or peperitic
177 margins where they contact bodies of Lpi (Fig. 5C), and 2) Ld_2 (Table 1) have sharp, chilled, and
178 columnar jointed margins where they intrude all other lithofacies. Ld_1 is prevalent in the central
179 and high elevations of the edifice and is best exposed through extensional cracks. Ld_2 outcrop
180 sporadically in the central high elevations of CM, as well as, along the eastern margin of the
181 edifice where they intrude subvertically stacked piles of Lp.
182
183 **5. Lithofacies associations**
184 The topmost portion of CM edifice and uppermost stratigraphic units are heavily eroded
185 which precludes us from identifying the precise location and nature (e.g., fissure, cone, etc.) of
186 the vent. However, we expect that the vent was near the present-day summit (elev. ~1580 m)

where, within a 100 m radius, we find a multitude (~10) of cross-cutting dykes intersecting the upper surface of the edifice. The volcano is volumetrically dominated by subaqueous style lithofacies that result from and record an explosive onset to the eruption followed by effusion (e.g., pillow lava) and intrusion (e.g., dykes). Furthermore, rather than a simple layer-cake stratigraphy, the CM volcano grew: i) laterally where deposits source from higher elevations and extend to the margins of the edifice, and ii) endogenously by abundant intrusions within the volcaniclastic pile. Based on the detailed stratigraphic relationships described above, we define four main lithofacies associations (A-D) (Table 2).

Lithofacies association A comprises Lt_1, Lpi, and Ld_1 (Table 2). Lt_1 is intruded by Lpi and Ld_1 at all elevations of the edifice, including exposures at the base of CM (Figs. 2B; 5). Ld_1 is observed to be in genetic relation to Lpi (Fig. 5C). Lt_1 outcrops at all elevations of CM, and the deposits are pervasively palagonitized and lithified (Stroncik and Schmincke, 2002). The mingling of Lpi within Lt_1 and examples of soft-sediment deformation indicate that Lt_1 was saturated and unconsolidated at the time of intrusion. Additionally, the margins of Ld_1 are often poorly defined and pillowed, further suggesting a saturated slurry-like host rather than a cooled and lithified host at the time of intrusion. Lastly, Ld_1 is often seen tangential to 'blooming' Lpi, suggesting that these two intrusive bodies are temporally related. Further petrographic similarities (i.e. olivine and plagioclase phenocrysts) substantiate a co-genetic relationship between Lpi and Ld_1. This lithofacies association reveals that unconsolidated ash and lapilli were intruded by peperitic bodies, processes that require a water-saturated eruptive environment. These stratigraphic relations imply an age succession of $Lt_1 > Lpi \geq Ld_1$.

Lithofacies association B comprises Lpi and Pi (Table 2); at CM peperite deposits (Pi) are always spatially associated with masses of intrusive pillow lava (i.e. Lpi; Fig. 6). We interpret these occurrences as fuel-coolant interactions (FCI) where the sudden contact of hot magma (e.g., fuel) with cold, saturated sediment (e.g., coolant) generates a vapour film around the intruding body (i.e. Lpi) (Doyle, 2000; Hooten and Ort, 2002; Martin and Németh, 2007). Within the vapour films, instabilities may arise, causing local phreatomagmatic fragmentation along the borders of the intrusion. Regions that experienced more stable vapour films result in globular peperite texture (Fig. 6C) while areas with less film stability produce blocky peperite textures (Figs. 6D) (Martin and Németh, 2007). Most peperite deposits form along the margins

of syn-volcanic intrusions. The field relations for Lpi and Pi show a contemporaneous origin, with both lithofacies forming as a result of intrusion into wet, unconsolidated lapilli tuffs.

Lithofacies association C comprises Tb, Ls, Lp, Lpi, and Lt (Table 2). The tuff breccia (Tb) blankets the upper surface of CM and contains a large proportion (<50%) of sheet lava (Ls) lithics, as well as moderate (30-40%) subrounded lithics of pillowed lava (Lp and Lpi), and minor (>5%) subrounded blocks of Lt (Fig 7). The high volume of Ls lithics entrained within the widespread tuff breccias is our best line of evidence that the sheet lavas preserved at higher elevations were originally more extensive and volumetrically abundant. Post-eruptive erosion (i.e. glacier erratics and scour marks; Fig. 8D) and collapse (i.e. extensive network of extensional fissures) provide a reasonable explanation for the relatively small remnant outcroppings of the Ls unit. The Tb matrix comprises moderately palagonitized, explosively derived fine ash, quench fragmented ash and lapilli, and coherent lapilli lithics. These findings suggest that Tb are syn-eruptive debris flows composed of previously erupted volcanic lithics. The degree of palagonitization alteration throughout the unit suggests subaqueous deposition (Schiffman et al., 2006). The tuff breccias incorporate clasts derived from all other earlier stratigraphic units which, combined with other stratigraphic relationships, suggests the succession Lt>Lpi≥Lp>Ls>Tb.

Lithofacies association D comprises Ld_2 with all other CM lithofacies (Table 2). At CM, Ld_2 intrudes through all other lithofacies with sharp, columnar jointed margins, including cross-cutting Ld_1 in select locations. These contact relations indicate that Ld_2 is the latest preserved lithofacies from the CM eruption. This last association suggests a temporal succession of $Lt>Lpi=Pi\geq Ld_1\geq Lp>Ls\geq Tb>Ld_2$.

6. Chemistry and Petrography

6.1 Petrography

Detailed mineral abundances and componentry based on standard polarizing light and scanning electron microscopy (Philips XL30) for all CM volcanic lithofacies are listed in Table 1. All coherent CM samples are olivine and plagioclase porphyritic, with glomeroporphyritic clots visible in hand samples. A smaller population of samples also contains phenocrystic augite. Petrographically, the pillowed dykes (Ld_1) have similar mineralogy as found in pillowed (Lpi) and most sheet lavas (Ls). Jointed-dykes (Ld_2) commonly contain phenocrystic augite as do a

small proportion of pillow lava samples (Lp). Olivine phenocrysts are subhedral and unzoned. Plagioclase phenocrysts are tabular and moderately zoned, with a very minor percentage (>5%) showing sieve textures. When present, augite crystals are subhedral to anhedral.

Volcaniclastic samples are distinguished by sorting, grain size, structures, and componentry. Lapilli tuffs (Lt_{1-3}) are composed of monolithic vitric juvenile fine ash and coarse lapilli (Figs. 9B-H) and microlitic tachylyte juvenile pyroclasts (5-30%). Intact to fragmented crystals of olivine and plagioclase are observed within the matrix of Lt_{1-3}. Juvenile shapes range from blocky to highly vesicular (~60-70%) (Figs. 9B-H). Interstitial sediments are observed between coherent Lp clasts but are notably different (i.e. coarse, jig-saw fit clasts compared with Lt_{1-3})(e.g. Fig 9A).

Tuff breccia (Tb) componentry is highly variable. Tb is dominated by clasts of basalt (Lpi, Ls, Lp) and contains minor blocks of Lt_1 within a matrix of vitric ash and lapilli. Tb matrix is overall coarser than Lt_{1-3} although still contains abundant blocky and highly vesiculated juveniles.

6.2 Geochemistry

Whole-rock major and trace element geochemical compositions were measured for 26 samples by X-ray fluorescence (XRF) analyses of fused discs and by inductively coupled plasma-mass spectroscopy (ICP-MS), respectively. Samples span all CM volcanic lithofacies (i.e. dykes, sheet and pillow lavas, and juvenile vitric-lapilli). Representative compositions of whole rocks and glasses are reported in Table 3; analytical uncertainties are based on replicate analyses done by Acme Analytical Labs Ltd., Vancouver, BC, Canada. A subset of samples was analysed for FeO volumetrically by ALS Canada Ltd., North Vancouver, BC, Canada. Appendix A contains the full data set and additional analytical details.

Figure 10A illustrates the chemical diversity of CM samples after Le Bas et. al, 1986 classification of volcanic rocks. All CM samples are subalkaline (Irvine and Baragar, 1971) but display moderate spread in SiO_2 (~47-51 wt.%) and Na_2O-K_2O (~3-4 wt. %). The spread in chemistry observed in Fig. 10A correlates with groups of samples having different phenocryst contents. Samples that contain minor modal abundances of augite (in addition to olivine and plagioclase) are typically higher in SiO_2 and Na_2O-K_2O wt. %. However, we find no significant differences in mineralogy or chemical compositions that correlate with the stratigraphic position.

279 Fig 10B shows Mg#s (molar MgO/ (MgO +FeO*)∗100) of CM samples with relation to
280 SiO_2 wt.%. Within the Cascade arc, volcanic rocks having Mg# > 60 are considered "primitive"
281 indicating limited crustal influence (Green and Harry, 1999; Mullen and Weis, 2013). Our results
282 show CM samples range from Mg# ~55-67 with the majority of samples (~80%) between 60-66.
283 Cracked Mountain rare earth elements (REE) shown in Fig. 10C normalized to chondrite
284 composition after Sun and McDonough (1989). There is little variation in trace element
285 concentrations between samples, including similar anomalies (i.e. positive Eu^{2+}), suggesting a
286 similar mantle source for all CM deposits.
287
288 **7. Geochronometry**
289 7.1 Radiogenic $^{40}Ar/^{39}Ar$ Results
290 Two CM samples (MH-19-055, 031) were selected for $^{40}Ar/^{39}Ar$ radiometric dating at
291 the WiscAr Geochronology Labs, University of Wisconsin-Madison, USA. The holocrystalline
292 dyke sample (MH-19-031) proved to be non-measurable because of excess argon trapped in the
293 plagioclase minerals. This is a common issue with basaltic dykes (of young ages) (Brian Jicha,
294 pers. comm. 2021) and with subglacially erupted deposits of all compositions (Clay et al., 2015).
295 The second CM sample (MH-19-055) was collected from the radially jointed interior of a pillow
296 lava outcrop. This sample contained low radiogenic argon but the analysis was still possible
297 through twenty-four heating steps with moderate uncertainty. The results yielded a plateau age of
298 401.6 ± 38.1 ka for crystallization of the groundmass (Fig. B1). Errors are quoted at a 2σ (95%
299 confidence) level and are propagated from all sources except for mass spectrometer sensitivity
300 and the age of the flux monitor. Appendix B contains analytical procedures used and table B1
301 contains complete measured data for heating steps.
302
303 7.2 Paleomagnetic Methods and Results
304 A total of nine sites across the CM edifice were selected for the paleomagnetic study. The
305 sites were chosen to span the entire stratigraphic sequence (i.e. oldest to youngest) and one site
306 (Site 2) was replicated for field and lab reproducibility (Table C1). We preferentially sampled
307 units that cooled quickly, thus locking in the geomagnetic field orientation at the time of
308 emplacement (e.g., Johnson et al., 2008). Efforts were made to sample only intact outcrops
309 thereby avoiding areas suspected of post-emplacement movement. Approximately eight standard

2.5-cm-diameter paleomagnetic cores were collected from each site and a minimum of three cores from each outcrop. Each sample was oriented using a magnetic compass, and where possible a sun compass was used in conjunction with magnetic orientations.

CM samples were analyzed at the paleomagnetic laboratory at the University of Lethbridge, Alberta. Magnetic susceptibility was determined with a Sapphire Instruments (SI-2B) susceptibility meter. The magnetization of each sample was measured with an AGICO JR-6A spinner magnetometer before demagnetization and again after each level of stepwise demagnetization. CM samples were held in magnetic shields following field collection and between laboratory measurements. All samples were subjected to alternating field (AF) demagnetization, performed using an ASC Scientific D-2000 demagnetizer with a three-axis manual tumbler, and carried out at 10 milli-tesla (mT) steps (up to 200 mT). Thermal demagnetization was carried out at 100, 200, 300, 400, 500, 525, 550, and 580 °C, using an ASC Model TD48 dual-chamber thermal demagnetizer to confirm that alternating field demagnetization was sufficient to resolve the primary remanence. Directions of characteristic magnetization were determined for each sample by principal component analysis (Kirschvink, 1980) using Remasoft version 3.0 (Chadima and Hrouda, 2006). Mean directions of characteristic magnetization were calculated for each site and an overall mean was also calculated (Appendix C; Table C1). All samples were subject to stepwise AF demagnetization and principal component analysis and mean directions were calculated from the AF data only.

All paleomagnetic samples are normally magnetized (Fig. 11A; Table C1). The mean directions of sites are consistent for eight of nine sites, where all eight sites plot within the uncertainty circle (α_{95}) about the overall mean (N=8) with a declination of 347.3˚ and inclination of 76.6˚, and Fisher precision factor of $k = 351$, $\alpha_{95} = 3.0°$ (Fig. 11A). Typical, well-behaved demagnetization characteristics are shown for samples from Lt_1 and Ld_1 respectively in Figs 11B and C.

All paleomagnetic samples produced stable directions of magnetization following stepwise demagnetization. Alternating field demagnetization, applied to all specimens, exhibited linear decay to the origin on orthogonal projections (Fig. 11B and C). The median destructive fields range from 20–80 mT and final directions are often stable up to 200 mT alternating field demagnetization (see CMV015A, Fig. 11B) indicative of single-domain magnetite. Thermal demagnetization showed complete demagnetization at 550 to 580 °C, typical of fine-grained

(single domain) magnetite as the magnetic carrier (see CMV029, Fig. 11C). Note that single-domain magnetite is the optimal magnetic mineral and grain size for producing reliable paleomagnetic directions. The magnetic susceptibility values of CM volcanics range from 0.4-1.0 x 10-3 SI (median value of 0.5 x 10-3 SI) for the flows composed of pyroclastic density currents and 2.4-16.4 x 10-3 SI (median value of 4.5 x10-3 SI) for dykes. Mean natural remanent magnetization for CM volcanics is 9.4 A/m (range 0.4–22.0 A/m).

The common pole direction obtained for all volcanic units, including the latest dykes, implies a common eruption age indicating a monogenetic origin for the volcano. Furthermore, the data from each site showed no indication of rotation or tilt as the mean direction is within the expected paleosecular variation (see mean of sites 2-9 and GAD inclination for sampling latitude, Fig. 11A, and Table C1). The sole exception was Site 1 (Table C1) where the seven cores record a different mean pole direction compared to the other eight sites (2-9). Site 1 is a lower elevation cliff-side exposure of pillow lava (Lp) on the SE margin of the edifice. Of the seven cores, three can be ascribed to post-emplacement rotation and yield coherent results with a mean declination and inclination of 34.4˚ and 72.9 respectively. The rotation is likely due to partial extensional collapse and, relative to the mean pole direction for the CM edifice, we calculate a downslope rotation of ~12˚E (Fig. C1). This rotation has a calculated maximum crack width of ~20 m which accords well with the observed fissures found on the outer margins of CM (e.g., Fig. 3B).

8. Discussion

8.1 Explosive Onset to Glaciovolcanic Eruption

The lapilli tuff deposits (e.g. Fig 9B-H) comprise coarse to fine ash (>100 μm) particles that are commonly highly vesiculated (<60%). The abundance of fine ash in CM Lt deposits suggests explosive magmatic and/or phreatomagmatic fragmentation (Zimanowski et al., 1991; White and Valentine, 2016; Latutrie and Ross, 2020). The Lt deposits comprise both blocky ash (e.g. Fig 9B) and micro-vesiculated cuspate ash (e.g. Fig 9D and F) suggesting that both phreatomagmatic (external water) and magmatic (internal volatiles) drove the explosive fragmentation processes. We note that blocky juveniles are dominant in $Lt_{1\text{-}3}$ suggesting that phreatomagmatic reactions involving glacial meltwater played the largest role in the explosive eruptive style.

372 Based on the overall bedform and textures found in Lt deposits, we assert that the
373 depositional environment was wet and probably (shallow) subaqueous. The massive character
374 and moderate to poor sorting of Lt_1 suggest continuous deposition from a sustained column,
375 rather than periodic explosive pulses which would generate moderately sorted and bedded
376 deposits via elutriation (e.g., White, 1996, 2000). The lack of welding, compaction, or clast
377 imbrication is also consistent with a water-rich intergranular phase (rather than gas) for these
378 pyroclastic density currents (White, 2000; Brand and Clarke, 2009).
379 The thinly bedded, moderate to well sorted, and weakly normally graded Lt_2 is indicative
380 of deposition from dilute pyroclastic density currents (i.e. pyroclastic surge; Fisher and Waters,
381 1970; Brand and Clarke, 2009). These deposits reflect phreatomagmatic explosive pulses that
382 dispersed highly fragmented ash laterally and elutriated through the water column. The shallow
383 dipping cross-bedding preserved in some Lt_2 outcrops (Fig. 4B) is consistent with subaqueous
384 pyroclastic deposits (Moorhouse and White, 2016). The overall lack of well-sorted beds of fine
385 ash, characteristic of thick water column elutriation, makes a shallow subaqueous setting most
386 plausible.
387 Lt_3 contains moderate volumes (20-40 %) of non-welded spatter within moderately to
388 well-sorted ash and lapilli matrix (Fig. 4C). We propose that the Lt_3 deposits record periods of
389 increased magma flux, volatility, and/or a decreased water supply (at the vent), where a
390 strombolian style burst ejected largely vesiculated and fluidal clasts (Latutrie and Ross, 2020).
391 We find that the overall characteristics of the Lt_3 deposits indicate a shallow aqueous to
392 emergent depositional environment. This assertion is based on a lack of bomb sags within these
393 deposits and chilled but not quenched (or pillowed) spatter clasts. The two outcrops of Lt_3 are
394 located at upper elevations of CM, and not observed within lower to middle stratigraphy. Our
395 interpretation is Lt_3 represents localized magmatic generated fallout mixed with
396 phreatomagmatically generated pyroclastic density currents in shallow aqueous to locally drained
397 regions of CM.
398 Explosively derived Lt deposits are present at all elevations of CM (Fig. 2) and comprise
399 ~30% of the entire edifice (Table 1), and excluding intrusions, are closer to 60% of the volcano
400 volume. Our findings indicate that not only was the onset of the CM eruptions explosive but that
401 explosivity was sustained throughout most of the eruption. This explosive-styled eruption makes
402 CM unique within the GVB, being only one of five other identified tephra-dominated

glaciovolcanic landforms (Wilson and Russell, 2018). We speculate that explosive onsets to glaciovolcanic eruptions may be significantly more common than recognized and underestimated because tephra-dominated landforms are highly susceptible to erosion. We suggest CM's transitional eruptive history, which produced intrusive and effusive coherent lavas, helped create a stronger structure more resistant to glacial erosion.

The investigation of Cracked Mountain deposits records a complex sequence of events beyond the initially explosive onset. Our analysis suggests the following conceptual model for the evolution of the CM eruption (Fig. 12):

1. An explosive, Surtseyan phase dominated the initial CM eruption, producing a subaqueous tephra cone comprising Lt_1 (Fig. 12A). Our interpretation of this initial phase is detailed above.
2. A transition from explosive to effusive (and intrusive) activity (Fig. 12B) is expressed by peperitic dykes (Ld_1) and bodies (Lpi). These intrusions inflate the edifice endogenously and dykes that pierce the margins of the tephra pile form stacks of pillow lavas (Lp) at the margins of the volcano.
3. Late-stage intrusions and effusions produce effusive lavas (Ls) and dykes (Ld_2) and associated breccias (Tb), (Fig. 12C). The culmination of the CM eruption is marked by late-stage dyke activity (Ld_2) that cut through all other lithofacies. The paleomagnetic signatures of all CM deposits overlap within one paleomagnetic moment. Thus, the CM eruption taking place from stages 1-3 can be thought of as more or less continuous.

The final stage (4) in the CM formation was non-eruptive and characterized by glacial erosion and edifice collapse (Fig. 12D). The timing of glacial retreat is unclear, but the present-day surface features bedrock erratics and scour marks indicating post-eruptive glaciation. The widespread distribution of large extensional fissures and cracks results from the retreat of the enclosing ice sheet which originally buttressed the steep-walled edifice. Glacial erratics are not found within these fissures which may suggest that the edifice was mainly enclosed (and buttressed) by regional and local ice until the Last Glacial Period (i.e. <115 -120 ka).

8.2 Paleoenvironmental implications

Our mapping and analysis suggest CM is a monogenetic edifice with no evidence for significant time gaps during the eruption. The results of paleomagnetic analyses concur with our field observations that the varying lithofacies were emplaced in one paleomagnetic moment ($\lesssim$ 1,000 years; Turner, 1987; Barletta et al., 2010; Lisé-Pronovost et al., 2013) at 401 ± 38 ka (Fig. B1).

The CM lithofacies (i.e. pillow lavas, palagonitized tuffs, and peperites) indicate a subaqueous eruptive paleoenvironment, however, the edifice is situated at a high elevation in a high relief environment and surrounded by steep-sided deep (~800 m) valleys (Fig. 3). We suggest a glaciovolcanic eruption into a sustained englacial lake of meltwater enclosed by a substantial ice sheet on the basis that there are no obvious physical barriers (i.e. mountains or ridges) to allow for a conventional paleo-lake. The volcanic lithofacies suggest that the englacial lake was sustained throughout the eruption and that the lake surface elevation continued to rise with the growth of the edifice. The CM volcano is best described as a transitional, tephra-dominated, tuya after the descriptive classification of Russell et al., (2014) and its lithofacies associations make it distinct from the classical mafic tuya model (e.g., pillow effusion, hyaloclastites, lava-fed deltas, and capping lava) (Smellie, 2007; Jakobsson and Gudmundsson, 2008; Edwards et al., 2015).

The CM volcanic succession is ~250 m thick and rests on basement rocks at ~1,250 m a.s.l (Fig. 2A). Subaqueous lithofacies outcrop at elevations as high as ~1,650 m a.s.l where they have relief of ~800 m above the major drainages. At the highest elevations of CM (~1,600-1650 m a.s.l), we find small remnant subaerial sheet lavas (Ls) although the abundance of Ls lithics within the thick succession of Tb deposits may suggest that there was much more subaerial lava originally. There are, at least, two scenarios that would explain subaerial capping lavas within the englacial lake environment. The most likely scenarios are that, either, i) the edifice grew and became emergent above the paleolake level to form a classic passage zone defining a maximum lake level (Jones, 1970; Smellie, 2006; Russell et al., 2013; Edwards et al., 2015) or ii) the level of the englacial lake decreased due to subglacial drainage creating a "dry" subaerial environment. In the latter case, post-draining subaerial lavas overlapping the subaqueous lithofacies establish a minimum level of the englacial lake (Smellie, 2006; Skilling, 2009; Russell et al., 2013).

462 There is no direct evidence for a passage zone relationship (i.e. beds of pillow lava
463 breccias or lava fed deltas) so we favour the second scenario involving overlap lavas wherein the
464 elevation of Ls at ~1,650 m defines a minimum level and, thus, a minimum depth of ~250 m for
465 the paleo-englacial lake (Fig 13B). We have used the shape and size of the CM edifice and the
466 surrounding topography to constrain the maximum dimensions and volume of the paleo-
467 englacial lake. The paleo-topography beneath the CM edifice (Figs. 3, 13A) limits the size of the
468 syn-eruptive englacial lake. Relative to the present-day edifice we estimate the lake may have
469 extended <100 m to the south and <300 m to the east but been limited to < 50 m to the north and
470 west by very steep drainages. Assuming an asymmetric shape of 1,800 m long and 1,300 m wide
471 and a maximum depth of 250 m (Fig. 13B) yields a maximum lake volume at ~0.36 km^3. The
472 present-day (i.e. minimum) volume of the CM volcano is ~0.18 km^3 such that the lake could
473 only store < 0.18 km^3 of water (i.e. maximum lake volume – edifice volume). This strongly
474 suggests that throughout the eruption the englacial lake was never fully sealed but was a leaky
475 system where meltwater production and sub-ice drainage were nearly matched (cf. Russell et al.
476 2014). As the eruption waned, melting of the enclosing ice became less efficient and drainage
477 became dominant, leading to a lowering of the lake level to allow for subaerial eruption of lavas
478 (Fig. 12C).
479 To sustain a lake level of 250 m requires a rate of leakage less than the rate of meltwater
480 accumulation and also requires an ice thickness above ~280-300 m to counterbalance the
481 hydrostatic lake pressure (e.g., Tweed and Russell, 1999; Smellie, 2006; Edwards et al., 2015).
482 The surrounding topography features steep drainages with valley floors at ~ 800 m a.s.l. (i.e.
483 Meager Creek and Elaho valley; Figs. 3 and 13). This suggests that the enclosing ice sheet, an
484 earlier (paleo-) incarnation of the Cordilleran Ice Sheet (CIS) at 401 ± 38 ka, was at least 880 m
485 thick. This minimum ice thickness has implications for the distribution of the paleo-CIS and
486 suggests that most of the surrounding landscape was under ice except at the highest elevations
487 (Fig. 13A and C; Clague, 2009; Wilson et al., 2020).
488 The CM age of 401 ± 38 ka coincides with the waning of marine $\delta^{18}O$ isotope stage
489 (MIS) 12 glacial period (~470-425 ka) and the warming period of MIS 11 (~420-375 ka)
490 (Lisiecki and Raymo, 2005) (Fig. 14). The shift in global $\delta^{18}O$ associated with the MIS 12 to 11
491 transition is the largest of all the Pleistocene cycles and signifies rapid global warming (e.g. Fig
492 14; Lisiecki and Raymo, 2005). The ~850 m (or thicker) thickness of the paleo-CIS enclosing the

493 Cracked Mountain volcano is inconsistent with the mid-point of MIS 11 at 400 ka. However, if
494 we accept a slightly older $^{40}Ar/^{39}Ar$ age of ~425 ka (still within the analytical uncertainty)
495 (Table B1) for the eruption of Cracked Mountain, the age accords well with the global ice period
496 MIS 12 (Lisiecki and Raymo, 2005; Batchelor et al., 2019). Eruption ages for other volcanoes in
497 the GVB are sparse, however, Wilson and Russell (2018) report glaciovolcanic eruptions during
498 MIS 12 within the Mount Cayley volcanic field (Ember Ridge, unpublished age), as well as,
499 subaerial lavas erupting in the Salal glacier field during MIS 11 (Nichols Valley at 405 ka).
500 These additional age constraints, although limited, do support the eruption of Cracked Mountain
501 into an early (late-Pleistocene) incarnation of the CIS within SW British Columbia at ~ 425 ka.
502 We also speculate that at this time, there may have been a large-scale decompression
503 effect on the Earth's crust driven by rapid deglaciation at the end of MIS 12. The link between
504 volcanism and crustal unloading during periods of deglaciation has been modeled throughout the
505 GVB (e.g., Wilson and Russell, 2020) and explored in Icelandic and Andean glaciovolcanic
506 fields (e.g., Carrivick et al., 2009; Guillot and Ponce, 2021). We, therefore, find it entirely
507 feasible that the CIS retreat in SW British Columbia would have triggered magmatic ascent
508 through the unloaded crust, leading to the eruption of the Cracked Mountain volcano (as well as
509 others). Lastly, since records of older glaciation cycles tend to be obscured by younger waxing
510 and waning of ice sheets, our findings at CM provide useful temporal and physical constraints
511 for the CIS extent in SW British Columbia during the mid-Pleistocene.
512
513 **9. Summary**
514 The Garibaldi Volcanic Belt contains many Quaternary glaciovolcanic centres. The study of
515 these volcanoes provides paleoclimatic evidence at the time of the eruptions and contributes to
516 the understanding of magma, ice, and water interactions more generally. Here, we present the
517 first physical volcanological study of Cracked Mountain, a transitional, tephra-dominated tuya.
518 Our findings indicate an initially explosive eruption that later transitioned into intrusive and
519 effusive activity. We characterize the explosivity as dominantly phreatomagmatic, manifested as
520 Surtseyan style eruption in a shallow englacial lake. Peperitic intrusions and pillow lava
521 effusions are the largest coherent units by volume, indicating that subaqueous conditions
522 persisted through the middle and later stages of the eruption. Small remnants of subaerially
523 erupted lavas are preserved at the highest elevations, suggesting that the lake drained periodically

524 in the later stages of the eruption. This claim is supported by our modeling of paleolake
525 dimensions and volumetric capacities. Lastly, our temporal investigation of the eruption
526 concludes that CM was monogenetic, erupting ~425 ka between MIS 11 and 12. We model the
527 localized, mid-Pleistocene CIS as having a minimum thickness of ~850 m, reaching elevations of
528 1,680 m a.s.l or higher.
529
530
531 **Acknowledgments**
532 This research was supported by the Geological Survey of Canada with funding through NRCan's
533 Emerging Renewable Power Program and GeoScience BC. Special thanks to Steve Grasby of
534 NRCan for all his help organizing field campaigns and funding analytical methods. We thank
535 Sophie Leiter, Lindsey Abdale, Annie Borch, and Mahmud Mohammad for their assistance in
536 the field.
537
538 **References**
539 Barletta, F., St-onge, G., Channell, J.E.T., and Rochon, A., 2010, Dating of Holocene western
540 Canadian Arctic sediments by matching paleomagnetic secular variation to a geomagnetic
541 field model: Quaternary Science Reviews, v. 29, p. 2315–2324,
542 doi:10.1016/j.quascirev.2010.05.035.
543 Le Bas, M.J., Le Maitre, R.W., Streckeisen, A., and Zanettin, B., 1986, A chemical classification
544 of volcanic rocks based on the total alkali-silica diagram: Journal of Petrology, v. 27, p.
545 745–750, doi:10.1093/petrology/27.3.745.
546 Batchelor, C.L., Margold, M., Krapp, M., Murton, D.K., Dalton, A.S., Gibbard, P.L., Stokes,
547 C.R., Murton, J.B., and Manica, A., 2019, The configuration of Northern Hemisphere ice
548 sheets through the Quaternary: Nature Communications, v. 10, doi:10.1038/s41467-019-
549 11601-2.
550 Brand, B.D., and Clarke, A.B., 2009, The architecture, eruptive history, and evolution of the
551 Table Rock Complex, Oregon: From a Surtseyan to an energetic maar eruption: Journal of
552 Volcanology and Geothermal Research, v. 180, p. 203–224,
553 doi:10.1016/j.jvolgeores.2008.10.011.
554 Carrivick, J.L., Russell, A.J., Rushmer, E.L., Tweed, F.S., Marren, P.M., Deeming, H., and

555 Lowe, O.J., 2009, Geomorphological evidence towards a de-glacial control on volcanism:
556 Earth Surface Processes and Landforms, v. 1178, p. 1164–1178, doi:10.1002/esp.
557 Chadima and Hrouda, 2006, Remasoft 3.0: A user-friendly paleomagnetic data browser and
558 analyzer: Travaux Géophysiques, v. XXVII, p. 20–21.
559 Clague, J.J., 2009, Cordilleran Ice Sheet: Encyclopedia of Paleoclimatology and Ancient
560 Environments, p. 206–211.
561 Clague, J.J., and Ward, B., 2011, Pleistocene Glaciation of British Columbia: Elsevier Inc., v. 15,
562 563–573 p., doi:10.1016/B978-0-444-53447-7.00044-1.
563 Clay, P.L., Busemann, H., Sherlock, S.C., Barry, T.L., Kelley, S.P., and McGarvie, D.W., 2015,
564 40Ar/39Ar ages and residual volatile contents in degassed subaerial and subglacial glassy
565 volcanic rocks from Iceland: Chemical Geology, v. 403, p. 99–110,
566 doi:10.1016/j.chemgeo.2015.02.041.
567 Doyle, M.G., 2000, Clast shape and textural associations in peperite as a guide to
568 hydromagmatic interactions: Upper Permian basaltic and basaltic andesite examples from
569 Kiama, Australia: Australian Journal of Earth Sciences, v. 47, p. 167–177,
570 doi:10.1046/j.1440-0952.2000.00773.x.
571 Edwards, B.R., Gudmundsson, M.T., and Russell, J.K., 2015, Glaciovolcanism: The
572 Encyclopedia of Volcanoes, p. 377–393, doi:10.1016/b978-0-12-385938-9.00020-1.
573 Edwards, B.R., Skilling, I.P., and Tuffen, H., 2009, Volcano-Ice Interactions on Earth and Mars:
574 Journal of Volcanology and Geothermal Research, v. 185, p. 247–250.
575 Fisher, R. V, and Waters, A.C., 1970, Base surge bed forms in Maar volcanoes: American
576 Journal of Science, v. 268, p. 157–180.
577 Green, N.L., Harakal, J.E., Souther, I.J.G., and Read, P.B., 1988, Eruptive history and K-Ar
578 geochronology of the late Cenozoic Garibaldi volcanic belt, southwestern British Columbia:
579 Geological Society of America Bulletin, v. 100, p. 563–579,
580 https://pubs.geoscienceworld.org/gsa/gsabulletin/article-pdf/100/4/563/3380343/i0016-
581 7606-100-4-563.pdf.
582 Green, N.L., and Harry, D.L., 1999, On the relationship between subducted slab age and arc
583 basalt petrogenesis, Cascadia subduction system, North America: Earth and Planetary
584 Science Letters, v. 171, p. 367–381, doi:10.1016/S0012-821X(99)00159-4.
585 Green, N.L., and Sinha, A.K., 2004, Consequences of varied slab age and thermal structure on

586 enrichment processes in the sub-arc mantle of the northern Cascadia subduction system:
587 Journal of volcanology and geothermal research, v. 140, p. 107–132.
588 Guillot, M.G., and Ponce, J.F., 2021, Change of eruptive style during Pliocene deglaciation :
589 from scoria cones to lava shields in southern extra - Andean Patagonia , Argentina:
590 Bulletin of Volcanology, p. 1–19, doi:10.1007/s00445-021-01466-z.
591 Harris, M., and Russell, J.K., 2021, Bedrock Mapping Results for the Mount Meager Geothermal
592 Research Initiative: Geoscience BC, p. 7–34.
593 Hickson, C.J., Russell, J.K., Stasiuk, M. V, and Swanson, D.A., 1999, Volcanology of the 2350
594 B.P. Eruption of Mount Meager Volcanic Complex, British Columbia, Canada: implications
595 for Hazards from Eruptions in Topographically Complex Terrain 1: Bulletin of
596 Volcanology, v. 60, p. 489–507.
597 Hildreth, W., 2007, Quaternary Magmatism in the Cascades-Geologic Perspectives: U.S
598 Geological Survey, v. 1744, p. 1–123.
599 Hooten, J.A., and Ort, M.H., 2002, Peperite as a record of early-stage phreatomagmatic
600 fragmentation processes: An example from the Hopi Buttes volcanic field, Navajo Nation,
601 Arizona, USA: Journal of Volcanology and Geothermal Research, v. 114, p. 95–106,
602 doi:10.1016/S0377-0273(01)00282-7.
603 Irvine, T.N., and Baragar, W.R.A., 1971, A Guide to the Chemical Classification of the Common
604 Volcanic Rocks: Canadian Journal of Earth Sciences, v. 8, p. 523–548, doi:10.1139/e71-
605 055.
606 Jakobsson, S., and Gudmundsson, M., 2008, Subglacial and intraglacial volcanic formations in
607 Iceland: Jökull, v. 58, p. 179–196.
608 Johnson, C.L. et al., 2008, Recent investigations of the 0-5 Ma geomagnetic field recorded by
609 lava flows: Geochemistry, Geophysics, Geosystems, v. 9, doi:10.1029/2007GC001696.
610 Jones, T.G., 1970, Intraglacial Volcanoes of the Laurgarvatn Region, Southwest Iceland, II:
611 Journal of Geology, v. 78, p. 127–140.
612 Kelman, M.C., 2005, Glaciovolcanism at the Mount Cayley Volcanic Field, Garibaldi Volcanic
613 Belt, Southwestern British Columbia: University of British Columbia, 1–258 p.
614 Kelman, M.C., Russell, J.K., and Hickson, C.J., 2002, Effusive intermediate glaciovolcanism in
615 the Garibaldi Volcanic Belt, southwestern British Columbia, Canada: Geological Society,
616 London, Special Publications, v. 202, p. 195–211, doi:10.1144/GSL.SP.2002.202.01.10.

617 Kirschvink, J.L., 1980, The least- squares line and plane and the analysis of palaeomagnetic
618 data: Geophysical Journal of the Royal Astronomical Society, v. 62, p. 699–718,
619 doi:10.1111/j.1365-246X.1980.tb02601.x.
620 Latutrie, B., and Ross, P.S., 2020, Phreatomagmatic vs magmatic eruptive styles in maar-
621 diatremes: a case study at Twin Peaks, Hopi Buttes volcanic field, Navajo Nation, Arizona:
622 Bulletin of Volcanology, v. 82, doi:10.1007/s00445-020-1365-y.
623 Lawrence, R.B., Armstrong, R.L., and Berman, R.G., 1984, Garibaldi Group Volcanic Rocks of
624 the Salal Creek Area, Southwestern British Columbia: Alkaline Lavas on the Fringe of the
625 Predominantly Calc-Alkaline Garibaldi (Cascade) Volcanic Arc: Journal of Volcanology
626 and Geothermal Research, v. 21, p. 255–276.
627 Lescinsky, D.T., and Fink, J.H., 2000, Lava and ice interaction at stratovolcanoes: Use of
628 characteristic features to determine past glacial extents and future volcanic hazards: Journal
629 of Geophysical Research: Solid Earth, v. 105, p. 23711–23726, doi:10.1029/2000jb900214.
630 Lisé-Pronovost, A., St-onge, G., Gogorza, C., Haberzettl, T., Preda, M., Kliem, P., Francus, P.,
631 Zolitschka, B., Pasado, T., and Team, S., 2013, High-resolution paleomagnetic secular
632 variations and relative paleointensity since the Late Pleistocene in southern South America:
633 Quaternary Science Review, v. 71, p. 91–108, doi:10.1016/j.quascirev.2012.05.012.
634 Lisiecki, L.E., and Raymo, M.E., 2005, A Pliocene-Pleistocene stack of 57 globally distributed
635 benthic D 18 O records: Paleoceanography, v. 20, p. 1–17, doi:10.1029/2004PA001071.
636 Martin, U., and Németh, K., 2007, Blocky versus fluidal peperite textures developed in volcanic
637 conduits, vents and crater lakes of phreatomagmatic volcanoes in Mio/Pliocene volcanic
638 fields of Western Hungary: Journal of Volcanology and Geothermal Research, v. 159, p.
639 164–178, doi:10.1016/j.jvolgeores.2006.06.010.
640 Mathews, W.H., 1952, Mount Garibaldi, A Supraglacial Pleistocene Volcano in Southwestern
641 British Columbia: American Journal of Science, v. 250, p. 81–103.
642 Moorhouse, B.L., and White, J.D.L., 2016, Interpreting ambiguous bedforms to distinguish
643 subaerial base surge from subaqueous density current deposits: The Depositional Record, v.
644 2, p. 173–195, doi:10.1002/dep2.20.
645 Mullen, E.K., and Weis, D., 2013, Sr-Nd-Hf-Pb isotope and trace element evidence for the origin
646 of alkalic basalts in the Garibaldi Belt, northern Cascade arc: Geochemistry, Geophysics,
647 Geosystems, v. 14, p. 3126–3155, doi:10.1002/ggge.20191.

Read, P.B., 1979, Meager Creek Geothermal Area: , p. 1 Sheet, doi:10.4095/129507.

Read, P., 1990, Mt Meager Complex, Garibaldi Belt, Southwestern BC.: Geoscience Canada, v. 17, p. 167–170.

Roddick, J.C., and Souther, J.G., 1987, Geochronology of Neogene volcanic rocks in the northern Garibaldi Belt, British Columbia: Geological Survey of Canada, v. 87–2, p. 21–24.

Russell, J.K., Edwards, B.R., and Porritt, L.A., 2013, Pyroclastic passage zones in glaciovolcanic sequences: Nature Communications, v. 4, doi:10.1038/ncomms2829.

Schiffman, P., Watters, R.J., Thompson, N., and Walton, A.W., 2006, Hyaloclastites and the slope stability of Hawaiian volcanoes: Insights from the Hawaiian Scientific Drilling Project's 3-km drill core: Journal of Volcanology and Geothermal Research, v. 151, p. 217–228, doi:10.1016/j.jvolgeores.2005.07.030.

Skilling, I.P., 2009, Subglacial to emergent basaltic volcanism at Hlöðufell, south-west Iceland: A history of ice-confinement: Journal of Volcanology and Geothermal Research, v. 185, p. 276–289, doi:10.1016/j.jvolgeores.2009.05.023.

Skilling, I.P., White, J.D.L., and Mcphie, J., 2002, Peperite : a review of magma-sediment mingling: Journal of Volcanology and Geothermal Research, v. 114, p. 1–17.

Smellie, J.L., 2007, Glacial landforms | Quaternary vulcanism, subglacial landforms: Encyclopedia of Quaternary Science, p. 784–798, doi:10.1016/B0-44-452747-8/00101-0.

Smellie, J.L., 2006, The relative importance of supraglacial versus subglacial meltwater escape in basaltic subglacial tuya eruptions: An important unresolved conundrum: Earth-Science Reviews, v. 74, p. 241–268, doi:10.1016/j.earscirev.2005.09.004.

Stewart, M.L., Russell, J.K., and Hickson, C.J., 2008, Geology, Pebble Creek formation, British Columbia: , p. 1 sheet.

Stroncik, N.A., and Schmincke, H.U., 2002, Palagonite - A review: International Journal of Earth Sciences, v. 91, p. 680–697, doi:10.1007/s00531-001-0238-7.

Sun, S.S., and McDonough, W.F., 1989, Chemical and isotopic systematics of oceanic basalts: Implications for mantle composition and processes: Geological Society Special Publication, v. 42, p. 313–345, doi:10.1144/GSL.SP.1989.042.01.19.

Turner, G.M., 1987, A 5000 year geomagnetic palaeosecular variation record from western Canada: Geophysical Journal of the Royal Astronomical Society, p. 103–121.

Tweed, F.S., and Russell, A.J., 1999, Controls on the formation and sudden drainage of glacier-

impounded lakes: Implications for jökulhlaup characteristics: Progress in Physical Geography, v. 23, p. 79–110, doi:10.1191/030913399666727306.

White, J.D.L., 1996, Pre-emergent construction of a lacustrine basaltic volcano, Pahvant Butte, Utah (USA): Bulletin of Volcanology, v. 58, p. 249–262, doi:10.1007/s004450050138.

White, J.D.L., 2000, Subaqueous eruption-fed density currents and their deposits: Precambrian Research, v. 101, p. 87–109, doi:10.1016/S0301-9268(99)00096-0.

White, J.D.L., and Houghton, B.F., 2006, Primary volcaniclastic rocks: Geology, v. 34, p. 677–680, doi:10.1130/G22346.1.

White, J.D.L., Mcphie, J., and Skilling, I., 2000, Peperite: A useful genetic term: Bulletin of Volcanology, v. 62, p. 65–66, doi:10.1007/s004450050293.

White, J.D.L., and Valentine, G.A., 2016, Magmatic versus phreatomagmatic fragmentation: Absence of evidence is not evidence of absence: Geosphere, v. 12, p. 1478–1488, doi:10.1130/GES01337.1.

Wilson, A.M., and Russell, J.K., 2020, Glacial pumping of a magma-charged lithosphere : A model for glaciovolcanic causality in magmatic arcs: Earth and Planetary Science Letters, v. 548, p. 116500, doi:10.1016/j.epsl.2020.116500.

Wilson, A.M., and Russell, J.K., 2017, Lillooet Glacier basalts, southwestern British Columbia, Canada: Products of Quaternary Glaciovolcanism: Canadian Journal of Earth Sciences, v. 54, p. 639–653, doi:10.1139/cjes-2016-0201.

Wilson, A.M., and Russell, J.K., 2018, Quaternary glaciovolcanism in the Canadian Cascade volcanic arc—Paleoenvironmental implications: Field Volcanology: A Tribute to the Distinguished Career of Don Swanson. Geological Society of America, v. 538, doi:10.1130/2018.2538(06).

Wilson, A.M., Russell, J.K., and Quane, S.L., 2019, The table, a flat-topped volcano in southern British Columbia: Revisited: American Journal of Science, v. 319, p. 44–73, doi:10.2475/01.2019.02.

Wilson, A.M., Russell, J.K., and Ward, B.C., 2020, Paleo-glacier reconstruction in southwestern British Columbia , Canada : A glaciovolcanic model: Quaternary Science Reviews, v. 218, p. 178–188, doi:10.1016/j.quascirev.2019.06.024.

Woodsworth, G., 1977, Geology of Pemberton (92J) Map Area: Geological Survey of Canada, p. 1 sheet.

Zimanowski, B., Fröhlich, G., and Lorenz, V., 1991, Quantitative experiments on phreatomagmatic explosions: Journal of Volcanology and Geothermal Research, v. 48, p. 341–358, doi:10.1016/0377-0273(91)90050-A.

Figure Captions

Figure 1: Location and geologic setting of Cracked Mountain volcano. A) Map of the Cascade volcanic arc in the USA and Canada (i.e. Garibaldi volcanic belt (GVB)) (modified from Mullen and Weis, 2013; Wilson and Russell, 2017). B) Undivided geological map of MMVC distribution of Mt. Meager volcanic deposits (MV), basement (Bu) throughout the region (Woodsworth, 1977; Read, 1979; Harris and Russell, 2021). The youngest MMVC eruption, 2350 B.P. Pebble Creek Formation (PcF) (Hickson et al., 1999; Stewart et al., 2008) is differentiated from other MMVC volcanics. Cracked Mountain (CM) is situated south of the main MMVC (Wilson and Russell, 2018; Harris and Russell, 2021). Map projection based on Universal Transverse Mercator, Zone 10U North American Datum 1983.

Figure 2: Geology of Cracked Mountain. A) Geologic map showing the distribution of CM volcanic lithofacies. Dyke location and orientations are shown in red; extensional cracks are shown in black. The volcanic edifice unconformably overlies basement granodiorites (Bg) and mica-schists (Bs). White-numbered dots show locations of representative stratigraphic logs (B, C). B) Graphic logs showing volcanic stratigraphy at various locations and elevations within the map area (depicted in Figs. 2A). Lithologies are depicted with various patterns and symbols while corresponding map units are shown in the same colours as Fig. 2A. Red lines shown in map units represent intruding dykes observed within the lithologies of the graphic logs. Map projection based on Universal Transverse Mercator, Zone 10U North American Datum 1983.

Figure 3: Physiographic setting of Cracked Mountain volcano. A) NE-SW oriented Google Earth imagery of Cracked Mountain showing the location of volcanic deposits overlying basement rocks (white-arrows). B) N-S oriented Google Earth imagery of Cracked Mountain (outlined in white), highlighting visible cracks parallel the steep drainages. C) South-West facing DEM hillshade map showing CM volcanics (red shaded outline) situated above present-day Meager Creek and Elaho Valleys.

Figure 4: Field photos displaying bedform structures of CM lapilli tuffs: A) Field photo showing ~2 m thick exposure of massive, moderately sorted ash and lapilli tuff underlying poorly sorted tuff breccia (Tb). Half metre hammer (white arrow) for scale. B) Field photo displaying a ~0.5m thick exposure of thinly bedded, well-sorted, ash, and a lapilli tuff (Lt_2) interbedded within massive lapilli tuff (Lt_1). One metre hammer for scale. C) Field photo showing ~10 m wide and ~4 m thick exposure of moderately to poorly sorted, locally spatter dominated, lapilli tuff (Lt_3). One metre hammer for scale. The white box shows the location of the inset displaying fluidal clast surrounded by a vitric ash matrix.

Figure 5: Field photos illustrating the association of pillowed lava (Lpi), peperitic dykes (Ld_1), and enclosing lapilli tuff (Lt_1): A) Photomosaic of ~30 m wide by~ 4 m thick exposure of pillowed lava (Lpi) mingled with massive lapilli tuff (Lt_1). Inset (white box) shows pillowed

lobes with a lens of Lt_1. One metre hammer (white arrow) for scale. B) Annotated version of 5A. Note preserved lenses of Lt_1 within extensive Lpi deposits. C) Field photo showing ~5 m wide and ~4 m deep exposure of "blooming" pillowed lava (Lpi) within massive lapilli tuff (Lt_1). Note a feeder dyke (Ld_1) (white arrow) is visible through the coherent Lpi body. Inset (white box) shows pillowed lava in contact with a lens of Lt_1. D) Annotated version of 5C.

Figure 6: Field photos illustrating the association of pillowed lava (Lpi) with peperites (Pi) and peperitic textures present at Cracked Mountain: A) Photomosaic of ~10 m wide and ~4 m thick exposure volcaniclastic peperite (Pi) formed along the margins of coherent bodies of pillowed lava (Lpi). Tape measure (white arrow) and human for scale. Inset (white box) shows quench-fragmented peperite bounding Lpi. Marker for scale. B) Annotated version of 6A. C) Example of globular (fluidal) peperite (Pi) texture. Pen for scale. D) Example of blocky peperite (Pi) texture. Pen for scale.

Figure 7: Field photos illustrating the structure and variable clast types found in Cracked Mountain tuff breccias (Tb). A) Massive, ~1.5 m thick, tuff breccia (Tb) dominated by subrounded to blocky lava, overlying massive lapilli tuff (Lt_1). Hammer (1 m) for scale. B) Massive, tuff breccia (Tb) dominated by subrounded to blocky lava, with minor, block-sized lapilli tuff lithics (Lt_1) (white arrows). C) Rare lithic of pahoehoe (Ls) entrained within tuff breccia (Tb). Hammer (1 m) for scale.

Figure 8: Field photos illustrating pillow and subaerial lavas from Cracked Mountain. A) Stacked sequence of pillow lavas (Lp) (view looking NW at SE base of CM), ~150 m wide and ~40 m thick. White arrows mark approximate edifice basement contact at 1500 m a.s.l. B) Wall of pillow lava (Lp), ~10 m high, exposed on the S margin of the volcano. C) Coherent bulbous pillow lobes (Lp) up to ~0.5 m in diameter. One metre hammer (white arrow) for scale. D) Remnant flow-top of jointed sheet lava (Ls) near the summit of the volcano (~1,600 m a.s.l). Black arrows show granitic erratics and scour marks covering the surface of the lava. Hammer (1 m) for scale.

Figure 9: Photomicrographs showing textures of CM volcaniclastic lithofacies. A-C, E, G, and H are plane-polarized images at 4x magnification with a 2 mm scale. D and F are from Scanning Electron microscopy (SEM), shown with a 300 μm scale bar. A) Photomicrograph of interstitial pillow lava sediment (Lp) composed of coarse, jig-saw fractured, weakly vesiculated glass. B) Photomicrograph of massive, ash, and lapilli tuff (Lt_1) showing fine-grain juvenile clasts including microlitic (Mlt), blocky (Bl), and highly vesiculated (Vsc) vitric clasts. The matrix contains a small proportion of intact to fragmented olivine (Ol) and plagioclase crystals. C) Photomicrograph of massive lapilli tuff (Lt_1) showing size range of juvenile vitric clasts and shapes (i.e. blocky and cuspate). D) SEM photomicrograph of 9C showing both blocky and highly cuspate vesiculated shapes of fine ash fraction (~ 100 μm). E) Photomicrograph of massive lapilli tuff (Lt_1) showing coarse to fine juvenile clasts and fragmental crystals olivine and plagioclase. Highly vesiculated vitric clasts are abundant. F) SEM photomicrograph of 9E showing a highly vesiculated (50-60%) coarse vitric juvenile clast. G) Photomicrograph of thinly bedded lapilli tuff (Lt_2) showing layers of ultra-fine ash separating layers of coarser, blocky (Bl), and vesiculated (Vsc) vitric clasts. H) Photomicrograph of matrix material supporting spatter

dominated lapilli tuff (Lt_3) showing a highly vesiculated, vitric juvenile lapilli clast within an ash and fine lapilli-sized vitric matrix.

Figure 10: Major (XRF) and trace elemental (ICP-MS) compositions for whole-rock samples (white) and glasses (black) from Cracked Mountain. A) Total alkali ($Na_2O + K_2O$) vs Silica (SiO_2) wt. % (TAS) with the classification of Le Bas et. al. (1986) and Irvine and Baragar (1971). B) Mg# (molar MgO/ (MgO +FeO*)∗100) vs Silica (SiO_2) wt. % for Cracked Mountain volcanics. CM samples not measured with ferric titration use the mean value of Fe 2+/ Σ Fe =0.7228 (N=7) for CM basalts that were determined. C) Rare Earth Trace Element (REE) compositions of Cracked Mountain volcanics, normalized to a Chondrite after Sun and McDonough (1989).

Figure 11. Stereographic plots of paleomagnetic remanence directions for Cracked Mountain volcano and examples of typical, well-behaved demagnetization data. A) Stereographic plot of mean data from CM Sites 2-9 and their α_{95} (p = 0.05) confidence circles (see Table C1). The mean of sites 2-9 is shown in red. Geocentric Axial Dipole (GAD) field inclination for sampling latitude is shown with a filled square (see Table C1). Present Earth's Field direction (PEF) is shown with a filled star (see table C1). Site 1 is excluded as it is an outlier (see details in Appendix C) that appears to represent rotation associated with extensional collapse. B) Stereographic plots (left) show magnetization directions after stepwise AF and thermal demagnetization of the Lt_1 sample from Site 2 (CMV015A/B), where the filled circles lie on the lower hemisphere. Precision values, given as the maximum angle of deviation (MAD) are included. Orthogonal plots (right) show horizontal projections as filled circles and vertical projections as open circles. Natural remanent magnetization is shown with a circle and cross. Units are in amperes per metre. Note that AF demagnetization for sample CMV015A produces more coherent results than does thermal demagnetization. C) Well-behaved stepwise demagnetization data for a dyke (Ld_1) sample collected at Site 6 (CMV029A/B), layout, symbols, and units as 12B. Note, this sample shows identical results for AF and thermal demagnetizations. Based on the results of detailed AF and thermal demagnetization of pilot specimens from each site, AF demagnetization is the preferred treatment.

Figure 12: Schematic model (2x V.E) of volcanic evolution of CM. Stage 1: Explosive phreatomagmatic eruptions, building a subaqueous tephra cone. Stage 2: The sustained intrusion of lava into unconsolidated sediments, and endogenous growth of the edifice. Dykes that breached the margins of the volcanic pile produced pillowed lavas within the englacial lake. Stage 3: Involves the buildup of CM to the level of the englacial lake (or above) and subaerial eruption of lava as well as syn-eruptive debris flows forming deposits of massive tuff breccia. Schematic drainage channels are shown forming through the ice sheet. Stage 4: Post-eruptive, glacial retreat, where the top of the edifice is scoured off. Additionally, the removal of glacially confined margins causes extensional, gravity-driven stress on of the overs steeped volcanic successions, causing cracks to form and partial edifice collapse.

Figure 13: Paleoclimate glacial reconstruction at the time of Cracked Mountain eruption, ~401 ka. A) Hillshade DEM for CM map area overlain showing the dispersal of glacial ice. We use the approximate summit of CM (~1650 m a.s.l) as the minimum height at which glacial ice is reached. All regions below 1650 m are shown in light blue (i.e. ice) and all regions above 1650

m are shown in brown. CM edifice is shown in green within a schematic englacial lake. B) Undivided N-S (A-A') and E-W (B'-B) cross-sections for CM, shown at no VE. Volcanic rocks (green) overlie basement (pink) above steep valleys to the N (Meager Creek) and W (Elaho Valley). Schematic glacier ice is shown confining CM with an englacial lake forming around the volcano. The minimum thickness of the englacial lake is ~250 m estimated from the total thickness of the edifice. C) Schematic 3D DEM is shown for the CM map area. The same colours and symbols were used in 13A. Glacial ice is shown reaching minimum elevations of 1650 m a.s.l. with a minimum thickness of ~850 m based on the elevation of Meager Creek. Schematic drainage channels are shown based on the physiographic setting of the edifice.

Figure 14: Mid to late Pleistocene Marine $\delta^{18}O$ ($^{o}/_{oo}$) isotope record (MIS), modified from Lisiecki and Raymo (2005) showing fluctuations (and numbered stages) in global ice from, where higher $\delta^{18}O$ represents periods of more global ice and lower $\delta^{18}O$ represents periods of lower global ice. The vertical axis is a record of time (ka) with magnetic pole orientations shown through the Pleistocene. Dark bars are times of normal polarity and white bars are times of pole reversal. The dashed box indicates the blow-up portion of the MIS from 250-600 ka. The Cracked Mountain plateau age of 401.6 ± 38.1 ka is plotted (grey shaded) on the blow-up MIS portion, representing times from the waning of MIS 12 through MIS 11. The preferred age of Cracked Mountain is indicated with a dashed line at ~425 ka.